MULTI-SCALE FEATURES OF ATMOSPHERIC RIVERS AND THE LINKAGES WITH LOCAL-SCALE HYDROLOGICAL IMPACTS ON THE U.S. WEST COAST

BY

HUANCUI HU

DISSERTATION

Submitted in partial fulfillment of the requirements
for the degree of Doctor of Philosophy in Atmospheric Sciences
in the Graduate College of the
University of Illinois at Urbana-Champaign, 2018

Urbana, Illinois

Doctoral Committee:

Professor Francina Dominguez, Chair
Professor Praveen Kumar
Professor Steve Nesbitt
Professor Zhuo Wang

ABSTRACT

Atmospheric rivers (ARs), defined as filamentary structures of strong water vapor transport in the atmosphere, are an important component of the hydrologic cycle and are characterized by a multi-scale nature. On the one hand, ARs are embedded in the planetary-scale Rossby waves and account for the majority of poleward moisture transport in the midlatitudes. On the other hand, ARs are the fundamental reason for generating extreme basin-scale precipitation and floodings over many regions of the world including the U.S. West Coast in the winter season. The goal of this dissertation is to examine the multi-scale features associated with ARs. The links to local-scale hydrological impacts are of particular interest because they are the key in estimating local hydrological consequences associated with climate variability and projecting flood-risk changes with global warming.

The first part of this dissertation presents the connection between the characteristics of large-scale Rossby wave breaking (RWB) over the eastern North Pacific and the regional-scale hydrological impacts associated with landfalling ARs on the U.S. West Coast. ARs associated with RWB account for 2/3 of the landfalling AR events and >70% of total AR-precipitation in the winter season. The two regimes of RWB – anticyclonic wave breaking (AWB) and cyclonic wave breaking (CWB) – are associated with different directions of the vertically integrated water vapor transport (IVT). AWB-ARs impinge in a more westerly direction on the coast while CWB-ARs impinge in a more southwesterly direction. Most of the landfalling ARs along the northwestern coast of the U.S. (states of Washington and Oregon) are AWB-ARs, due to their westerly impinging angles arriving more orthogonally to the western Cascades and more efficiently transforming water vapor into precipitation through orographic lift. Consequently, AWB-ARs

account for the most extreme streamflows in the region. Along the southwest coast of the U.S. (California), the southwesterly impinging angles of CWB-ARs are more orthogonal to the local topography, and are also characterized by more intense IVT. Consequently, CWB-ARs are associated with the most intense precipitation and account most of the extreme streamflows in southwest coastal basins.

The second part of this dissertation investigates the contribution of tropical moisture on AR strengths and the associated meso-scale mechanisms. We used the water vapor tracer tool embedded in WRF (WRF-WVT) to "tag" moisture from the tropics in the simulations of the top 15% of ARs affecting the Northwest (based on their IVT). This tool helps to provide a joint view of tracer moisture (that from the tropics) and total moisture in ARs' lifecycles. We first analyze an AR event in detail and find that tropical moisture affects AR development through direct and indirect mechanisms in the following ways: 1) narrow line-convection over the cold front is mostly from tropical moisture; 2) latent heat release associated with cold-frontal precipitation induces positive potential vorticity that helps enhance the pre-cold-frontal low-level jet (LLJ); 3) the enhanced LLJ in turn enhances entrainment of tropical moisture along this AR. We also found significant "mutual amplification" near the warm front where most landfall is generated. It is achieved through strong warm air advection ahead of the tropical moisture arrival that helps enhance low-level moisture convergence and vertical ascent (in other words, an enhanced ageostropic circulation). These processes associated with tropical moisture are confirmed by other simulated cases. We found increasing trends of cold-frontal precipitation and latent heat generated potential vorticity in line with enhanced LLJ. However, ARs with stronger tropical moisture contribution are not characterized by significantly stronger ageostrophic circulation. This indicates the importance of other dynamical factors in modulating AR precipitation.

The third part of this dissertation examines the interactions of local land surface conditions with ARs. We develop and implement a novel numerical water tracer model within the Noah-Multiparameterizations (WT-Noah-MP) land surface model to investigate the regional responses to ARs arriving in the U.S. Pacific Northwest. This approach is specifically designed to track individual hydrometeorological events (such as ARs) and it provides a more comprehensive representation of the physical processes beyond the standard land surface model output. In the WT-Noah-MP simulations, we "tag" the precipitation from individual AR events using this tool, and it provides stores, fluxes and transit time estimates of the "tagged" water in the surface-subsurface system. Consequently, we are able to test the tracer mixing assumptions by comparing transit times obtained from isotope observations in the WS10 watershed (Oregon). In addition, from a regional simulation of an extreme AR, the model helps to differentiate the flood response due to direct precipitation from indirect thermal effects and showed that a large portion of this event water was retained in the soil after 6 months. The water tracer addition in Noah-MP can help us quantify the long-term memory in the hydrologic system that can impact seasonal hydroclimate variability through evapotranspiration and groundwater recharge.

ACKNOWLEDGEMENTS

First, I would like to express my deep gratitude to my advisor Prof. Francina Dominguez. She is an incredible teacher and advisor with passion, patience, and sharp eyes in seeing chances to make breakthrough, poking holes in researches and leading me with strong hands throughout my Ph.D. I am always amazed by her clear comprehension of both details and large pictures, which stimulated me a lot and will continuously stimulate me in the future. For the previous six years being her student, I have received tremendous encouragement, inspiration and trust from her. I really appreciate being with her in these very important six years in my life.

I would also like to thank the rest of my thesis committee: Prof. Praveen Kumar, Prof. Steve Nesbitt and Prof. Zhuo Wang. I learned a lot from the joint group meetings co-hosted by Dr. Praveen Kumar and Dr. Francina Dominguez. Being exposed to subjects different from my research area, it helped me to broaden my scope to the existing various topics in the science community and also to identify the commonalities of the problems that we are facing. Thanks to Dr. Steve Nesbitt, who taught the "Tropical Meteorology" course that I especially enjoyed (also being my last course). I was able to piece together the meteorology and climate components I learned from graduate school and to view the Earth system in a more integrated way. I am also very grateful to Dr. Zhuo Wang, who always encouraged me with kind words for my small achievements. I also admire her enormous knowledge and deep insights over a variety of subjects.

I also appreciate the help and suggestions I received from my other coauthors to improve my manuscripts: Dr. Gan Zhang, Dr. Marty Ralph, Dr. David Lavers, Dr. Jeffery McDonnell and Dr. Gochis.

My sincere thanks also go to Dr. Erick Rivera, Dr. Alejandro Martinez, Dr. Zhao Yang, and future doctors Itinderjot Singh, Divyangsh Chug, Sujan Pal and Carolina Bieri, who provided me with tremendous support in my different stages along the path pursuing my Ph.D. and the sense of belonging as a research group. Being a unique group doing hydrometeorology and hydrology researches in the atmospheric sciences department, they make me feel special but not isolated.

I thank my fellow lab-mates for the stimulating interesting discussions, expanding my English vocabulary (e.g. “mammatus” and “virga”) and for all the funs we have had in the last few years. I will remember all the joy from the parties, coffee breaks, bowling and everything.

Last but not the least, I would like to thank my family: my parents and my sister for supporting me unconditionally and always feeling proud of me. Special thanks to my niece Weini Xing, who is a sweet and talented little girl that always made me laugh whenever I thought of her.

To my beloved family.

TABLE OF CONTENTS

CHAPTER 1: INTRODUCTION

1.1 Motivation

Perhaps some of the most striking features in a satellite loop of the Earth are the long filaments in the atmosphere that transport water across great distances (Newman et al. 2012). These narrow corridors characterized by strong vapor transport predominantly occur in the mid-latitudes and are known as Atmospheric Rivers (ARs; see an example in Fig. 1-1). About 4 or 5 ARs occur in each hemisphere at any given time, and > 90% of poleward vapor transport in the mid-latitudes are accomplished by these ARs (Zhu and Newell 1998; Gimeno 2014). While critical in the global water and energy cycle, ARs are also the main driver for cool-season precipitation and flooding events for many coastal regions (e.g. Ralph et al. 2006a; Neiman et al. 2011; Lavers and Villarini 2013). In particular, coastal basins along the U.S. West Coast are heavily affected by ARs due to the fact that: 1) ARs bring in vast amounts of moisture from the Pacific and 2) the Cascade-Sierra mountain ranges are natural barriers that force the moisture to rise and produce heavy precipitation.

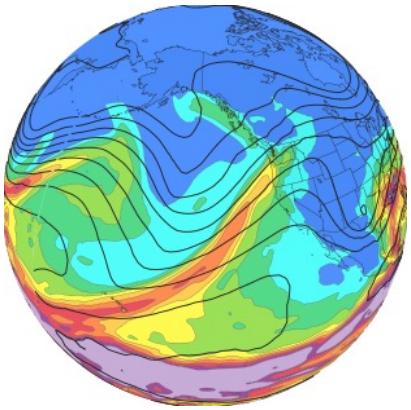

Figure 1-1. An example of AR (color shading shows column-integrated vapor), in association with Rossby waves (wave patterns indicated by the black 500mb geopotential heights)

As a result, precipitation associate with ARs accounts for >55% of cool-season precipitation along the U.S. West Coast (Rutz et al. 2014) and make important contributions to how much snow and water will be available in these regions. While providing critical sources for western (especially California) water supplies (Dettinger et al. 2011; Ralph and Dettinger 2011), landfalling ARs can also be devastating as they can result in major floods for coastal river basins

from California to Washington (Ralph et al. 2006a; Neiman et al. 2011). For example, an extreme AR occurred in December 2007 significantly affected the Chehalis River basin (western Washington) causing 11 fatalities, a 4-day closure of the I-5 highway, and USD 1 billion economic losses (Dominguez et al. 2018). Given the critical role of ARs for the water resources, as well as they risk they pose for flooding in many coastal regions, it is important that the hydrometeorology community improves our understanding of AR features and their variability in order to better predict them on time scales from days to decades (Ralph and Dettinger 2011). It is of particular importance to advance our understanding and predicting regional- to local-scale impacts, which are of the greatest societal relevance but are often most uncertain. Therefore, to better link AR characteristics with regional- and local-scale hydrological impacts is the subject of this dissertation.

To achieve this goal, it is important to understand how ARs interconnect global circulation with local-scale extreme events through multi-scale interactions. As mentioned earlier, ARs are a key phenomenon of the global transport of water vapor (Newman et al. 2012). Physically, they represent the vapor transport components within mid-latitude transient eddies that are embedded in planetary-scale Rossby waves (Zhu and Newell 1998; Fig. 1-1). Within synoptic eddies, ARs are located in the warm sector of extratropical cyclones and are closely tied to the pre-cold-frontal low-level jet (Neiman et al. 2008b). If discussed in the context of the Norwegian classical cyclone model, ARs represent a configuration similar to the warm conveyor belt, a poleward, slantwise ascending airstream rising above the warm front near the cyclone center (Carlson 1980; Browning 1999; Sodemann and Stohl 2013). This rapidly ascending airflow towards the leading edge of ARs tend to generate intense precipitation and condensational latent heating. However, in contrast to maritime extratropical cyclones, the precipitation induced by landfalling ARs affecting the U.S.

West Coast are also largely modified by orographic effects, and mesoscale details of the AR (e.g. atmospheric stability, frontal waves) and how ARs interact with the local mountainous terrain determines how much precipitation affects different watersheds (Neiman et al. 2008b; 2011; Ralph et al. 2011; Houze 2012). Subsequently, whether a landfalling AR generates local flooding is ultimately influenced by the land surface conditions (snow and soil conditions) that can greatly modulate runoff generation processes (Neiman et al. 2008b; Leung and Qian 2009). Now, from all these processes with such a broad spatial spectrum, what are the key processes that affect AR features and how can we link these aspects with ARs' hydrological impacts at regional- and local-scales?

Rossby Wave Behavior: At the planetary-scale, AR features are subject to the changes in Rossby wave dynamics. As the narrow and elongated structures existing between troughs and ridges, ARs' lifecycle is closely related with the growth and decay of these eddies (Barnes and Hartmann 2012). Recently, Rossby wave breaking (RWB) has been found of particular relevance in modulating moisture transport features along the U.S. West Coast. This is especially true in the context of interannual variability because the two regimes of RWB are modulated by ENSO phases and hence are closely tied to the U.S. West Coast winter precipitation in association with ARs (Ryoo et al. 2013). Similarly, extratropical circulation changes in a future climate are very likely to modulate AR characteristics through the interaction with RWB (Payne and Magnusdottir 2014). How can large-scale dynamical changes of ARs influence the risk of extreme flooding for coastal river basins? What are the key elements that link large-scale dynamics with AR local impacts? Can this knowledge be used to better forecast AR variability and change?

Tropical/Subtropical Moisture Export: Within the scale of extratropical cyclones, the two concepts "atmospheric river" and "warm conveyor belt", while representing similar subjects,

correspond to two different mechanisms. "Atmospheric river" suggests a more two-dimensional riverlike flow from the (sub)tropics to the mid- and high latitudes while "warm conveyor belt" describes a more three-dimensional ascending structure of airstreams that also account for local moisture confluence (Sodemann and Stohl 2013). One aspect that has raised particular interest is the tropical-extratropical linkages, as some ARs can extend to the eastern tropics Pacific and seem to "tap" Hawaiian moisture into U.S. West Coast (referred as "pineapple express"). In some cases, this tropical-extratropical interaction has been linked to extreme precipitation (Knippertz and Wernli 2010; Ralph et al. 2011; Neiman et al. 2014). However, the relative role of direct advection of tropical moisture vs. local moisture convergence within ARs is under debate (Bao et al. 2006; Knippertz and Wernli 2010; Sodemann and Stohl 2013; Dacre et al. 2015; Eiras-Barca et al. 2017). Furthermore, the mechanisms by which tropical moisture can modulate AR features and their inland impacts is largely unknown. A better understanding of the impacts of tropical moisture could potentially help us better anticipate how ARs could change thermodynamically through increase water vapor content that a warmer climate will bring (Trenberth 1998; Sodemann and Stohl 2013; Dominguez et al. 2018).

Land Surface Processes: Upon the arrival of ARs on the U.S. West Coast, intense precipitation usually occurs and the precipitation distribution is modulated to a first order by orographic forcing (Colle 2004; Neiman et al. 2011). Another onshore characteristic often observed in association with ARs' arrival is anomalously warm air temperature. This can raise melting-levels and results in rain falling at high elevations over a much larger catchment area and can also induce snowmelt below the melting-levels. These processes can greatly enhance runoff volume and amplify streamflow responses (White et al. 2002; Lundquist et al. 2008; Neiman et al. 2008b). In addition, soil moisture conditions, can considerably modulate the transit features of AR

precipitation over land in producing fast streamflow response or longer lifetimes in the subsurface (Leung and Qian 2009; Dettinger 2013; Hrachowitz et al. 2016). To better understand the variability of AR-induced flooding risks and how it can affect local hydroclimate, it is important for us to better quantify and understand the influence of land surface conditions on ARs' hydrometeorological impacts and the interactions between them.

1.2 Objective and Scientific Questions

The overarching goal of this dissertation is to investigate different aspects of AR features at a wide range of spatial scales, with a focus on establishing the linkages of these aspects with local hydrological impacts on the U.S. West Coast. AR features are closely linked with atmospheric variability and its consequences over land, and the linkages built can be used to better understand and anticipate how water resources and the exposure of flood risk associated with ARs can be modulated by climate variability and change. Ranging from planetary-scale to local-scale, we will address three key science questions:

Q1. What is the effect of upper-tropospheric dynamics, in the form of Rossby wave breaking, on basin-scale precipitation and streamflow?

Q2. How can tropical moisture export modulate AR development and precipitation features?

Q3. How can land surface conditions modify the transit features of ARs over land and what are the effects of AR precipitation on local hydroclimate?

1.3 Scientific Contribution

As the atmospheric component of the NASA funded interdisciplinary project "Atmospheric Rivers and changing flood risk in the Pacific Coast region of the Western U.S.", I have examined

three different aspects of ARs, varying with scales, that can individually affect ARs' hydrological impacts over the U.S. West Coast: i) I linked planetary-scale Rossby wave breaking (RWB) with AR features and found a dramatic latitudinal variation of AR-related landfall and streamflow responses to the two dominant modes of RWB (Hu et al. 2017); ii) I investigated synoptic- to meso-scale processes and analyzed how tropical moisture can contribute to extreme ARs in direct and indirect ways. In particular, I found critical roles of tropical moisture in enhancing cold-frontal low-level jets and promoting local convergence where landfall occurs (Hu and Dominguez 2018); iii) I focused on how land surface conditions can modulate AR flooding, and found an important contribution from antecedent snowpack melt to streamflow and a long-term memory left by extreme ARs on the local hydroclimate (Hu et al. 2018) (depicted in Fig. 1-2).

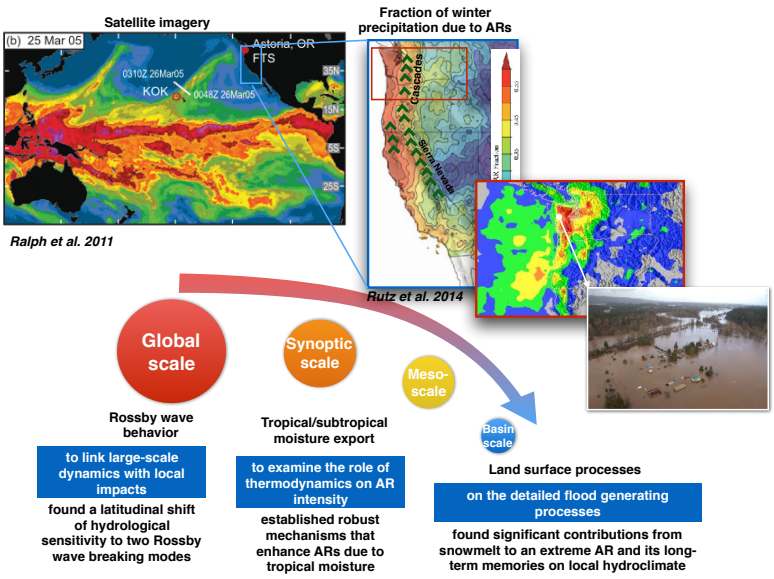

Figure 1-2. Schematic summarizing the multi-scale aspects of ARs and their roles for ARs' hydrological impacts examined by this dissertation.

In addition to advancing our scientific understanding of ARs, I also developed a novel water tracer tool in the model framework of Noah-MP. I used this tool to "tag" precipitation from individual AR events to track the subsequent terrestrial lifecycle. This is a tool that can be easily adapted for other hydrometeorological phenomenon to help us understand physical processes over land and identify model deficiency if used in combination with isotopic tracer observations.

CHAPTER 2: LINKING ATMOSPHERIC RIVER HYDROLOGICAL IMPACTS ON THE U.S. WEST COAST TO ROSSBY WAVE BREAKING

(Published in Journal of Climate, May 2017)

Atmospheric rivers (ARs) have significant hydrometeorological impacts on the U.S. West Coast. This study presents the connection between the characteristics of large-scale Rossby wave breaking (RWB) over the eastern North Pacific and the regional-scale hydrological impacts associated with landfalling ARs on the U.S. West Coast (36°N~49°N). ARs associated with RWB account for 2/3 of the landfalling AR events and >70% of total AR-precipitation in the winter season. The two regimes of RWB – anticyclonic wave breaking (AWB) and cyclonic wave breaking (CWB) – are associated with different directions of the vertically integrated water vapor transport (IVT). AWB-ARs impinge in a more westerly direction on the coast while CWB-ARs impinge in a more southwesterly direction.

Most of the landfalling ARs along the northwestern coast of the U.S. (states of Washington and Oregon) are AWB-ARs. Due to their westerly impinging angles when compared to CWB-ARs, AWB-ARs arrive more orthogonally to the western Cascades and more efficiently transform water vapor into precipitation through orographic lift than CWB-ARs. Consequently, AWB-ARs are associated with the most extreme streamflows in the region.

Along the southwest coast of the U.S. (California), the southwesterly impinging angles of CWB-ARs are more orthogonal to the local topography. Furthermore, the southwest coast CWB-ARs have more intense IVT. Consequently, CWB-ARs are associated with the most intense precipitation. As a result, most of the extreme streamflows in southwest coastal basins are associated with CWB-ARs. In summary, depending on the associated RWB type, ARs impinge

on the local topography at a different angle and have a different spatial signature of precipitation and streamflow.

2.1 Introduction

Precipitation related to atmospheric rivers (Zhu and Newell 1998; Ralph et al. 2004) are critically important for water resources on the West Coast of the United States. Between 25%~50% of the annual precipitation falling on the West Coast is related to AR events (Dettinger et al. 2011), and ARs are responsible for a large fraction of the snow water equivalent accumulated in the Sierra Nevada mountains (Guan et al. 2010). ARs are, by definition, filamentary structures characterized by very strong atmospheric water vapor transport (usually measured as vertically integrated vapor transport - IVT), moving as much water as is discharged by the Amazon river (Zhu and Newell 1994; 1998). Consequently, when they impinge on the orographic barriers of the U.S. West Coast, ARs can cause extreme precipitation and floods (Ralph et al. 2004; 2006a; Neiman et al. 2008a; Ralph and Dettinger 2011; Dettinger et al. 2011; Neiman et al. 2011). In western Washington, for example, most flooding events observed in four watersheds were associated with ARs (Neiman et al. 2011). While the maximum AR frequency occurs on the northern coast of Oregon and Washington and gradually decreases southward (Rutz et al. 2014), ARs are still associated with some of the largest floods along watersheds in the California coast, such as the Russian river basin (Ralph et al. 2006b). And 3-day precipitation totals associated with long-duration landfalling ARs in California are as large as anywhere in the country, including precipitation due to landfalling tropical storms and hurricanes (Ralph and Dettinger 2012). At the basin-scale, the precipitation totals and resulting hydrologic response of the basins depend on the angle of impingement of the ARs in relation to the local topography (Ralph et al. 2003). Analyzing the basin hydrologic

response in western Washington, Neiman et al. (2011) found that the basins draining the western slopes of mountains are impacted by westerly ARs, while basins draining the southern flanks had their largest discharges during southwesterly AR flows.

AR events involve a multi-scale chain of events: from planetary-, synoptic-, meso- to the watershed and river reach scale. As an example, an extreme AR event analyzed by Ralph et al. (2011) involved several key ingredients from the planetary scale (tropical convection, storm tracks) to the mesoscale (frontal wave). However, while extratropical cyclones (and ARs associated with these cyclones) usually develop with baroclinic instability as a lower- and upper-tropospheric coupled system, the connection between ARs and upper-troposphere atmospheric dynamics and variability has only recently become an active area of research. Of particular relevance is the effect of large-scale Rossby wave breaking (RWB) on meridional moisture transport and ARs. Liu and Barnes (2015) found that about 61% of the total extreme meridional moisture transport across 60°N was due to RWB events likely associated with ARs. Ryoo et al. (2013) linked the U.S. West Coast winter precipitation with upper-tropospheric potential vorticity (PV) during El Niño and La Niña years, through the interannual variability between the two regimes of RWB.

RWB represents irreversible mixing of the synoptic eddies in the midlatitude Rossby waves and has two primary regimes - anticyclonic wave breaking (AWB) and cyclonic wave breaking (CWB) (Thorncroft et al. 1993). AWBs are often observed on the equatorward flank of the jet where conditions are dominated by anticyclonic wind shear, while CWBs generally occur on the poleward flank of the jet where cyclonic wind shear is predominant. During the mature stage of the two lifecycles, both RWB types exhibit strong non-linear characteristics. Analysis of eddy meridional momentum and vertical heat fluxes of the AWB suggests poleward momentum

transport and “absorption” of eddy energy in the upper-tropospheric subtropics, which convert eddy kinetic energy (EKE) into stronger upper-tropospheric westerlies. In contrast, EKE accompanying the CWB is absorbed less because most of the upward propagating Rossby waves are reflected back downward from the high-latitude upper troposphere. As a result, the CWB has a relative persistent EKE. The feedback between eddies and the mean flow also results in a poleward shift of the jet after AWB but an equatorward shift of the jet after CWB. Associated with significantly different dynamic features, AWB (CWB) phenomenon is manifested by irreversible mixing of PV in an anticyclonic (cyclonic) manner (McIntyre and Palmer 1985; Thorncroft et al. 1993).

In addition to eddy momentum and heat fluxes, moisture flux characteristics accompanying RWB are often discussed in the context of ARs. Close relationships have been found between the strongest landfalling ARs on the West Coast and clear AWB signals in the eastern Pacific (Payne and Magnusdottir 2014; Mundhenk et al. 2016b). A trajectory study by Ryoo et al. (2015) relates the different patterns of trajectories among ARs with RWB and demonstrates that about 66% of the AR events they evaluated are associated with AWB. While these studies demonstrate the importance of AWB, it is important to note that AR precipitation has the most significant impacts on the southwestern coast when CWB occurs more frequently over the eastern Pacific during El Nino years (Ryoo et al. 2013). In addition, the trajectory study by Ryoo et al. (2015) ties ARs with intense precipitation over the southwestern U.S. with a stronger relevance to CWB.

ARs are modulated by extratropical circulation patterns which are, in turn, related to RWB patterns. In fact, the latitude of maximum AR occurrence is related to that of maximum AWB occurrence (Mundhenk et al. 2016a). For this reason, changes in RWB can be used as indicators for AR variability and change (Payne and Magnusdottir 2014; Mundhenk et al. 2016b). As an

example, the El Niño southern oscillation (ENSO) can modify storm track strength and location (e.g. storm track strength and location; Seager et al. 2003; Orlanski 2005; L'Heureux and Thompson 2006) and produce significantly different precipitation patterns over the West Coast, likely through ARs with different RWB types (Cayan and Roads 1984; Ryoo et al. 2013). In terms of long-term climatic trends, global warming can potentially induce changes in RWB dynamics and consequently lead to changes in ARs. A poleward displacement of midlatitude jets with climate change is found to result in a robust and significant reduction of CWB frequency and a poleward shift of AWB distribution (Barnes and Hartmann 2012). The poleward shift of midlatitude jets also leads to a significant decrease of AR events in aquaplanet simulations (Hagos et al. 2015). At the same time, the thermodynamic change associated with climate change further complicates the problem (Gao et al. 2015). Such changes could potentially have a significant impact on regional precipitation in the West Coast (Salathé 2006; Dettinger 2011; Mass et al. 2011; Ryoo et al. 2013). This is particularly important because of the socioeconomic and ecologic consequences of changes in flood risk and water resources associated with these extreme events on both the local and regional scales. However, establishing the relationship between upper-tropospheric dynamics and regional hydrologic impacts is a critical first step before evaluating possible changes in regional hydrologic impacts due to climate change along the West Coast.

In this study, we focus on establishing the link between RWB and the regional-scale hydrological impacts of ARs on the U.S. West Coast, as a necessary step to bridge large-scale atmospheric dynamics and regional scale hydrological variability. This understanding provides the dynamic basis for studies on changes in AR-related hydrologic impacts due to climate variability and change. To do this, we examine the AR characteristics along the U.S. West Coast in association with RWB. We make particular efforts on establishing the relationship between AR features and

precipitation along the northwest and southwest coast of the US, and quantifying the AR impact on two river basins within the northwest and southwest coast, respectively. Both of the basins have experienced severe AR-related floods in the past. In addition, we analyze the streamflow features of three additional river basins located between them. The key questions we want to address are: 1) How important is RWB for the impacts of landfalling ARs on the U.S. West Coast? 2) Is there a significant precipitation difference associated with AWB- and CWB-ARs and how does it change with latitude? 3) How do coastal watersheds along a latitudinal gradient respond hydrologically to AWB- and CWB-ARs at a regional scale?

2.2 Data and Methods

We examine the ARs that affect the west coast of the U.S. with their eastern leading edges reaching 36°N~49°N (black hatched area in Fig. 2-1a). Note that ARs at latitudes lower than 36°N were excluded in this analysis because of the small number of AR events and weak RWB signals (Fig. 2-2). To determine the importance of RWB for the impacts of landfalling ARs (question 1), we quantify the number of AR events and the precipitation associated with RWB. To explore the latitudinal variation of AR characteristics and impacts (question 2 and 3), we examine two subsets of ARs reaching two 5-degee bands: 44°N~49°N and 36°N~41°N (red hatched grids in Fig. 2-1a). These two bands correspond to the northwest and southwest coast of the U.S.

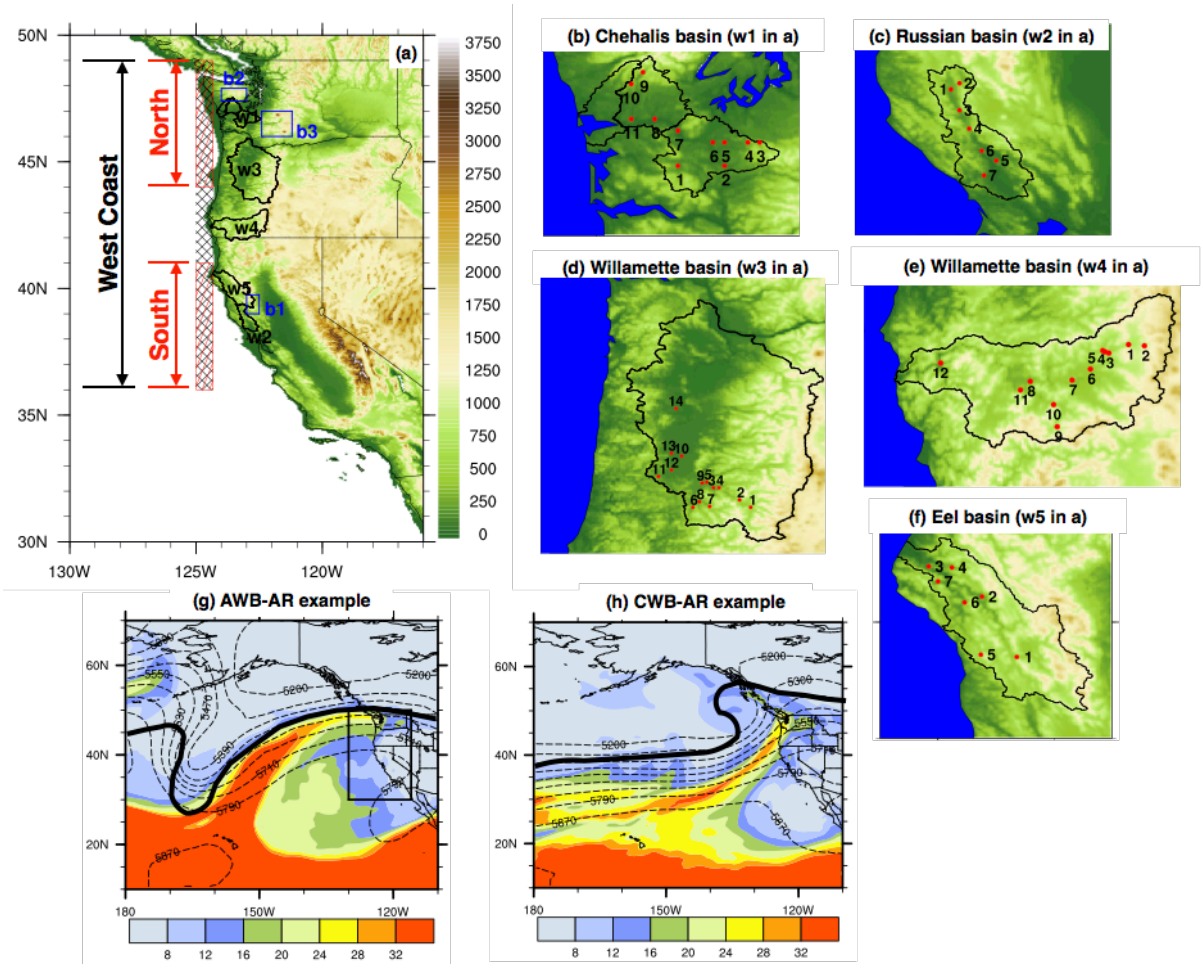

Figure 2-1. (a) Topography features of the U.S. West Coast (unit: m). ARs with the leading edges reaching the black-hatched area are grouped as ARs affecting the West Coast; ARs withe leading edges within the north (south) red-hatched area are grouped to represent the ARs affecting the northwest (southwest) coast. The five river basins are delineated by black lines, named as w1~w5. Blue boxes suggest the area used to represent local precipitation features, named as b1~b3. (b)~(f) Magnified view of the five basins w1~w5 with USGS streamflow gauges. (g) An AR example associated with AWB event on Nov 22, 1990, with precipitable water (color shaded, unit: kg m^{-2}) and 500mb geopotential height (dashed contours, unit: m). (h) The same as (g) but showing an AR event with CWB on Jan 14, 1988. The thick black lines in (g) and (h) indicate the 1.5PVU contour at 350K surface (1PVU=$10^{-6}m^{-2}Kkg^{-1}$).

We link the latitudinal variation of RWB-AR features, together with mountain range orientations, to local precipitation of two river basins. For the ARs impacting the northern band, we focus on the Chehalis river basin in western Washington (Fig. 2-1b) where several AR-induce major floods have caused extensive damages and economic losses. For instance, from December 1 through December 3, 2007, the Chehalis basin experienced heavy rainfall and severe flooding

which caused a 4-day closure of the I-5 highway (Hayes 2008). The Chehalis river basin is surrounded by mountains, except for the Pacific Ocean on its western boundary. Storms centered over the mountains on the southern Willapa Hills and Cascade foothills on the east can cause flooding in the upper Chehalis. Storms over the Olympic Mountains to the north can cause flooding in the lower Chehalis, without having much effect in the upper basin (Ruckelshaus Center 2012). For the ARs affecting the southern band, we focus on the Russian river basin in northern California (Fig. 2-1c). The effect of ARs on extreme flooding in the Russian basin has been studied by Ralph et al. (2006a; 2013). All seven extreme streamflow events between 1997 and 2006 were found to be associated with ARs (Ralph et al. 2006a). Surrounded by coastal mountains, the Russian river flows southward along the valley for about 145 km and drains into the Pacific Ocean (Anders et al. 2011). The mean orientation of the crest of the coastal mountains is along ~140°-320° (Ralph et al. 2013).

In addition to the Chehalis and Russian river basins, we analyzed three additional coastal river basins along a latitudinal gradient between the Russian and Chehalis. The three additional river basins, from north to south, are the Willamette (northwestern Oregon), Rogue (southwestern Oregon) and Eel (northern California) river basins. They are generally bounded by the Cascade-Sierra Nevada Mountains to the east and Pacific to the west, with rivers flowing into the Pacific Ocean. Using these five basins, we can assess the large-scale hydrologic impacts at different latitudes, while retaining the catchment-specific implications.

2.2.1 MERRA data

We use 30 years (1979-2009) of the National Aeronautics and Space Administration (NASA) Modern-Era Retrospective Analysis for Research and Application (MERRA) reanalysis dataset for meteorological analysis. It has high resolution, both in time and space. MERRA is

characterized by a significant improvement of the atmospheric branch of the hydrological cycle (Rienecker et al. 2011) compared with the previous generation of reanalyses (e.g. ERA-40, NCEP/NCAR-R1). Two-dimensional time-averaged fields (e.g. vertically integrated flux of specific humidity) are available at 1/2° × 2/3°, hourly resolution, while 3-dimensional instantaneous fields (e.g. zonal wind) at pressure levels are available at 1.25° × 1.25°, 3-hourly resolution.

2.2.2 AR identification

The AR identification method developed by Lavers et al. (2012; 2013) is applied to MERRA data. In contrast to other detection methods that use satellite-estimated water vapor content to identify AR events (Ralph et al. 2004; Neiman et al. 2008b; Ralph and Dettinger 2012; Wick et al. 2013), Lavers et al. (2012) evaluate the AR dimensions using IVT values above a certain threshold according to the latitude range of the AR's leading edge. IVT is calculated using Equation 2-1.

$$IVT = \sqrt{QU^2 + QV^2} \qquad \text{Equation 2-1}$$

where QU and QV are the vertically integrated eastward and northward vapor flux respectively from MERRA.

We perform the AR detection algorithm three times by confining AR leading edges within three latitude bands. Two 5-degree latitude bands (44°N~49°N and 36°N~41°N) are selected to investigate differences in ARs with latitude, and one broad band (36°N~49°N) is selected as the entire West Coast. As an example, the first step in the identification process for the AR events in the northern band (44°N~49°N) is to determine the IVT threshold. The maximum IVT values for coastal grids (between 44°N~49°N along 124.7°W, northern red hatched area in Fig. 2-1a) at 1200UTC of each day from October to March during 1979-2009 are taken to construct the distribution. Then, the IVT threshold is determined as the 85th percentile the IVT distribution. For

each time step (hourly) during the 1979-2009 Oct-Mar period, the algorithm searches grids with IVT values above the threshold, starting from the coastal grids towards the west-southwest-south directions. A time step is flagged as an AR step if consecutive grids spanning more than 2000 km exceed the threshold. However, an AR event has to last more than 18h (≥18 continuous AR step). We adjust the original length criteria used in Lavers et al. (2012; 2013) from 20 degrees of longitude to a solid length threshold of 2000 km to accommodate for our wider latitudinal range. In addition, individual events must be separated by at least 24 hours. The IVT thresholds and the number of AR events for the three bands are shown in Table 2-1. We note that a lower threshold (350 kg $m^{-1}s^{-1}$) is used when identifying AR events for the West Coast.

Table 2-1. Information about three latitude bands used to identify AR events and the number of AR events identified

	Name	Latitudinal range	IVT threshold (kg $m^{-1}s^{-1}$)	Number of events		
				ARs	AWB-ARs	CWB-ARs
1	North 5-degree band	44°N~49°N	384	192	80	61
2	South5-degree band	36°N~41°N	350	156	55	55
3	West Coast	36°N~49°N	350	301	122	91

2.2.3 RWB type classification

RWB is manifested by the large-scale, rapid irreversible overturning of PV contours on isentropic surfaces (McIntyre and Palmer 1985). An objective algorithm to detect RWB types developed by Strong and Magnusdottir (2008) is applied. This detection method objectively identifies the poleward-advection low-PV tongues associated with anticyclonically and cyclonically overturning PV contours at the 350K isentropic surface (see Fig. 2-1 in Strong and Magnusdottir 2008).

In this study, PV is interpolated to the 350K isentropic surface at every time step in which an AR event was detected. We then use the detection method of Strong and Magnusdottir (2008a) to

objectively classify RWB events as AWB and CWB. The detection method provides information about the location of each RWB. This information is used to link the RWB with the ARs. For the RWB to be linked to an AR, the location of RWB needs to be in the vicinity the concurring AR (within the box of 180°~110°W and 30°N~70°N). In the case when more than one RWB occur simultaneously (e.g. Messori and Caballero 2015), the AR is attributed to the RWB type whose breaking location is closer to the AR. AR events can hence be classified into AWB-ARs, CWB-ARs and non-breaking ARs. Figures 2-1g and h show examples of AWB- and CWB-ARs with 1.5 PVU contours (1 PVU = 10^{-6} m^{-2} K kg^{-1}).

RWB activity undergoes seasonal variation, and concentrating the RWB detection on a specific isentropic level could potentially limit the validity of the RWB detection. However, by examining the RWB signals on two more levels (340K and 330K isentropic levels), we find consistent patterns of AR-related RWB detection with slightly different horizontal extension (not shown). Since the RWB type is more important than its horizontal extent in this study, we take the results from the 350K as representative of RWB.

2.2.4 Livneh gridded land surface data

To investigate precipitation spatial distribution within the watershed, we use 1/16° degree latitude/longitude data from Livneh et al. (2013) for the winters from 1979 to 2009. The daily precipitation and temperature are derived from daily precipitation observations from approximately 20,000 NOAA Cooperative Observer stations across the conterminous U.S. We use this observational product to evaluate the spatial distribution of AR-related precipitation in sections 2.4 and 2.5.

2.2.5 Streamflow gauge measurements

The AR-related streamflow characteristics of the five river basins are obtained from long-term streamflow measurements by the U.S. Geological Survey (USGS). To be consistent, only gauges with 30-year data availability (1979 Oct - 2009 Mar) are included in our analysis. The number of streamflow gauges within each river basin is listed in Table 2-2 and their locations are indicated in Figures 2-1b~f.

Table 2-2. Number of USGS streamflow gauges in the five coastal basins having record from 1979 to 2009.

	Basin name	# of USGS streamflow gauges
1	Chehalis river basin	11
2	Russian river basin	7
3	Willamette river basin	14
4	Rogue river basin	12
5	Eel river basin	7

2.3 Importance of RWB-ARs to the West Coast

Using data and methods described in sections 2.2.1~2.2.3, we identify AR events affecting the West Coast and classify those with clear RWB signatures into AWB or CWB types. A total number of 301 AR events are identified, and are binned based on the impinging latitude at the time of maximum IVT (Fig. 2-2a) and the average impinging latitude throughout AR duration (Fig. 2-2b), respectively. Consistent with previous studies (Neiman et al. 2008a; Rutz et al. 2014), the northwest coast experiences more ARs, especially to the north of 42°N. The number of ARs peaks at 43°N~45°N (Fig. 2-2), in agreement with the peak AR probabilities found by Guan and Waliser (2016). Note that in Fig. 2-2, we include AR events that impinge south of 36°N. However, they are a small subset of events and usually accompanied by weak RWB signals, thus are excluded in the rest of the analyses.

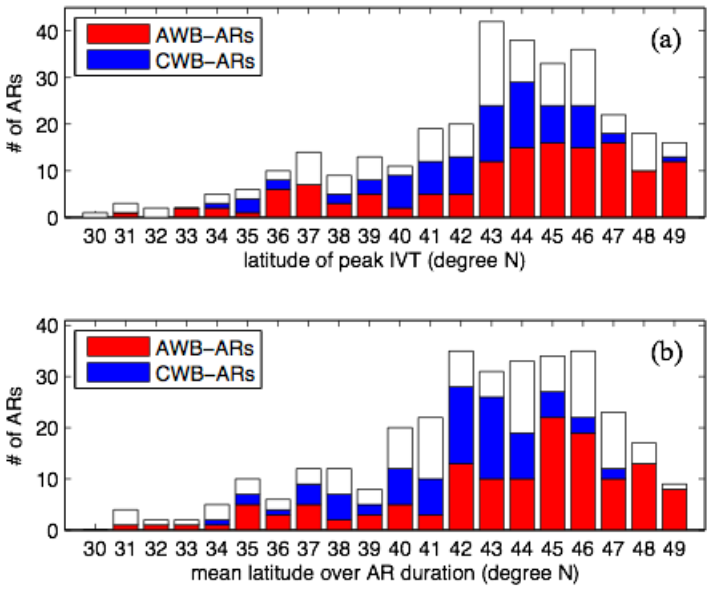

Figure 2-2. Histograms of AR event numbers binned with (a) the impinging latitude at the time step with the maximum IVT and (b) the averaged impinging latitude with peak IVT over all steps within each AR's duration.

Among 301 AR events, about 2/3 (204 events) are associated with RWB. AWB-ARs (129 events) clearly outnumber CWB-ARs (75 events) from Table 2-1, consistent with the higher frequency of AWB in general as a result of the preferential equatorward propagation of Rossby waves and anticyclonic wind shear on the equatorward flank of the jets (Hoskins et al. 1977; Thorncroft et al. 1993; Nakamura and Plumb 1994; Peters and Waugh 1996; Barnes and Hartmann 2012). However, Ryoo et al. (2015) estimated that ~66% of ARs are associated with AWB. The discrepancy likely arises due to the difference in the AR detection method – IVT is used in this study but precipitable water was the criteria for Ryoo et al. (2015).

Figure 2-2 also suggests that peak IVT of CWB-ARs tends to occur at 40°N~46°N while peak IVT of AWB-ARs impinges mostly at 42°N~49°N. As a result, more frequent AWB-ARs are also found affecting the northern 5-degree band but similar AWB-ARs and CWB-AR frequencies are found in the southern 5-degree band (Table 2-1). However, within the confining latitude bands, some AR events of long duration and wide-range effect are counted twice (once in each latitude band). The summation of two subsets is thus larger than for the West Coast (Table 2-1). In fact, 28 CWB-ARs are counted in both latitudinal subsets while only 14 AWB-ARs are included in both subsets, indicating a broader north-to-south movement of CWB-ARs. AWB-ARs, on the other

hand, appear to impinge at higher latitudes and have limited latitudinal movement within their lifespan.

In addition to the number of ARs related with RWB, we also examine their significance to winter precipitation. We quantify the precipitation associated to each AR using the two-day maximum precipitation (the same approach used in Warner et al. 2012), occurring ± 2 days around the peak IVT time step. The ratio of RWB-ARs precipitation to the total AR precipitation is calculated and shown in Fig. 2-3. More than 70% of total AR precipitation results from RWB-ARs in Washington and the fraction gradually decreases to ~60% towards the southwest coast (Fig. 2-3a). However, mountainous regions in California have higher ratios. When partitioning the total ratios in Fig. 2-3a into AWB-ARs and CWB-ARs parts, they clearly demonstrate opposite spatial patterns (Figs. 2-3b and c). The northwest coast (Washington and Oregon) is predominantly affected by AWB-ARs, accounting for over 40% of AR precipitation, even more on the Cascades (>45%). In contrast, a larger portion of AR precipitation in the southwest coast (California) is associated with CWB-ARs despite their peak IVT latitudes at 40°N~46°N. The

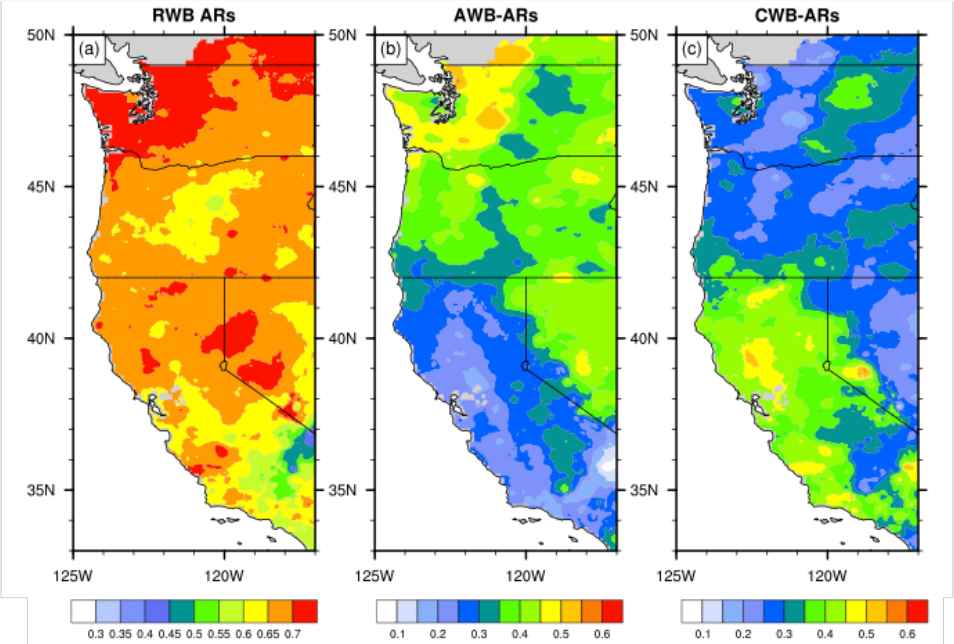

Figure 2-3. Ratio of AR-related precipitation due to (a) RWB-ARs, (b) AWB-ARs and (c) CWB-ARs.

reasons for the large difference in the region of impact between the two AR types are further explored by two subsets of ARs affecting the two latitude bands and river basins.

2.4 Difference of AWB and CWB AR Features

To demonstrate the AR features associated with AWB and CWB, we analyze two subsets of ARs reaching the two 5-degree latitude bands. Instead of mixing all ARs impacting the West Coast together, we use two AR subsets because, by refining the ARs impinging the northwest (44°N~49°N) and southwest coast (36°N~41°N), we can 1) obtain clear AR features, and 2) reveal the latitudinal variation of AR features with two RWB types.

2.4.1 Synoptic composites

AR synoptic composites are constructed for the north band (Figs. 2-4a~c) using MERRA data. Compared with composites averaged from all AR events (Fig. 2-4a), AWB-ARs appear to impinge in a more westerly direction (Fig. 2-4b). In contrast, CWB-ARs impinge in a southwesterly direction towards the coast (Fig. 2-4c). Note that we focus on the impinging angles of ARs towards the West Coast, but not the overall orientation of the filamentary structure. In fact, CWB-ARs have more zonal orientation off the coast, while AWB-ARs have a more meridional orientation, similar to the features found by Sodemann and Stohl (2013).

AWB-ARs are characterized by a pronounced 875mb high to the southeast of the ARs while CWB-ARs show an enhanced 875mb low to the northwest of the ARs (Figs. 2-4b and c). The near-surface low found in CWB-ARs is consistent with the single and large surface cyclones mostly coexisting with CWB-ARs (Moore et al. 2012; Sodemann and Stohl 2013). CWB-ARs are also associated with a longer filamentary structure with higher IVT ($\geq$560 kg $m^{-1}s^{-1}$) (Fig. 2-4c). This could be partially attributed to the stronger wind speed of CWB-ARs (as seen the stronger pressure gradient for the 875mb level in Fig. 2-4c). Similar synoptic features are found in the composites

for the south-band subset (Figs. 2-4d~f) but with the patterns shifted southward. However, the strength of AWB-ARs along the southern coast is weakened significantly. Further details of the IVT transport and dynamical features will be investigated in section 2.4.2, to explain the difference between AWB- and CWB-ARs and the latitudinal variation.

A similar pattern as northern AWB-AR composites (Figs. 2-4b) with a strong high pressure to the southeast of the ARs is found by Neiman et al. (2008a) for ARs with water vapor plumes impacting the northwest coast. In contrast, CWB-AR composites (Figs. 2-5c and f) with an anomalous low to the northwest of the ARs resemble those for ARs affecting the southwest coast (see Fig. 6 in Neiman et al. 2008a). This suggests a significant and consistent role of AWB-ARs to the northwest coast, but a more prominent role of CWB-ARs for the southwest coast.

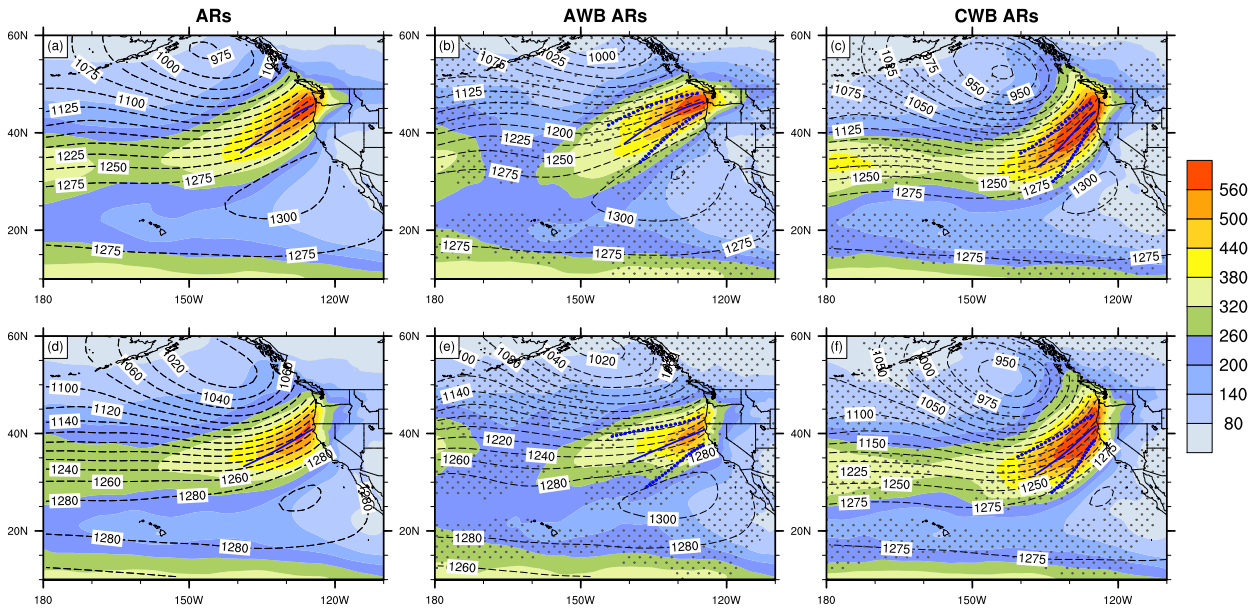

Figure 2-4. Composites of IVT (color shaded, unit: kg m-1s-1) and 875mb geopotential height (dashed contours, unit: m) for the northern subset of ARs (a~c) and the southern subset of ARs (d~f). Blue solid lines suggest the averaged IVT axes starting from the coast and extending 2000 km into the Pacific. The blue dots in (b), (c), (e) and (f) suggest the standard deviation of IVT axes.

2.4.2 Vertical structures

Decomposing the IVT into moisture and wind components at each level, Fig. 2-5 shows the averaged vertical profiles near the coast for each AR type. They are extracted from the grid along 124.7°W having the maximum IVT. Therefore, for the northern ARs, all the profiles (Fig. 2-5a~c) are from the grids in the North 5-degree band (the north red hatched area in Fig. 2-1a); and for the southern ARs, profiles (Fig. 2-5d~f) are extracted from the grids in the South 5-degree band (the south hatched area in Fig. 2-1a). Figure 2-5 clearly reveals that the horizontal wind speed is the dominant factor in driving the difference of IVT. For the northern ARs, CWB-ARs on average have stronger winds below 750mb level, which result in significant stronger moisture transport below 800mb level despite slightly less humidity. However, the AWB-ARs have much stronger upper-tropospheric winds. A similar horizontal wind difference between AWB- and CWB-ARs is found in the southern ARs, but with greater moisture fluxes of CWB-ARs extending to 550mb. The horizontal wind, especially the lower-tropospheric winds, generally decreases with latitude (Figs. 2-5a and d).

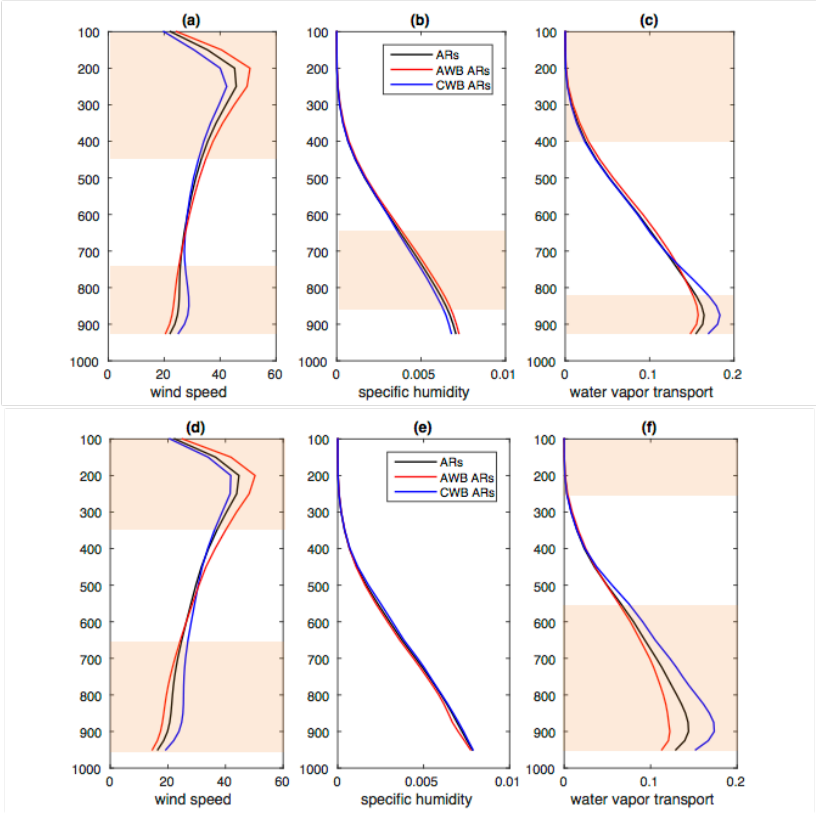

Figure 2-5. Vertical profiles composites for the northern subset of ARs (a~c) and for the southern subset of ARs (d~f). Orange shaded levels are the levels with significant different means between AWB- and CWB-ARs with 99% confidence level.

In addition to coastal profiles, we present the composite vertical cross-sections along the core IVT axes (Fig. 2-6). Specific humidity, vertical and horizontal wind speed are shown along the 2000 km axes for each RWB type. Consistent with Fig. 2-5, CWB-ARs have stronger horizontal winds in the lower-troposphere, extending to ~1500 km off the coast (Figs. 2-6c and g). It is consistent with the enhanced pressure gradient of CWB-ARs suggested by Fig. 2-4. Humidity, on the other hand, shows smaller differences close to the coast and larger differences away from the coast (Figs. 2-6d and h). The reason is that 2000 km away from the coast, along the CWB-AR axes, the AR is usually located at lower latitudes than AWB-ARs (Figs. 2-4c and f).

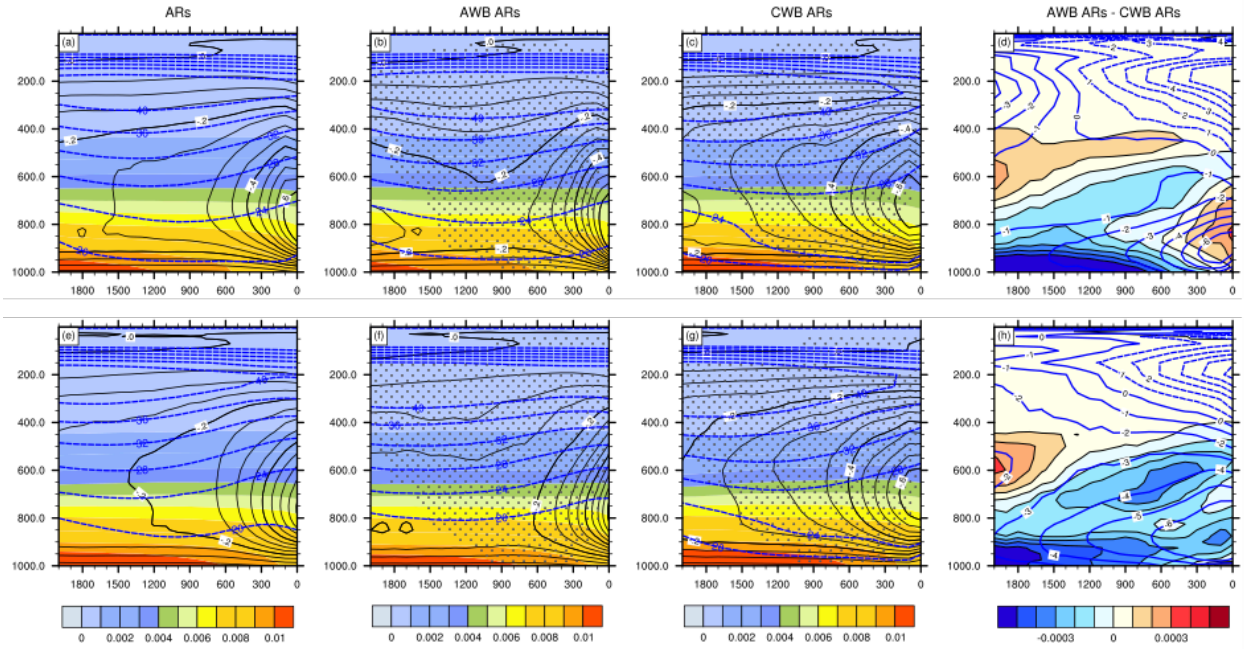

Figure 2-6. Vertical cross-sections composites along the AR maximum IVT axes for the northern subset of ARs (a~c) and the southern subset of ARs (e~g). Specific humidity (unit: kg/kg) is shaded by colors; omega (unit: Pa/s) is contoured by black lines with intervals of 0.05 Pa/s; wind speed (unit: m/s) is contoured by blue dashed lines with intervals of 4 m/s. Stippled area in (b), (c), (f) and (g) show regions with significant different omega means between AWB- and CWB-ARs with 90% confidence level. (d) and (h) show the difference of specific humidity (color shaded) and wind speed (blue contours) between AWB-ARs and CWB-ARs for the northern and southern ARs. Horizontal tick label indicates the distance (unit: km) away from the coast into the Pacific. Each column shares the same colorbar.

The vertical wind component, critical in producing precipitation, is plotted in Figure 2-6. Significant stronger uplifting by CWB-ARs is found from the coast to ~1500 km offshore between

900mb~200mb. Taking a plan view of the vertical winds at the 750mb where the maximum occurs, AWB-ARs show strong uplifting confined closely to the coast (blue shading Fig. 2-7b), indicating a stronger relation with orographic lifting near the coast. CWB-ARs, on the other hand, show greater and extended regions of uplift offshore (blue shading Figs. 2-7c and f). It has been shown that vertical heat fluxes are much stronger in the mature phase of CWB, as most upward EKE is reflected in CWBs rather than absorbed, as in the AWB case (Thorncroft et al. 1993). This helps

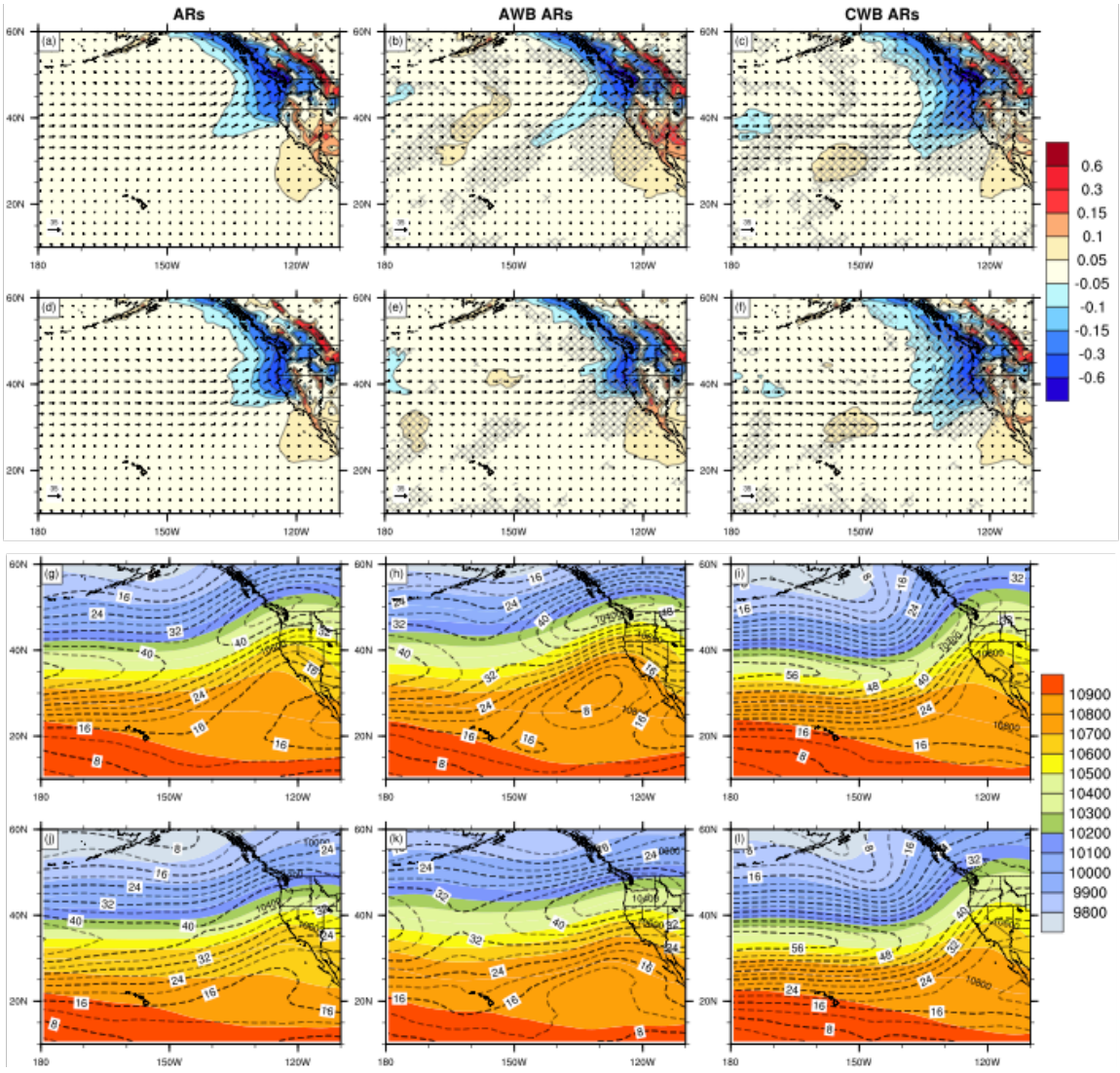

Figure 2-7. Omega (color shaded, unit: Pa/s) and horizontal wind (vectors, unit: m/s) composites at 750mb level for the northern subset of ARs (a~c) and the southern subset of ARs (d~f). Geopotential height (color shaded, unit: m) and horizontal wind speed (dashed contours, unit: m/s) composites at 250mb level for the northern subset of ARs (g~i) and the southern subset of ARs (j~l). Hatched areas in (b), (c), (e) and (f) show regions with significant different omega means between AWB- and CWB-ARs with 90% confidence level.

support the stronger vertical wind component shown in CWB-ARs. Moreover, the extended region of ascent could also be attributed to the stronger wind-terrain interaction of CWB-ARs, due to the stronger lower-tropospheric winds, which tend to extend the upstream ascent significantly (Wang and Chang 2012). It is also important to note that AWB-ARs have additional local maxima of uplifting over the mountains further inland – over the Cascades in Fig. 2-7b and over the Rockies in Fig. 2-7e.

In the upper troposphere, AWB-ARs have a more poleward displacement of the jet than CWB-ARs (Figs. 2-7g~l). AWB-ARs occur on the equatorward flank of the jet where anticyclonic wind shear is present; AWB also helps maintain the poleward position of the jet through poleward momentum fluxes. On the other hand, CWB-ARs occur on the poleward flank of the jet and the jet location is maintained relatively equatorward. However, the southern AWB-ARs are much weaker than the northern AWB-ARs (as can be seen in Figs. 2-7h and k), because they are associated with weaker westerly winds and probably are subject to stronger EKE absorption by the upper subtropics as moving closer to the subtropics.

2.4.3 Impinging angles and precipitation distribution

Given the orographic uplifting suggested in section 2.4.2, we connect the AR impingement towards the coast with precipitation inland. We calculate the impinging angle of ARs to the coast, based on the direction of vapor flux at the

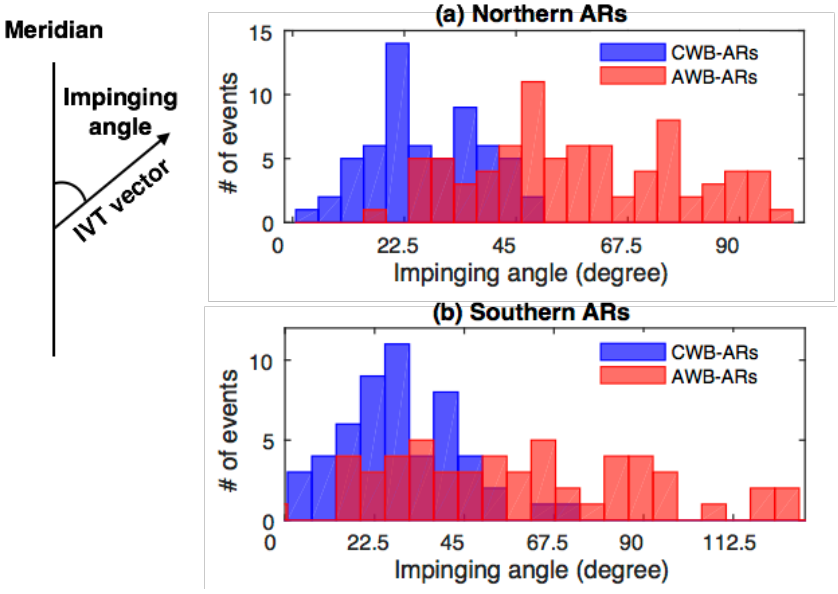

Figure 2-8. Histograms of AR impinging angles for (a) northern subset of ARs and (b) southern subset of ARs. The schematic on the left suggests the definition of impinging angles.

grid with maximum IVT along 124.7°W (red hatched area in Fig. 2-1a). We define the impinging angle as the angle between the IVT vector and the meridian (see the schematic in Fig. 2-8). The difference in impinging angles (averaged over the lifespan of the ARs) between AWB- and CWB-ARs, is represented by the histograms of impinging angles in Fig. 2-8. The averaged variation of impinging angles within the AR's lifespan is ±10.0° for the northern subset of ARs and ±11.5° for the southern subset of ARs relative to the averages over the lifespan.

For the north band, the angles of CWB-ARs mostly range between 10° and 46°, while AWB-ARs have a broader range and have a median angle of 55.1°. Due to the crucial interaction between AR and topography (Ralph et al. 2003; Neiman et al. 2011), the impinging angle differences associated with these two types of ARs result in a very distinct area of topographic uplifting and

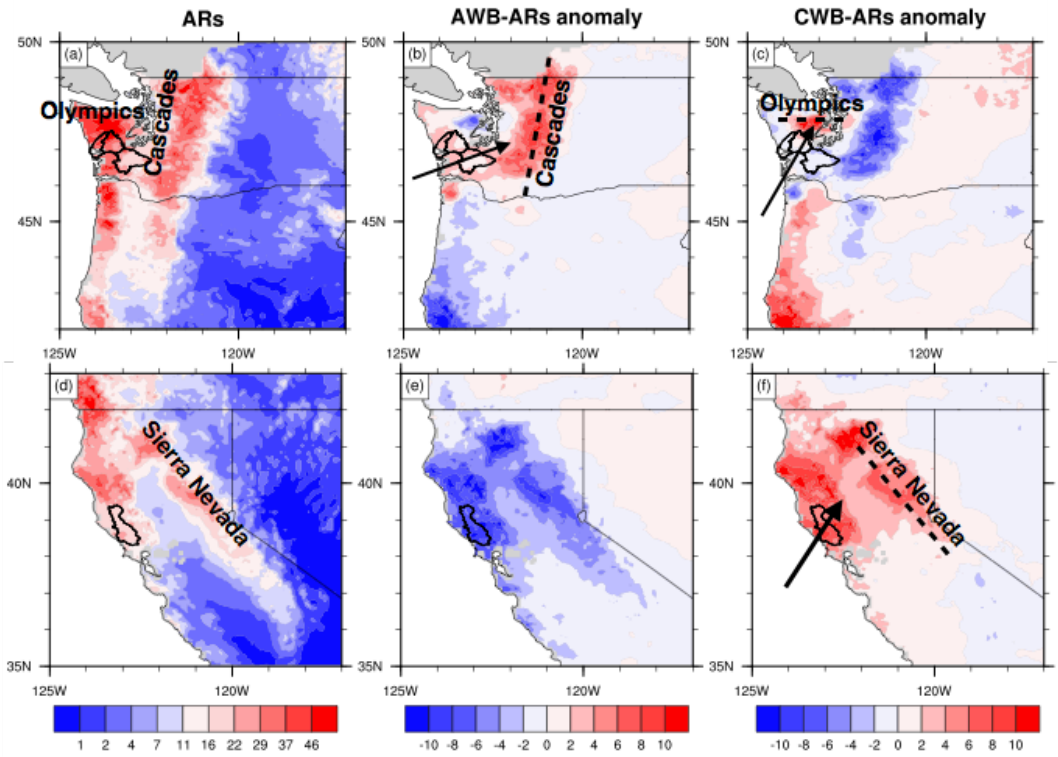

Figure 2-9. (a) Composites of precipitation (converted to mm/day), (b) AWB-AR precipitation anomalies (unit: mm/day) and (c) CWB-AR precipitation anomalies (unit: mm/day) for the northern subset of ARs. (d)~(f) are the same as (a)~(c) but for the southern subset of ARs. The dashed lines suggest he orientation of the mountains, and the arrows suggest the inland impingement of AWB- and CWB-ARs.

thus peak precipitation. AWB-ARs, with more westerly impinging angles, result in positive precipitation anomalies over the Cascades (Fig. 2-9b), meanwhile CWB-ARs, with more southwesterly impingement, contribute mostly to the precipitation over the Olympics (Fig. 2-9c). It is clear from these results that intense precipitation preferentially occurs over mountains where ARs impinge orthogonally (indicated by the sketched lines in Figs. 2-9b and c). Here we assume the impinging angles towards the mountains are very similar to the angles towards the coast, neglecting the local deflection of winds.

In a previous study, Neiman et al. (2011) analyzed four basins in western Washington and constructed composites based on the top 10 extreme events for each basin. The precipitation patterns for the Green river basin located on the western slope of the Cascades and the Satsop river basin draining the southern flank of the Olympics (see Fig. 9 in Neiman et al. 2011) resemble Figs. 2-7b and c respectively. It is reasonable to infer that AWB-ARs are likely to contribute to the top events measured at the site on the western flank of the Cascades (in the Green river basin) while CWB-ARs tend to produce extreme conditions for the site draining the southern Olympics (in the Satsop river basin). In fact, referring to their composites of IVT and near-surface geopotential heights (Fig. 10 and 12 in Neiman et al. 2011), they show the characteristic features of AWB- and CWB-ARs (Figs. 2-4b and c).

A similar relationship between precipitation, AWB- and CWB-AR impinging angles holds for the south-band ARs (Fig. 2-8b) yet with a limited number of AWB-AR events. However, AR-related precipitation in the south band is dominated by CWB-ARs. Positive precipitation anomalies over the Sierra Nevada and other coastal mountains due to CWB-ARs are clearly shown in Fig. 2-9f. As the mountains are oriented along ~140°-320° (Ralph et al. 2013), CWB-ARs impinging at ~25°~50° arrive more orthogonally with respect to the topographic barrier.

Furthermore, CWB-ARs are associated with much higher IVT than AWB-ARs (Fig. 2-5), a phenomenon amplified for the southern ARs.

2.5 Hydrological Impacts on River Basins

The spatial precipitation distribution corresponding to different AR impingement angles can significantly impact the river basin response. In this section, we place particular emphasis on extreme events. First, we investigate how the local precipitation features of two river basins (Chehalis and Russian) within the north and south 5-degree bands are related with impinging angle and IVT features accompanying RWB-ARs. Second, we quantify the relationship of AWB- and CWB-ARs to the extreme streamflow events in the five river basins along the West Coast.

2.5.1 Precipitation in relation to impinging angle and IVT

For the northern ARs (impinge between 44°N~49°N), AWB-ARs result in maximum precipitation over the Cascades whereas CWB-ARs result in maximum precipitation over the Olympics (Fig. 2-9). They both affect the Chehalis basin because the western Cascades drain to the upper Chehalis and the southern Olympics drain toward the lower Chehalis. We thus select the two boxes (b1 and b2 in Fig. 2-1a) over the western Cascades and the southern Olympics, and use 2-day averaged precipitation (averaged for all grids from Livneh gridded precipitation data within each box) of each AR event to establish the relationships between precipitation, impinging angle and IVT (averaged over the lifespan of the ARs; Figs. 2-10a~d).

Extreme precipitation events over the western Cascades are mostly associated with AWB-ARs, especially those with impinging angles between 40° and 80° (Fig. 2-10a). CWB-ARs, having <50° impinging angles, show an increasing precipitation trend with increasing impinging angle as it becomes more orthogonal towards the Cascade Mountains. In terms of IVT, both AWB- and CWB-ARs suggest a positive correlation between IVT strength and precipitation intensity (Fig. 2-

10b). However, the slope of AWB-ARs is larger than CWB-ARs suggesting more efficient transformation of water vapor into precipitation accompanying AWB-ARs with favorable impinging angles. An orthogonal impingement towards the Cascades requires an impinging angle

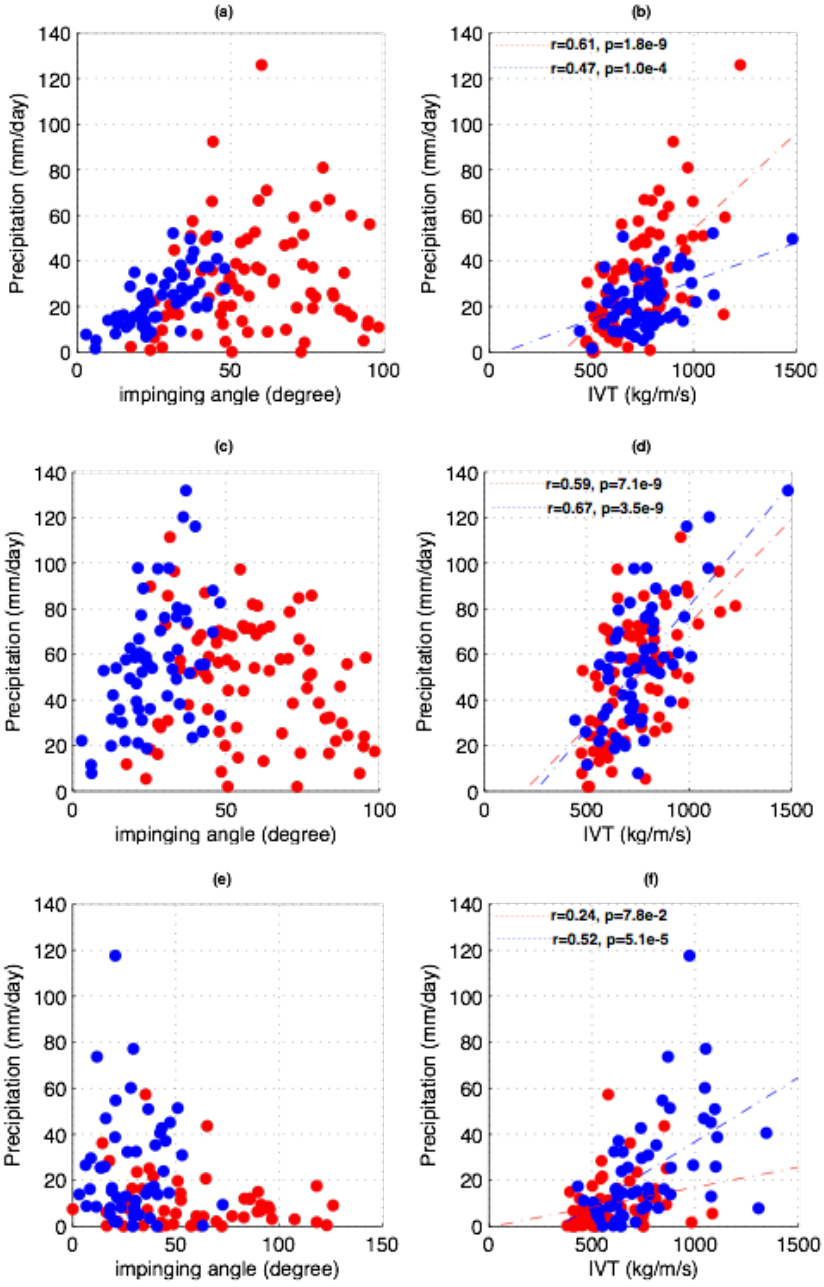

Figure 2-10. Scatterplots of 2-day averaged precipitation (averaged over the three blue boxes in Fig. 2-1a; converted to mm/day) and AR impinging angles: (a) western Cascades (b1 in Fig. 2-1a); (c) southern Olympics (b2 in Fig. 2-1a); (e) upstream Russian (b3 in Fig. 2-1a). Scatterplots of 2-day averaged precipitation (averaged over the three blue boxes in Fig. 2-1a; converted to mm/day) and AR IVT: (b) western Cascades (b1 in Fig. 2-1a); (d) southern Olympics (b2 in Fig. 2-1a); (f) upstream Russian (b3 in Fig. 2-1a).

of 90°~100° (see angle definition in Fig. 2-8), which is different from 40°~80° we see in Fig. 2-10a. Cases with impinging angles of 90°~100° tend to have lower humidity and thus weaker IVT (not shown), as they have advection from higher latitude and dryer conditions. Therefore, while impinging angles could be a limiting factor for IVT when exceeding 90°, more southerly impingement and a stronger IVT (like the ones with CWB-ARs) does not guarantee extreme precipitation over the western Cascades because they are less orthogonal to the mountains.

Over the southern Olympics, however, the majority of the extreme precipitation cases can be attributed to CWB-ARs (Fig. 2-10c) with ~35° of impinging angle. In this case, CWB-ARs have a higher efficiency in transforming water vapor into precipitation with a slightly steeper slope between precipitation intensity and IVT (Fig. 2-10d) than AWB-ARs. The difference between the slopes is not large probably due to the fact that AWB-ARs also produce large amounts of precipitation over the southwestern Olympics.

Similar analysis is repeated for the southern ARs (impinge between 36°N~41°N) on the Russian river basin by selecting a box over its upstream mountains (b3 in Fig. 2-1a). We find that CWB-ARs are predominantly contributing to the extreme precipitation events. CWB-ARs generally have impinging angles less than 50° and those events that induce the most intense precipitation have an average impinging angle of ~40° (Fig. 2-10e). However, in this case CWB-ARs have a much steeper slope between IVT and precipitation intensity than AWB-ARs (Fig. 2-10f), indicating the important role of impinging angle on modulating the AR landfall. Moreover, AWB-ARs generally have weaker IVT, which is consistent with weaker westerly winds moving equatorward and likely associated with weaker EKE.

2.5.2 Extreme streamflow

Finally, we investigate the role of the two RWB-AR types on the most extreme streamflow events for five basins along the West Coast. For each river basin, the top 20 AR-related streamflow events for the 30-year period (1979 Oct~2009 Mar) are selected and attributed to AWB- or CWB-ARs. As expected, the differences in precipitation intensity due to varying impinging angle (shown in sections 2.4.3 and 2.5.1) are the key determinants of the AR type on extreme streamflow. For the Chehalis basin, it is shown that AWB-ARs play a predominant role (Fig. 2-11b) in explaining the top streamflow events measured within the basin. AWB-ARs events are characterized by positive precipitation anomalies over the western Cascades and more efficient production of precipitation from IVT. However, it is also important to note that the number of CWB-ARs causing the top 20 extreme streamflow events measured at stations #8, 9 and 10 is substantial. These stations drain the southern flank of the Olympics, where positive precipitation anomalies are caused by CWB-ARs (see Figs. 2-9c and 2-10d).

In the Russian river basin, CWB-ARs are responsible for most of the extreme streamflow events (Fig. 2-11f). Enhanced precipitation results from CWB-ARs with orthogonal impingement on the coastal California mountains and strong IVT (Figs. 2-9f and 2-10f). CWB-ARs also result in significantly higher streamflow in the Russian basin than AWB-ARs (not shown) while the opposite is not found in the Chehalis river basin.

Three additional basins, the Willamette, Rogue and Eel river basins, located between the Chehalis and Russian basins show a clear transition of the dominant pattern from AWB-AR to CWB-AR on extreme streamflow events (Fig. 2-11). This latitudinal gradient is consistent with the north-south precipitation transition shown in Fig. 2-3. The coastal mountains generally shift from north-south orientation in western Washington to northwest-southeast orientation in northern

California, which favors a more orthogonal impingement of CWB-ARs in the south. In addition, the CWB-ARs are able to maintain the IVT strength moving southward, producing enhanced precipitation during landfall and high streamflows along the southwest coast.

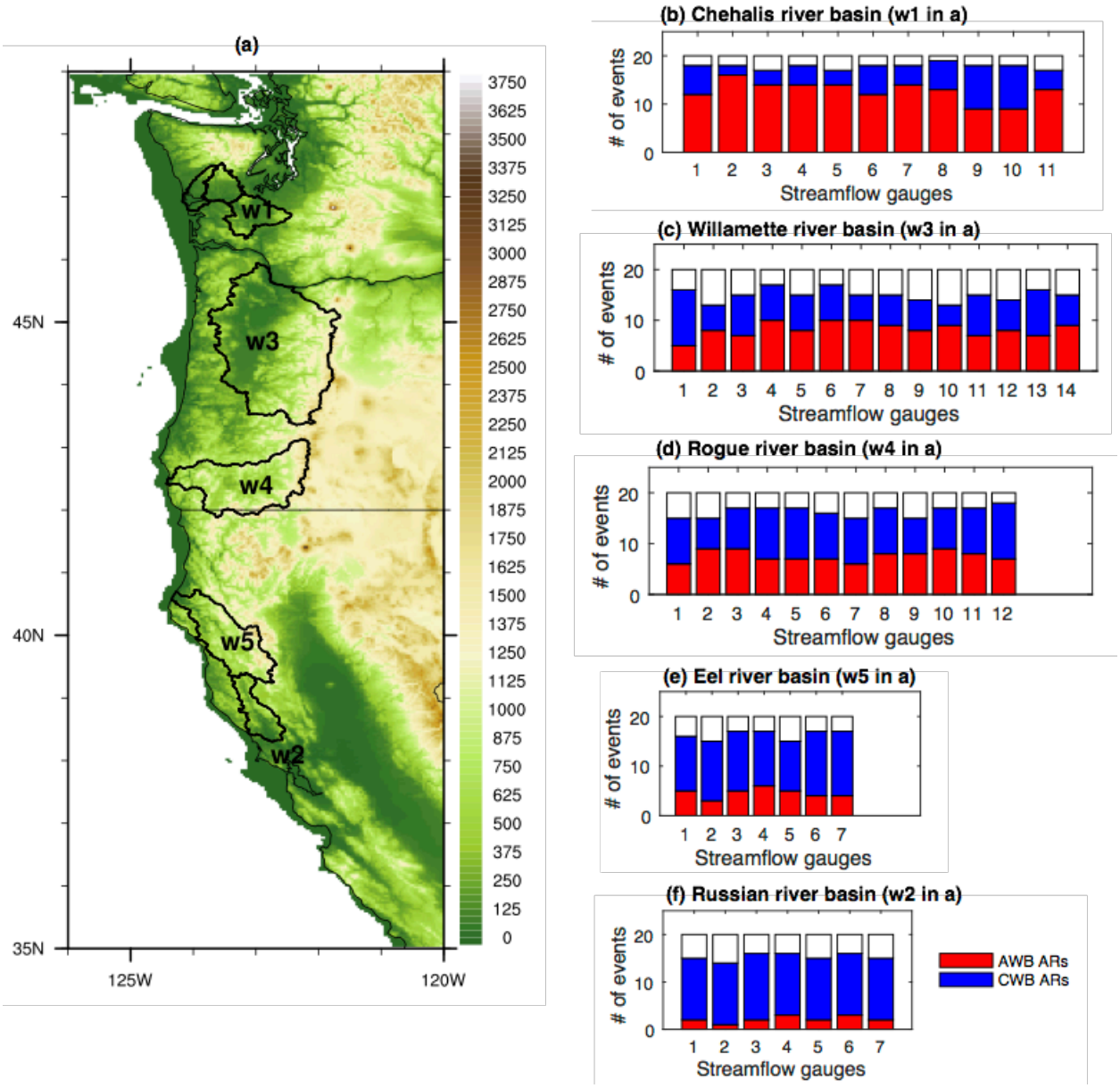

Figure 2-11. Shapes and locations of the five river basins along the West Coast (unit: m; a) and the number of top 20 streamflow events due to AWB- (red) and CWB-ARs (blue) for each USGS streamflow gauges in (b) the Chehalis river basin, (c) Willamette river basin, (d) Rogue river basin, (e) Eel river basin and (f) Russian river basin. The locations of the USGS streamflow gauges are indicated in Figs. 2-1b~f.

2.6 Summary and Conclusions

In this work we bridge the large-scale, upper-tropospheric RWB dynamics with regional hydrological responses through ARs along the U.S. West Coast. Among the total number of AR events, about 2/3 are associated with RWB. The ratio remains the same for all ARs identified for the West Coast (36°N~49°N), and two subsets of ARs that impact the northern and southern parts of the coast (36°N~41°N and 44°N~49°N). AWB-ARs tend to impinge at higher latitudes (>43°N) and have limited meridional movement within their lifecycles. On the other hand, CWB-ARs can travel from high to low latitudes along the coast within their lifespan, likely due to the fact that CWB have more persistent EKE than AWB.

The synoptic features associated with AWB-ARs are characterized by a pronounced surface high to the southeast of the ARs, while CWB-ARs generally have an enhanced surface low to the northwest of the ARs. CWB-ARs are shown to have significant larger moisture transport in the lower-troposphere than AWB-ARs (shown schematically in Fig. 2-12), mainly attributable to stronger winds. The strengthened winds in the lower troposphere of CWB-ARs are observed from the coast to ~1500 km into the Pacific Ocean along the IVT axes. When compared to AWB-ARs, CWB-ARs show much broader regions of ascent, extending hundreds of miles away from the coast. This is consistent with the stronger vertical eddy heat fluxes seen in the mature stage of CWB. In contrast, the ascent region of AWB-ARs is more spatially confined to the coast, suggesting a major orographic lifting effect. This is also consistent with the findings of Ryoo et al. (2015), where coastal ascent and anticyclonic trajectories, linked mostly to the AWB, lead to greater precipitation over the northwest coast.

As a result of the very different large-scale and synoptic features, AWB- and CWB-ARs result in different spatial patterns of precipitation and streamflow along the western coast. While precipitation is positively correlated with IVT, we find that the efficiency of converting water vapor into precipitation depends on the angle of impingement (Fig. 2-12). More orthogonal impingement results in higher efficiency. The impinging angles calculated from IVT show that AWB-ARs are characterized by more westerly impingement of IVT toward the coast, while CWB-ARs generally impinge the coast in a southwesterly direction. Consequently, the ARs will impinge on the local topography at a very different angle (assuming the angle doesn't change significantly from the coast).

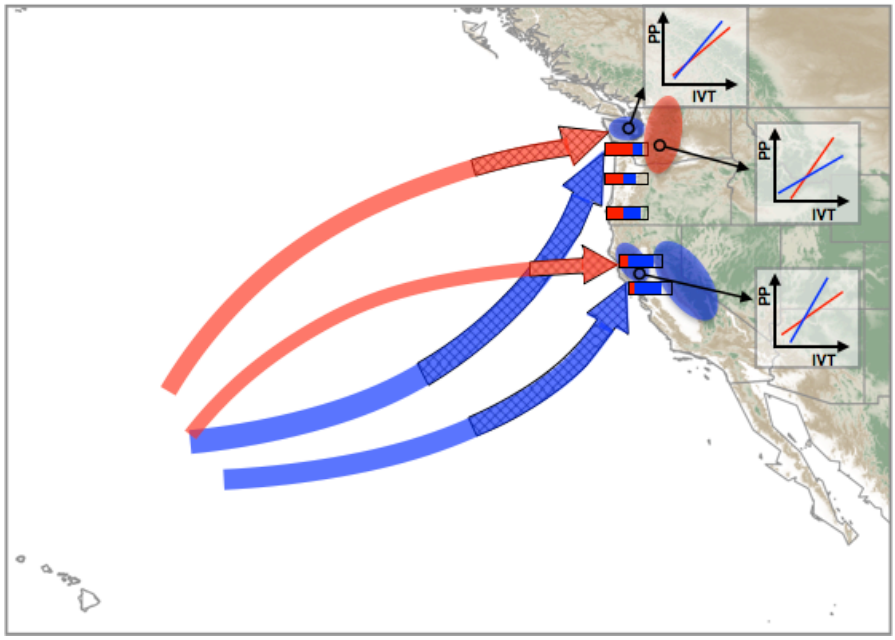

Figure 2-12. Schematic showing the averaged maximum IVT axes of AWB- (thick red curves) and CWB-ARs (thick blue curves) impinging toward the northern and southern coast of the U.S. (impinging angles suggested by the directions of the thick arrows). The thicknesses of the red (blue) axes suggest the magnitude of the averaged IVT magnitude associated with the AWB-ARs (CWB-ARs). The hatched part of the thick arrows suggest where ascending occur (omega < -0.1 Pa/s at 750mb) along the IVT axes. Red (blue) shaded ellipses suggest where positive precipitation anomaly is resulted from AWB-ARs (CWB-ARs). The compositions of the basin-averaged extreme streamflow events due to AWB-ARs (red bars) and CWB-ARs (blue bars) are shown by the horizontally aligned bars over the general basin locations. The efficiencies of AWB-ARs (CWB-ARs) in converting IVT to precipitation (or PP), obtained from the locations of the black circles, are shown by the slopes of the red (blue) lines in the x-y plots.

Along the northwestern U.S. (Washington and Oregon), the Cascade Mountains are oriented in a north-south direction and experience higher than average precipitation during AWB-ARs. It is important to note that the optimal impinging angle for AWB-ARs to the Cascades is 40°~80° but not 90°~100° - an ideally right angle to the mountain ranges. This is because, in our period of analysis, the AR events with 90°~100° angles tend to have lower humidity and weaker IVT as the advection is from relative higher latitudes. However, not all region in the northwest show predominantly AWB-AR precipitation. A notable exception is the enhanced precipitation over the more east-west oriented Olympic Mountains, which is predominantly affected by CWB-ARs. Accordingly, extreme streamflow events measured by the gauges in the upper Chehalis basin (draining the western Cascades) can be mostly attributed to AWB-ARs, but several gauges draining the southern Olympics within the Chehalis basin show clear signals of CWB-ARs' impact on extreme streamflow. Moving south from the Chehalis, the Willamette, Rogue and Eel river basins show progressively larger impacts of CWB-ARs on streamflow (Fig. 2-12). This is consistent with the latitudinal gradient of precipitation associated with AWB and CWB-ARs.

Along the southwest U.S. coast (northern California), CWB-ARs tend to impinge normally towards the northwest-southeast oriented mountains. In addition, over coastal California CWB-ARs are associated with stronger IVT while the strength of AWB-ARs decays rapidly at lower latitudes. These factors combined lead to greater precipitation associated with CWB-ARs along the southwest coast. As a result, in the Russian River basin of northern California, the majority of the extreme streamflow events are associated with CWB-ARs.

In this work, we focus primarily on the dynamical features associated with ARs in the upper troposphere – namely RWB - and how these features can modulate AR precipitation and associated streamflow along the West Coast. We find that AR wind direction and strength are the primary

drivers of IVT intensity, extreme precipitation and streamflow events. However, thermodynamic factors, such as temperature and moisture origin are very important to AR strength. For instance, the multi-scale AR event analyzed by Ralph et al. (2011) is marked by direct advection of water vapor from the tropics into the southern portions of the AR, as seen from satellite and dropsonde measurements. This tropical origin could contribute to the extreme nature of the event. Another extreme AR-related flooding case reported by Neiman et al. (2011), characterized by entrainment of tropical moisture, had anomalously warm condition that resulted in more-than-usual liquid form precipitation. The thermodynamical factors are particularly important for basin-scale flooding, because these could significantly modify the rain-snow partitioning of total precipitation. Greater than normal rain-snow partitioning can result in greatly enhanced runoff volume (White et al. 2002; Lundquist et al. 2008; Neiman et al. 2011) and could potentially lead to rain-on-snow events (Leung et al. 2004; Leung and Qian 2009). One way to examine the connections between moisture sources, thermal advection and rain-snow partitioning - varying with climate change - is to employ finer-resolution regional models and numerical tracer tools (Sodemann and Stohl 2013) to evaluate the 3-dimensional characteristics of vapor transport. This will be the topic of a future study.

In summary, depending on the associated RWB type, ARs impinge on the local topography at a different angle and have a different spatial signature of precipitation and streamflow. Our results demonstrate that large-scale, upper-tropospheric dynamics can strongly modulate AR features and regional hydrologic impacts. Having established the link, questions related to how regional hydrologic impacts associated with ARs could change in a warmer climate could be investigated.

CHAPTER 3: THE EXPORT OF TROPICAL MOISTURE ON ATMOSPHERIC RIVERS' VAPOR TRANSPORT AND LANDFALL

Some atmospheric rivers (ARs) that have caused severe flooding over the U.S. West Coast have been characterized by a "tropical connection" as captured by satellite imagery. However, the contribution of tropical moisture export and local moisture convergence to ARs is under debate. To establish a robust understanding of the contribution of tropical moisture on AR strength and to investigate the associated meso-scale mechanisms, we simulated 29 AR events, selected as the top 15% of ARs affecting the Northwest based on their vapor transport intensity. We used the water vapor tracer tool embedded in WRF (WRF-WVT). The WVT is used to "tag" moisture from the tropics and it helps to provide a joint view of tracer moisture (that from the tropics) and total moisture in ARs' lifecycles.

From an AR case study in Jan 23, 1982, we found a positive feedback system along the cold front that intimately interconnects with tropical moisture: 1) the narrow line-convection over the cold front is mostly from tropical moisture; 2) the latent heat release associated with the cold-frontal precipitation induces positive potential vorticity that helps enhance low-level jet (LLJ) that is pre-frontal; 3) the enhanced LLJ in turn enhances entrainment of tropical moisture to this AR. We also found significant "mutual amplification" near the warm front where most landfall is generated. It is achieved through strong warm air advection ahead of the tropical moisture arrival that helps to enhance low-level moisture convergence and the vertical ascent (in other words, an enhanced ageostropic circulation). These processes associated with tropical moisture are confirmed by other simulated cases. We found increasing trends of cold-frontal precipitation and latent heat generated potential vorticity in line with enhanced LLJ. This also leads to enhanced

moisture export from the tropics into leading edges of ARs and stronger warm air advection inland. However, no significant amplification of the ageostrophic circulation is found in those ARs with >25% contribution of tropical moisture to inland precipitation comparing with those <25%, suggesting the role of other dynamical factors in modulating ARs' precipitation strength. These mechanisms linking tropical moisture to AR intensity can provide important implications for possible AR strength change in a warming climate where tropical moisture is expected to increase significantly.

3.1 Introduction

Atmospheric rivers (ARs) are one of the key hydrometeological phenomena that affect the U.S. West Coast in winter (Ralph et al. 2011). ARs—narrow corridors in the atmosphere that transport great amount of water vapor towards the coast—account for over 50% of cool-season precipitation along the West Coast (Rutz et al. 2014). Consequently, ARs are important contributors to water resources for these coastal regions, yet they are also the fundamental reason for many floods in coastal basins (Ralph and Dettinger 2011; 2012). As an example, Neiman et al. (2008b) recorded a particularly intense AR that affected the Pacific Northwest on 6-7 November 2006. This event resulted in severe flooding with maximum 1-day streamflow among the top 1% of historical streamflow measurements in November for those gauges draining the coastal mountains and Cascades in western Washington. The extreme nature of this event has been attributed to the AR signature that connect the moisture pool of tropical eastern Pacific towards the coastal lands in western Washington (Neiman et al. 2008b; 2011). This type of tropical-extratropical link, often striking in satellite imagery, has been associated with higher likelihood of extreme hydrological impacts associated with ARs (Ralph et al. 2011; Neiman et al. 2011). This

is because the entrainment of tropical moisture is assumed to facilitate stronger vapor transport and warm temperature advection within ARs, leading to stronger precipitation and potentially triggering rain-on-snow, both of which can increase streamflow responses (e.g. White et al. 2002; Lundquist et al. 2008; Neiman et al. 2011).

However, it is under debate whether ARs' moisture and their subsequent landfall are substantially affected by tropical moisture. Dynamically, an air parcel from the tropics entrained into the subtropical extension of an AR can rainout the tropical moisture along its poleward track, but can also uptake local evaporation from the extratropics (Knippertz and Wernli 2010). In addition, the AR feature can be largely maintained by the convergence of extratropical moisture in association with the frontal systems that ARs are often associated with (Bao et al. 2006; Dacre et al. 2015). However, case studies using the moisture "tagging" technique in reginal climate models (RCMs) confirm the contribution of tropical moisture exports (TMEs) to coastal landfalls through the analysis of several extreme AR events (e.g. Sodemann and Stohl 2013; Eiras-Barca et al. 2017). Moisture tagging within RCMs is perhaps the best alternative to quantify moisture contributions from tropical and extratropical sources in ARs because of the interplay of physical processes that range from large to fine spatio-temporal scales which cannot be captured by coarse resolution models (Sodemann and Stohl 2013; Rios-Entenza and Miguez-Macho 2013; Dominguez et al. 2016). However, previous studies have focused on individual case studies and these isolated ARs do not allow for an establishment of a robust relationship between TME and AR features.

Understanding how moisture from the tropics interacts with AR features can help us anticipate changes in AR-related precipitation extremes in response to TME changes (Trenberth 1999; Sodemann and Stohl 2013). It is especially true in the context of climate variability and change

that can affect tropical moisture characteristics. Bao et al. (2006) found that direct poleward transport of tropical moisture by ARs is more likely to happen in El Niño-Southern Oscillation (ENSO) neutral years while it is less likely to occur in the El Niño years. In addition, tropical moisture is expected to increase in line with the Clausius-Clapeyron relationship with global warming (Meehl). In order to advance our understanding of potential changes in AR-related extreme precipitation, which can have significant social-economic impacts, it is important to understand the interactions between TME and AR features in our current climate.

The goal of this study is to investigate the role of TME on ARs' thermodynamic processes and the consequent landfall, with a particular focus on extreme events. To achieve this goal, we simulate 29 AR events with the top 15% vapor transport strength that affected the U.S. Northwest Coast using the Weather Research and Forecast model (WRF) and numerically "tag" the tropical moisture using the water vapor tracer (WVT) tool embedded in WRF (WRF-WVT). The joint view of tropical moisture and total moisture allows us to (1) identify the key processes that involve TME in association with ARs' evolvement and the resultant precipitation, and (2) characterize these processes according to the contributions from TME to the extreme ARs with top 15% IVT strengths.

3.2 Method and Datasets

3.2.1 AR samples

With a particularly interest in extreme events, we select a subset of ARs affecting the U.S. Northwest Coast according to their intensity of vapor transport. Hu et al. (2017) identified a total of 192 AR events reaching the Northwest Coast (44°N - 49°N) in 1979-2009 winters. These events are all characterized by strong vertically integrated vapor transport (IVT), span more than 2000 km in length and last longer than 18 hours (see more details in Hu et al. 2017). We rank these 192

ARs by their daily maximum IVT averaged over 44°N - 49°N along the 124.7°W meridian (the mean of the 192 events is 524.1 kg/m/s) and select the top 15% of events as our simulation sample. Therefore, we simulate a total number of 29 AR events with the greatest daily IVT strength (ranging from 670.9 to 1136.5 kg/m/s).

3.2.2 WRF-WVT

We use the WRF-WVT tool to simulate the 29 events. Unlike traditional WRF simulations, this tool employs an extra WVT module to numerically "tag" moisture that originates from a targeted three-dimensional region (the tropics in this case) as tracers and track their subsequent movement in space and time. The tracers are treated in the same way as moisture in the simulation, allowing a full consideration of all physical processes affecting atmospheric moisture such as advection, molecular and turbulent diffusion, convection and cloud microphysics represented by WRF (see more details in Insua-Costa and Miguez-Macho 2018). Therefore, the behavior of WVTs, representing a portion of total moisture in WRF, depends on the representation of the dynamics and physics in WRF. The physical parameterization scheme used in WRF-WVT are: YSU PBL scheme (Hong and Pan 1996), WSM6 microphysics scheme (Hong and Lim 2006), the Kain-Fritsch (Kain 2004) convective parameterization (only used for the outer domain). In addition, we use ERA-Interim (Dee et al. 2011) reanalysis as the initial and boundary conditions to drive WRF-WVT and spectral nudging (Miguez-Macho et al. 2004) is applied.

The simulation domains are shown as Figure 3-1b. The outer domain (domain 01; 15km grid spacing) is used to cover the AR extension and the inner domain (domain 02; 3km grid spacing) can resolve finer-scale processes that are important for precipitation generation during landfall (Neiman et al. 2011; Houze 2012; Hu et al. 2017). We use WVTs to "tag" moisture that exists in the atmosphere with latitudes lower than 25°N as tracers (the 3-D space above the hatched area),

and denote the transport of this moisture as tropical moisture export (TME). Using this method, TME only accounts for the export of tropical moisture crossing the 25°N "wall" in the domain (black dashed line), without accounting for other moisture that could originate in the tropics and enter the domain through other lateral boundaries. For each event we perform a 10-day simulation to account for the initiation and the associated landfall processes. The duration of the selected ARs ranges from 20 to 130 hours.

3.2.3 Other gridded datasets

To evaluate the biases in WRF simulations and their effects on interpreting tracers, we use two additional observation-based datasets: (1) NASA Modern-Era Retrospective Analysis for Research and Application (MERRA; Rienecker et al. 2011) to evaluate WRF-WVT in representing AR moisture transport features; and (2) Livneh gridded daily precipitation data (Livneh et al. 2013) derived from ~20000 NOAA Cooperative Observer Stations across the conterminous U.S. (1/16° latitude/longitude resolution) to evaluate model simulated precipitation after landfall over the western Washington (domain 02).

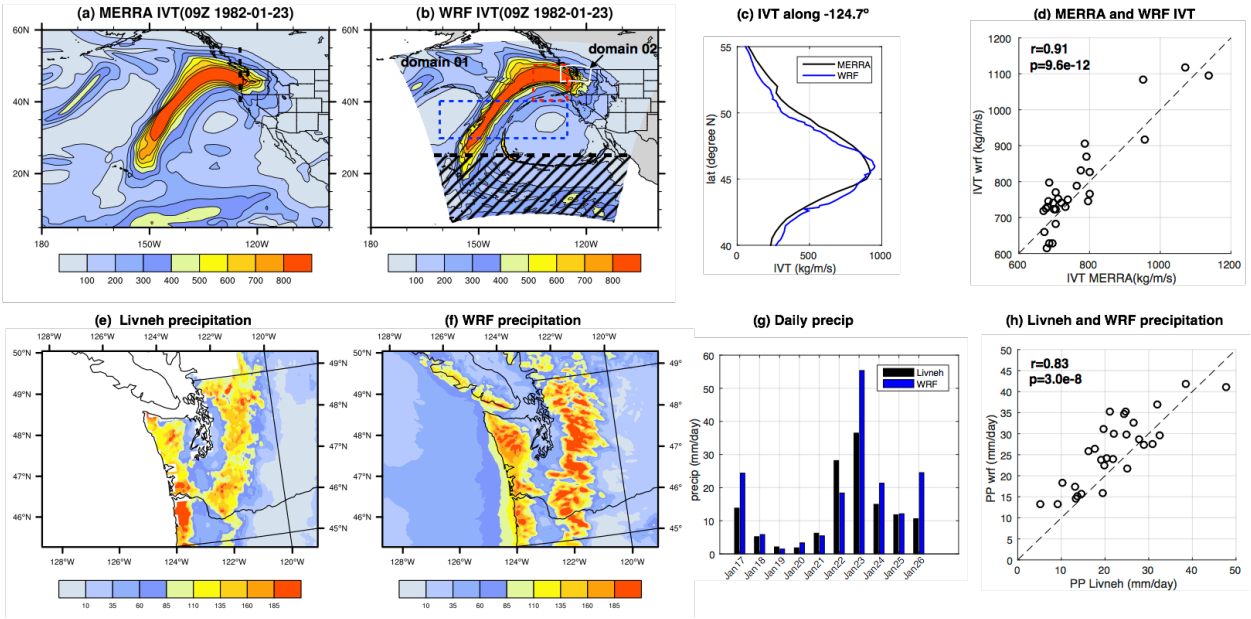

Figure 3.1. Spatial pattern of vertically integrated vapor transport (IVT; unit: kg/m/s) at 09Z Jan 23, 1982 from MERRA (a) and WRF-WVT simulation (b). (c) IVT at 09Z Jan 23, 1982 between 40˚N and 55˚N along 124.7˚W from MERRA and WRF-WVT simulation. (d) Comparison of daily maximum IVT (44˚N - 49˚N along 124.7˚W) for the 29 simulated ARs between MERRA and IVT. Spatial pattern of 2-day accumulated precipitation (Jan 22 and 23, 1982; unit: mm) in domain 02 from Livneh dataset (e) and WRF-WVT simulation (f). (g) Daily precipitation averaged over land in domain 02 from Livneh and WRF-WVT simulation. (h) Comparison of 2-day maximum precipitation (averaged into mm/day) over the terrestrial area in domain 02 for the 29 simulated ARs between Livneh and WRF-WVT simulation. (b) also shows the simulation domain 01 and domain 02 (the same domain shown in e and f), and the dashed blue and red boxes indicate the area used to investigate cold and warm front features.

3.3 AR case on Jan 23, 1982

To examine the mesoscale processes of ARs in association with TME, we present a case study that occurred Jan 23, 1982. This AR has a daily maximum IVT (averaged from 44°N - 49°N along the 124.7°W meridian) of 698.71 kg/m/s on Jan 23, 1982 and is responsible for precipitation that occurred in the Northwest Coast from Jan 21 to Jan 23, 1982. We simulate this AR event covering a 10-day period from 00Z 1982-01-17 to 00Z 1982-01-27. This case is characterized by considerable contribution from tropical moisture in both moisture and precipitation when it arrived the coast (~50%) and reveals an AR's lifecycle that is generally representative of other ARs.

3.3.1 Evaluation of AR simulation

To evaluate model uncertainties in reproducing this AR, we compare the simulated AR pattern and the resulting precipitation with the observation-based datasets. Figures 3-1a and b show the IVT pattern at 09Z Jan 23, 1982 (the time step with peak IVT) from MERRA reanalysis and the WRF-WVT simulation. Very similar spatial pattern and magnitude of IVT are observed. To zoom in the IVT strength just off the Northwest Coast, Figure 3-1c also shows a very similar IVT variation along the 124.7W longitude from 40°N to 55°N.

Figures 3-1e and f show the 2-day accumulated precipitation (Jan 22nd and Jan 23rd, 1982) over domain 02 from the Livneh data and the simulation. While strong precipitation is consistently maximized over the Cascades and the coastal mountains to the west, overestimation of precipitation for these two days from WRF-WVT is obvious (14.1% overestimation averaged over the terrain in domain 02). In fact, this overestimation is generally observed throughout the simulation period (Fig. 3-1g). This is likely due to a combined effect of model deficiencies and biases in the Livneh data over the mountains where observations are limited (Dominguez et al. 2018). Similarly, for the 29 simulated ARs, we evaluate our WRF-WVT simulations in terms of IVT strength off the Northwest Coast (44°N and 49°N along 124.7°W) and landfall in domain 02. Figure 3-1d shows similar daily IVT strengths between WRF-WVT simulations and MERRA with a mean of percentage differences of 2.9%. For 2-day maximum precipitation in domain 02, WRF-WVT generally overestimates the precipitation comparing to the Livneh dataset (Fig. 3-1h) with a mean of percentage differences of 26.2%. Overall, the WRF-WVT simulations realistically capture ARs' IVT strengths and reasonably capture the spatial patterns of the coastal rainfall over Western Washington, but overestimates the precipitation.

3.3.2 TME - AR interactions

We now focus on the role of TME in association with the development of this AR. At the initiation stage of this AR (Jan 20th - Jan 22nd), tropical moisture entrains into the subtropical portion of this AR transported by southerly winds (Figs. 3-2a and b). Figures 3-2c and d show a vertical cross-section from 163°W to 140°W averaged over 27°N - 32°N at 12Z Jan 20 with color-shading indicating total moisture (Fig. 3-2c) and tracer moisture (Fig. 3-2d). It clearly reveals that moisture exported from the tropics is concentrated towards the core of this AR (~159°W) and accounts for the majority of moisture there (>70%). In the context of frontal system structures that usually accompany ARs, the AR core collocates well with the pre-cold-frontal low-level jet (LLJ; indicated by the gray contours in Figs. 3-2c and d), especially at the western boundary of the LLJ where narrow and convective rainbands often occur (Browning 1985; Lackmann 2002). Consequently, the precipitation along the cold-frontal rainbands associated with this AR comes almost entirely from the tropics (not shown). Meanwhile, the latent heat released from the narrow rainbands induces positive potential vorticity (PV) especially at the lower levels. Figures 3-2c and d show areas of strong latent heating induced PV (LHPV) calculated by the equations from Emanuel et al. (1987). This low-level positive PV maxima has the elongated feature that extends along the cold front at the west boundary of the LLJ (see blue contours in Figs. 3-2a and b), which can in turn intensify the strength of pre-cold-frontal LLJ due to its cyclonic circulation pattern. As a result, this enhanced LLJ can increase TME along the AR. Therefore, we find that a critical positive feedback mechanism observed along the cold front: tropical moisture is entrained along the cold front through the LLJ and contributes to convective narrow rainbands, which induce PV maxima through latent heat release and enhances the LLJ and tropical moisture export to higher latitudes. Our results suggest that tropical moisture plays an important role in intensifying the LLJ

and in turn, the enhanced LLJ induces further poleward export of tropical moisture along the AR. In fact, Lackmann (2002) shows that the cold-frontal PV anomaly can account for ~40% of LLJ

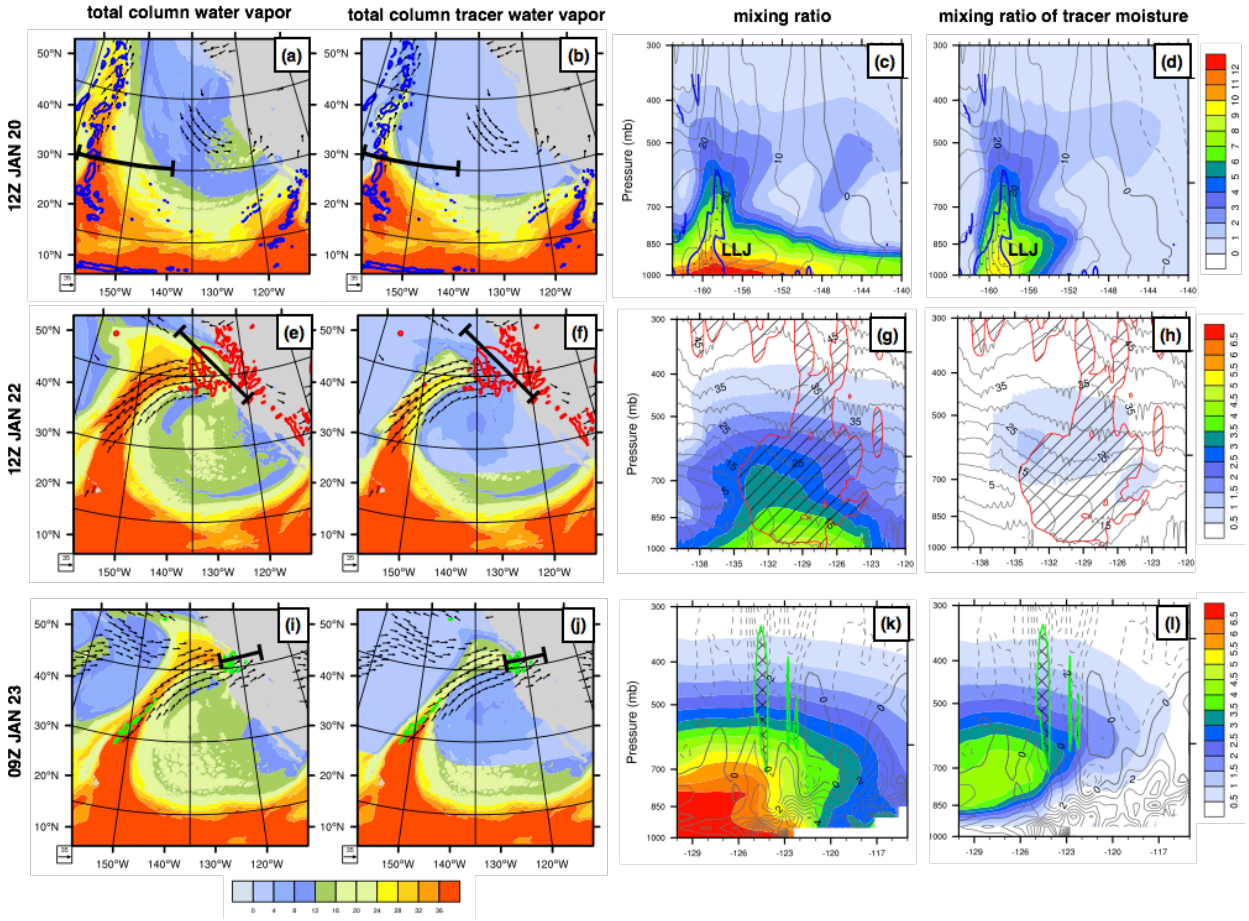

Figure 3-2. Moisture transport features at 12Z Jan 20, 1982 (a - d), 12Z Jan 22, 1982 (e - h) and 09Z Jan 23, 1982 (i - l). (a), (e) and (i) show total column water vapor for total moisture and (b), (f) and (j) show total column water vapor for tracer moisture (color-shaded; unit: kg/m^2 using the colorbar at the bottom), with wind vectors showing 800-950mb averaged winds where wind speeds > 20 m/s. (c) shows the vertical cross-section from 163°W to 140°W averaged in 27°N - 32°N (location indicated by the black line in a and b) with mixing ratio color-shaded (unit: g/kg; colorbar on the right), areas with latent heat induced PV >0.5 PVU/day stippled and contoured by thick blue lines and meridional winds contoured by gray lines. (d) is the same as (c) but with mixing ratio of tracer moisture color-shaded. (g) shows the vertical cross-section from 55N, 140W to 40N, 120W (indicated by the black line in e and f), mixing ratio color-shaded (unit: g/kg; colorbar on the right), area with WAA > 0.2 K/hr hatched and contoured by thick red lines and wind speed contoured by gray lines. (h) is the same as (g) but with mixing ratio of tracer moisture color-shaded. (k) shows the vertical cross-section from 130W to 115W averaged in 45N - 50N (location indicated by the black line in i and j) with mixing ratio color-shaded (unit: g/kg; colorbar on the right), area with vertical wind > 0.2 m/s hatched and countered by thick green lines and mass convergence contoured by gray contours (unit: 1/day; solid contours indicate positive values and dashed contours indicate negative values). (l) is the same as (k) but with mixing ratio of tracer moisture color-shaded. Blue, red and green contours in (a), (b), (e), (f), (i) and (j) indicates area with strong low-level (800 - 950mb) latent heat induced PV (>1.0 PVU/day), 500 - 950 averaged WAA (>0.2 K/hr) and 500 - 700mb averaged upward motion (>0.2 m/s), respectively. Note that in (a) and (b), low-level latent heat induced PV are masked out for areas with total column water vapor <24 kg/m^2 to show the LLJ-relevant PV features.

strength derived from PV inversion. This feedback mechanism involving TME, PV anomaly and LLJ is observed throughout this AR's lifecycle.

The subsequent poleward transport of tropical moisture generally follows the isentropic surfaces that slope upward. Approaching the warm front near the Northwest Coast, tracer moisture at 12Z Jan 22 is located in the mid-level (500 - 700m; Fig. 3-2h), while most of lower-level moisture (from surface to 700mb) is from extratropical moisture. Meanwhile, strong warm air advection (WAA) is observed in 1000 - 500mb levels due to the warmer-than-average nature of tropical air. In a plan-view, WAA is maximized at the leading edge of this AR (red contours in Figs. 3-2e and f) where the greatest temperature gradients occur. Strong WAA has important dynamical implications due to its effects on enhancing ageostrophic circulation in association with extratropical cyclone development and the consequent synoptic ascent that indicates precipitation. Indeed, consistent synoptic-scale low-level convergence is observed at 09Z Jan 23 over domain 02 (Figs. 3-2k and l) when peak precipitation occurs. While synoptic ascent is dominant over domain 02 (green contours in Figs. 3-2i and j), it is maximized over the coastal mountains (at 124°W and 122°W) indicating the role of topography on mesoscale features of precipitation distribution. At the same time, upper-level divergence is indicated by Figures 3-2k and l (dashed grey contours at upper levels), showing a picture of the ageostrophic circulation at the leading edge of this AR. Peak of total moisture and tracer moisture in domain 02 also occur at 09Z Jan 23rd (Fig. 3-3a). The enhanced low-level convergence explains the important contribution of local moisture (as opposed to tropical moisture) to this AR at lower levels, below 800mb (Fig. 3-3b). However, tropical moisture contributes significantly to mid-level moisture (Figs. 3-2l). Because vertical ascent is maximized in mid-levels that is responsible for generating precipitation, tropical moisture

has a slightly larger contribution to domain 02 precipitation (53.5%) than its contribution to precipitable water (47.9%) at 09Z Jan 23rd.

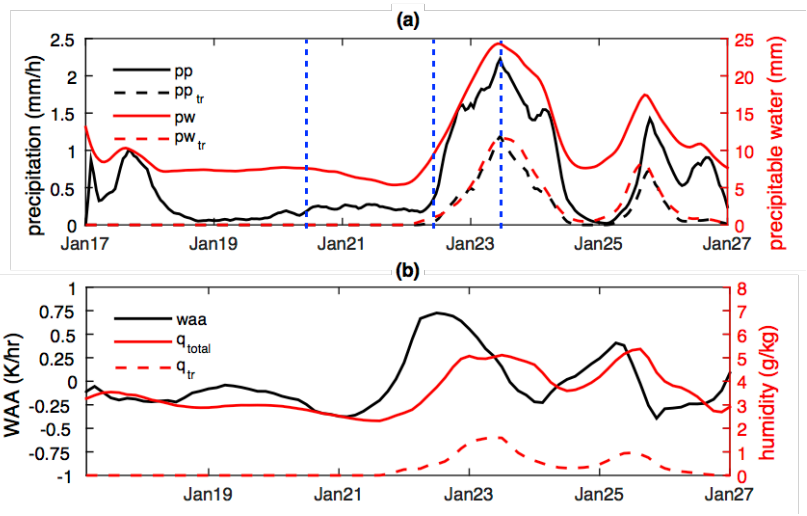

Figure 3-3. (a) Time series for domain 02-averaged precipitation (black; use the left y axis) and precipitable water (red; use the right y axis), with the total value shown by solid lines and the tracer value shown by dashed lines. (b) Time series for WAA (black; use the left y axis)and low-level averaged mixing ratios for total moisture (red solid) and tracer moisture (red dashed; using the right y axis) averaged in 800 - 950mb and red box in Fig. 3-1b. (a) also indicates the 3 time steps shown in Fig. 3-2 by blue dashed lines.

In summary, the joint analysis of total moisture and tracer moisture has allowed us to examine the role of TME in this particular AR at different stages of its development and at different geographical locations along its path. Along the cold front, TME produces cold-frontal rainbands that enhance LLJ through latent heat induced PV maxima, which in turn enhance the export of tropical moisture along the AR. Near the warm front, the thermal characteristics of TME, represented by strong WAA, enhance local moisture convergence and vertical ascent (i.e. the ageostrophic circulation). As a result, tropical moisture contributes 44.7% of this AR's landfall on Jan 23rd when daily maximum precipitation occurs.

3.4 TME-AR features in all simulated cases

While the AR case described above presents interesting dynamics and thermodynamics associated with TME, the next question is, how generalizable are these features? As described in Section 3.2.1, we simulated 29 AR events representing the most intense 15% of events in terms of daily IVT intensity for the period 1979 to 2009. Therefore, the simulated 29 AR events all have

daily IVT ≥ 670.9 kg/m/s (85% percentile IVT value; averaged between 44°N and 49°N along 124.7°W). While AR-precipitation intensity in general increases with IVT strength, precipitation intensity can also be significantly affected by other factors (Neiman et al. 2008a; Ralph et al. 2011). As a result, the simulated 29 events, despite capturing the largest IVT, show large variations in their associated 2-day maximum precipitation (Fig. 3-1h).

From the WRF-WVT simulations, we are able to quantify the contribution of tropical moisture to each AR. According to the contribution to the precipitation over domain 02 on the date with peak daily precipitation, we group these 29 events into 2 categories: 1) 16 AR events with significant tropical moisture contribution (≥25%; TME-ARs) and 2) 13 AR events without significant tropical moisture contribution (<25%; NTME-ARs). We select the 25% threshold to divide the sample size evenly in general (tropical contributions for TME-ARs are further indicated by yellow and red fills to indicate below and above 50% threshold in Fig. 3-4). Our goal is to examine the different features in these two groups in their initial and landfall stages according to the different contributions from tropical moisture.

3.4.1 Cold frontal features

To account for the cold-frontal features that may initiate TME before tropical moisture can actually reach the Northwest Coast, we quantify the LLJ strength and cold-frontal precipitation features over the upstream Pacific Ocean (the blue dashed box in Fig. 3-1b, 30°N - 40°N and 160°W - 125°W) within the 3-day period before the peak precipitation in domain 02 occurs. The 29 events clearly show a positive correlation between LLJ strengths (800 – 950mb levels) and cold-frontal precipitation with a correlation coefficient of 0.80 (Fig. 3-4a). More importantly, TME-ARs have stronger LLJs than NTME-ARs. The stronger LLJ is due, in part, to stronger PV anomalies induced by the latent heat release due to cold-frontal precipitation (Fig. 3-4b), consistent

with the cold-front positive feedback mechanism described in the AR case on Jan 23, 1982. Note that we divide the TME-ARs according to the contribution of tropical moisture to precipitation in domain 02, Figure 3-4a actually suggests that stronger LLJs in the upstream Pacific before ARs' arrival indicates larger TME and possibly lead to larger contribution of moisture from the tropics to ARs' precipitation. This can be used for forecasting purposes in order to infer the contributions from tropical moisture to ARs and their inland impacts given their thermal and landfall features.

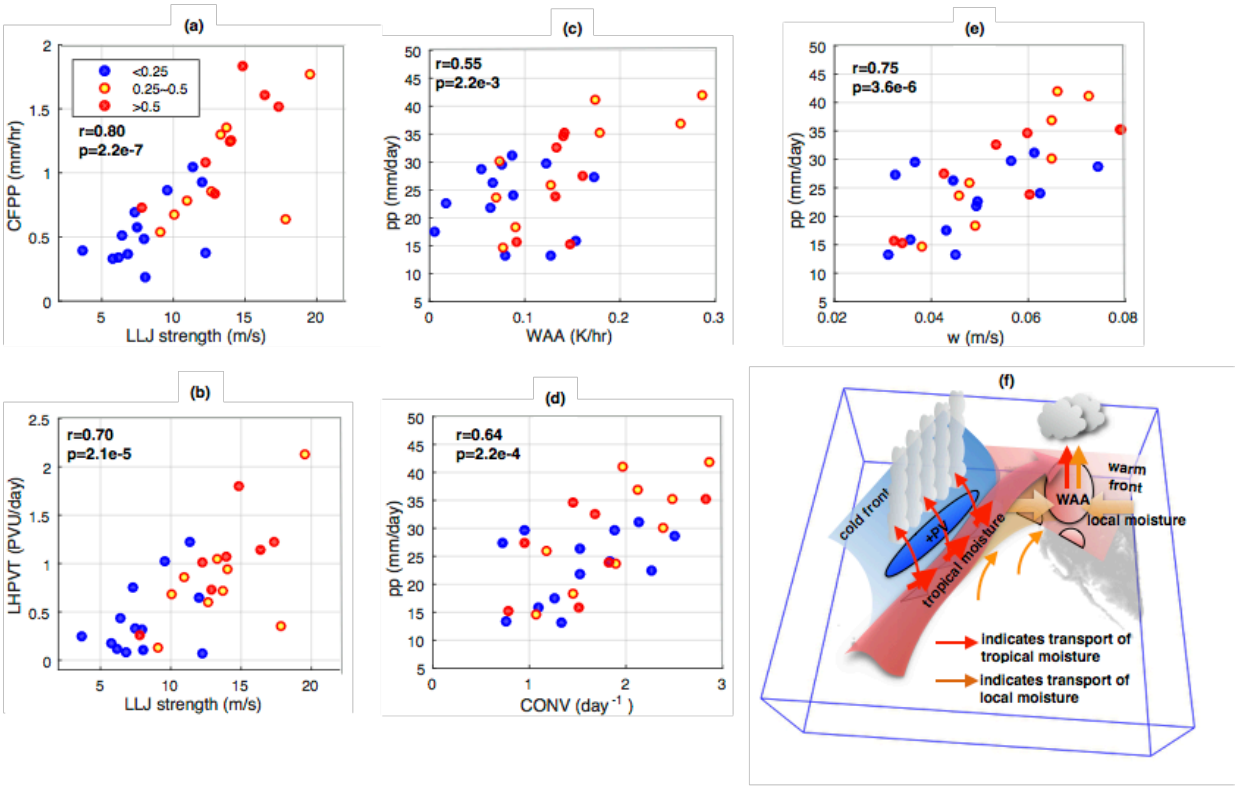

Figure 3-4. (a) Relationships between LLJ strength (800 - 950 mb) and cold-frontal precipitation within 3-day period before the peak landfall (in domain 02) time step in the blue dashed box in Fig. 3-1b. (b) Relationships between LLJ strength (800 - 950mb) and latent heat induced PV tendency (800 - 950mb) within the 3-day period before the peak landfall time step in the blue dashed box in Fig. 3-1b. (c) Relationships between WAA (500 - 950mb) within the 2-day period before the peak landfall time step averaged in the red dashed box in Fig. 3-1b and 2-day maximum precipitation in domain 02 (averaged to mm/day). (d) Relationships between domain 02-averaged low-level convergence (750 - 950mb) on the date with daily maximum precipitation and the 2-day precipitation in domain 02. (e) Relationships between domain 02-averaged mid-level vertical wind (500 - 700mb) on the date with daily maximum landfall and 2-day maximum landfall in domain 02. Red filled dots represents ARs with >50% contributions from tropical moisture to domain 02 precipitation, yellow filled dots represent ARs with 25 - 50% contributions from tropical moisture to domain 02 precipitation and blue filled dots represent ARs with <25% contributions from tropical moisture to domain 02 precipitation. (f) Schematic describing how tropical moisture can be involved in AR processes.

3.4.2 Warm frontal features

In a similar way as the case in Section 3.3, tropical moisture reaching the Northwest Coast mostly contributes to ARs' moisture in mid-levels (500-750mb) following the isentropic surfaces poleward. In order to quantify the WAA strengths that are usually maximized ahead of ARs'

leading edges, we average WAA in the 10°×10° box off the Northwest Coast (red dashed box in Fig. 3-1b, 40°N - 50°N and 135°W – 125°W) within the 2-day period before the peak landfall time step occurring in domain 02. Figure 3-4c shows a positive correlation between WAA and landfall. In particular, significantly stronger WAA is associated with TME-ARs (difference of means passing the 99% confidence-level test) due to the warmer temperature accompanying tropical air. Consistently, low-level convergence averaged over domain 02 is also positively correlated with ARs' precipitation (Fig. 3-4d). However, significant stronger low-level convergence is not observed from TME-ARs (i.e., did not pass the 99% confidence-level significant test of differences in mean). This damped difference in low-level convergence, which indicates the strength of ageostrophic circulation, between TME-ARs and NTME-ARs suggests that the role of other dynamical factors in modulating AR circulation processes in the leading edge (e.g., vorticity advection in the upper-levels and possibly other feedbacks). Consequently, TME-ARs have slightly stronger vertical motion (averaged in 500 - 700mb in domain 02) than NTME-ARs in means but are not significantly different (Fig. 3-4e). It is important to note that in addition to the enhanced synoptic-scale ascent due to ageostrophic circulation, there are other finer-scale factors that can contribute to vertical motion, such as uplift induced by vapor-terrain interaction, unstable atmosphere and frontal waves (Neiman et al. 2008a; Ralph et al. 2011; Hu et al. 2017). AR-related precipitation over domain 02 is positively correlated with upward motion but no significant difference in 2-day precipitation between TME-ARs and NTME-ARs is found.

It is also interesting to note that the TME-ARs within the greatest precipitation are often associated with the greatest contributions from tropical moisture (see the upper-right corner dots in Figs. 3-4c - e showing ARs with 25 – 50% tracer contributions). This is probably due to the fact that these events induce stronger local moisture convergence as well, thus both local and

tropical moisture contribute to landfall considerably (Fig. 3-4d). In addition, although the arrival of TME-ARs increases local temperature significantly (not shown), no significant differences between the rainfall-snowfall partitioning has been found between TME-ARs and NTME-ARs, because it is also important to take the background temperature in to account, which varies along with seasonal progression (from Oct to Mar).

3.5 Conclusions

In this study, we use WRF-WVT to simulate the 29 ARs with strongest daily IVT that affected the U.S. Northwest Coast during the 1979 to 2009 period. Using this WRF-WVT tool, we are able to quantify the contribution of tropical moisture to these ARs and the processes that link tropical moisture with ARs' precipitation during landfall. From the detailed examination of one AR case in Jan 23, 1982 and the analysis of all 29 simulated cases, we depict the interactions between TME and AR features in Figure 3-4f and obtain the following conclusions:

1) There is a positive correlation between pre-cold-frontal LLJ and cold-frontal precipitation in simulated ARs, consistent with the positive feedbacks between LLJ strength, cold-frontal precipitation, diabatic heating-induced PV maxima, and resulting enhancement of the LLJ;
2) Tropical moisture can be a critical component in this cold-frontal positive feedback system by contributing to cold-frontal precipitation, which can enhance LLJ through diabatic heating induced PV maxima and increase TME;
3) ARs with stronger contribution of tropical moisture to precipitation during landfall along the Northwestern Coast (TME-ARs) are characterized by stronger pre-cold-frontal LLJ (and the associated PV induced along the cold front) in the upstream Pacific;

4) ARs with stronger contribution of tropical moisture to precipitation (TME-ARs) are associated with stronger WAA and warmer air temperature anomalies;
5) These simulated ARs show positive relationships between synoptic-scale low-level convergence, vertical motion and precipitation intensity;
6) No significant differences in ageostrophic circulation strength (measured by low-level convergence) are observed between TME-ARs and NTME-ARs, suggesting the role of other dynamical factors in modulating ARs' precipitation strength;
7) The TME-ARs with the greatest 2-day precipitation are in fact characterized by moderate contribution from the tropics (between 25% and 50%), and larger contributions from local moisture due to stronger low-level convergence;

While no clear distinctions are found in 2-day precipitation, it is evident that ARs with large contribution from tropical moisture (≥25%) are associated with stronger WAA, which can at least partially contribute to the enhanced ageostropical circulation at ARs' leading edge where in landfall occurs. TME-ARs are also associated with significantly warmer anomalies. While it is important to account for the background temperature that varies with season, it is possible for TME-ARs to have higher probability of rainfall than snowfall or even trigger snowmelt given the same background temperature. Those situations are more likely to result in extreme flooding. Therefore, it can be important to account for the contribution of tropical moisture to ARs in order to better estimate inland impacts. Our results suggest that this can be achieved by tracking the strength of pre-cold-frontal LLJ in the upstream Pacific Ocean.

By track the tropical moisture using WVT, we identified a series of processes that can be affected by tropical moisture. We believe that these processes and relationships can be used to better predict AR-related impacts. For example, our work has implications for climate change

projects because in a warmer climate, increased tropical moisture will likely be entrained into the extratropics through ARs. This can modulate pre-cold-frontal LLJ, cold-frontal elongated PV maxima, ageostrophic circulation at ARs' leading edge, and precipitation characteristics – all of which are important components to examine in order to anticipate future changes in AR-related hydrological and socio-economic impacts. However, although the current study focuses on the thermodynamic aspect of TME in ARs, it is important to understand the dynamic and thermodynamic processes of ARs in an integrated way. As an example, during El Nino years warmer SST in the eastern tropical Pacific can hold more tropical moisture, however TME is less likely to happen due to the SST-induced circulation that does not favor TME (Knippertz and Wernli 2010). Furthermore, it is clear from this study that in addition to TME, other synoptic- and meso-scale dynamical processes can enhance ageostrophic circulation or vertical motion that can ultimately lead to extreme landfall and flooding.

CHAPTER 4: A NUMERICAL WATER TRACER MODEL FOR UNDERSTANDING EVENT SCALE HYDROMETEOROLOGICAL PHENOMENA

(Published in Journal of Hydrometeorology, 2018)

We develop and implement a novel numerical water tracer model within the Noah-Multiparameterizations (WT-Noah-MP) land-surface model that is specifically designed to track individual hydrometeorological events. This approach provides a more complete representation of the physical processes beyond the standard land surface model output. Unlike isotope-enabled LSMs, WT-Noah-MP does not simulate the concentration of oxygen or hydrogen isotopes, or require isotope information to drive it. WT-Noah-MP provides stores, fluxes and transit time estimates of tagged water in the surface-subsurface system. The new tracer tool can account for the horizontal and vertical heterogeneity of tracer transport in the subsurface by allowing partial mixing in each soil layer. We compared model-estimated transit times at the H. J. Andrews Experimental Watershed in Oregon with those derived from isotope observations. Our results show that including partial mixing in the soil results in a more realistic transit time distribution than the basic well-mixed assumption. We then used WT-Noah-MP to investigate the regional response to an extreme precipitation event in the U.S. Pacific Northwest. The model differentiated the flood response due to direct precipitation from indirect thermal effects and showed that a large portion of this event water was retained in the soil after 6 months. The water tracer addition in Noah-MP can help us quantify the long-term memory in the hydrologic system that can impact seasonal hydroclimate variability through evapotranspiration and groundwater recharge.

4.1 Introduction

Land surface models (LSMs) parameterize the exchange of water, energy and momentum between the land surface and the atmosphere and are a key component in Earth system modeling. The capability of LSMs to capture the timing and extent of the soil water budget, precipitation interception, storage and eventual loss to either runoff or evaporation determines the predictive skill for droughts, floods and continental moisture recycling (Henderson-Sellers 2006).

However, in recent decades there has been a shift away from bulk quantification of the water balance to a more nuanced understanding of the physical processes and pathways of water movement by tracking water through the terrestrial system using stable isotope tracers (McDonnell 2017). The isotopic composition changes in different stores and fluxes provide a recognizable signature of water transport in the surface-subsurface continuum (Gat 1996; McGuire and McDonnell 2006). These signatures have revealed that most of the runoff from natural watersheds and/or peakflow associated with rain storms is composed of displaced pre-event water (e.g. Sklash et al. 1976; Buttle 1994; Genereux and Hooper 1998; see review by Klaus and McDonnell 2013). And more recently that the water used for plant transpiration is different from the mobile water that supplies groundwater recharge (Brooks et al. 2009; Evaristo et al. 2015), suggesting a compartmentalization in time and space of the components of the water cycle.

These isotopic observations can be used to validate and improve LSMs' representation of the water cycle. This has been done by incorporating numerically an additional isotopic module in the LSM, and then directly comparing the modeled isotopic composition to observations (Aleinov and Schmidt 2006; Fischer 2006; Yoshimura et al. 2006; Sturm et al. 2010; Risi et al. 2016). The isotope-enabled LSM simulates the concentration changes of the hydrogen and oxygen isotopes ($^{1}H^{2}H^{16}O$ and $H_2{}^{18}O$) through mixing, advection, diffusion and related isotopic fractioning (e.g.

Riley et al. 2002; Braud et al. 2005; Yoshimura et al. 2006; Fischer 2006; Aleinov and Schmidt 2006; Zhang et al. 2009; Haese et al. 2013; Risi et al. 2016). Isotopic signals reflect the accumulated transport and phase change features of the model (Yoshimura et al. 2006) and thus can probe "correctness" of model's parameterization (Henderson-Sellers 2006; McDonnell and Beven 2014). This approach is attractive because the observations and model results can be directly compared. A strength of this approach is that water isotopes from local measurements can yield relevant information to evaluate isotope-enabled LSMs at the large scale (Risi et al. 2016).

Therefore, multiple LSMs with isotope capability now exist, e.g. iso-MATSIRO, iCHASM, the GISS ILSS, ECHAM5-JSBACH-wiso, and water isotopes in ORCHIDEE and CLM. However, the use of these isotope-enabled LSMs is hampered by their isotope-data-driven nature. For offline LSM simulations, spatially gridded isotope data of precipitation and ambient vapor is required in order to drive the isotopic compositions in the land surface (Kendall and Coplen 2001). For fully coupled regional atmosphere-land simulations in which a climate model provides the atmospheric and isotopic forcing for the LSM, isotopic composition of water vapor is required as lateral boundary forcing for regional simulations. However, these isotopic observations are largely limited in time and space and are usually subject to discontinuities and discrepancies of scales between measurements and modeling, which makes it difficult to ingest in these isotopic-enabled LSMs (Twining et al. 2006; Fischer and Sturm 2006; Risi et al. 2016), particularly when simulating historical events, when isotopic observations were not readily available. On the other hand, coupled global simulations (that do not require isotope data as lateral boundary conditions) rely entirely on the modeled representation of isotope physics and dynamics in the atmospheric-ocean and land system, thus increasing the uncertainties because they are not constrained by observations (Haese et al. 2013).

It is particularly difficult to numerically track water that originates from an individual precipitation event through the surface-subsurface system using isotopes (in observations or in models). As an example, to track an individual event using observations, the isotopic composition of soil water or streamflow $\delta_{out}(t)$ is estimated via the convolution integral of the isotope compositions of a series of precipitation events $\delta_{in}(t')$ and the transit time distribution (or system response function) $g(t-t')$ that reflects the transport in the subsurface. Tracking an individual event involves the de-convolution of the isotopic signature of each event, and this requires either an a-priori assumption of a time-invariant transit time distribution (e.g. Stewart and McDonnell 1991; McGuire et al. 2002; McGuire and McDonnell 2010), or high demands on isotope data to calibrate the time-variant transit time distribution (e.g. Klaus et al. 2015). Furthermore, some mixture of isotopically fractionated water in isotope-enabled LSMs may conceal or obscure the underlying movement of event water. Therefore, uncertainties associated with the assumptions on transit time distribution (Hrachowitz et al. 2009; Birkel et al. 2011; van der Velde et al. 2012) and isotopic fractionation parameterization when phase change occurs (e.g. Yoshimura et al. 2006; Risi et al. 2016), can hinder our ability to use isotopes for tracking water for individual events.

Here we present a new numerical tool to overcome past limitations and to track water through the terrestrial system. Using numerical tracers embedded in an LSM we "tag" the water of a particular event (for example a storm, or a series of storms), and follow the water as it moves through the surface-subsurface until it ultimately leaves the system as evapotranspiration or runoff. Note that we are using numerical tracers to distinguish the event-water from the rest of water in the model, which in the real world is achieved by the different water isotopic features from precipitation input. This tool tracks the event-water rather than water isotopes; thus it directly represents the water transit features without the complexity of isotopic physics.

The overarching goal of this paper is to understand hydrometeorological event dynamics as water moves through the surface-subsurface system with multiple characteristic spatiotemporal scales. The specific goals of this paper are:

1) to present the water tracer tool within the Noah LSM with multi-parameterization options (Noah-MP) (Niu et al. 2011). Noah-MP has been widely used in climate and large-scale hydrological studies. It is the first LSM that has a numerical water tracer capability. We will refer to this tool as WT-Noah-MP.

2) to evaluate WT-Noah-MP using isotope observations from a small watershed in the Northwestern U.S.

3) to investigate the short and long-term impacts of an extreme precipitation event over a large region in the Northwestern U.S.

4.2 Model Description

4.2.1 Noah-MP

Noah-MP (Niu et al. 2011) is an advanced LSM, based on the Noah model (Ek et al. 2003) , modified to include multiple physical processes. It has been used to study the large-scale water cycle in both standalone (e.g. Yang et al. 2011; Cai et al. 2014; Pilotto et al. 2015) and coupled simulations with the Weather Research and Forecast (WRF) model (e.g. Barlage et al. 2015; Martinez and Dominguez 2016) and its extended WRF-Hydro system (Gochis et al. 2013; Senatore et al. 2015). Similar to many other LSMs, Noah-MP has a single-level canopy model, a snow model and a ground hydrology model (see water stores and fluxes in Fig. 4-1 and Table 4-1). On the other hand, Noah-MP is unique due to its flexibility to customize simulations because it provides multiple options to parameterize key processes (Barlage et al. 2015). We use the

particular parameterization set shown in Table 4-2 to illustrate the water tracer implementation. Note that no lateral flow/routing is included in this particular model setting.

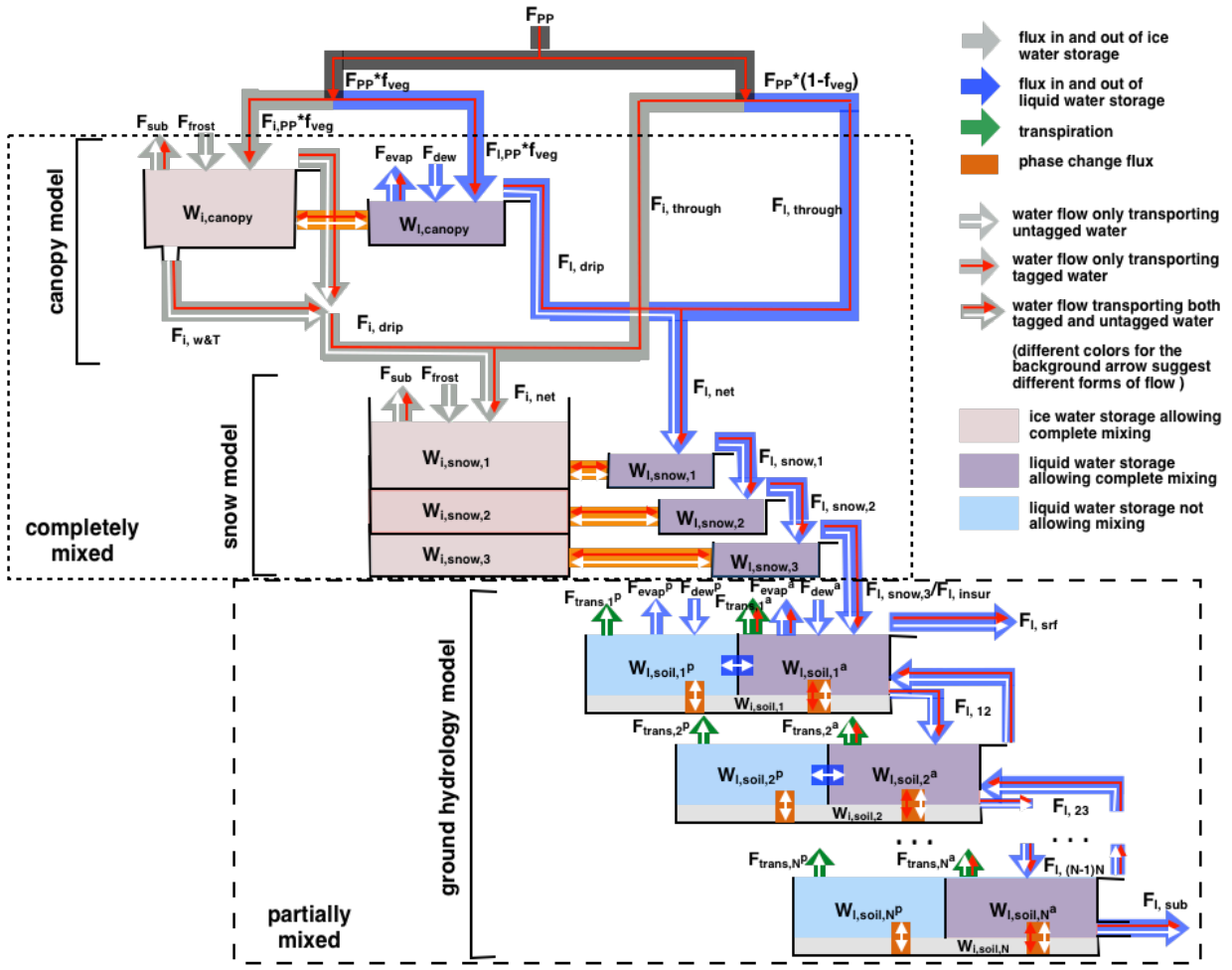

Figure 4-1. Conceptualization of the processes in WT-Noah-MP. Fluxes and storages with bluish colors suggest that in the form of liquid; fluxes and storage with the sliver color are in the form of ice. See figure legends and Table 4-1 for more information. Note that for the soil moisture reservoir that stacks liquid on top of ice does not suggests the real placement but rather it shows their shared holding capacity based on soil porosity.

Table 4-1. List of water stores and fluxes in Figure 4-1

	Variable name	Variable description
1	F_{PP}	Precipitation flux
2	F_{PP}*fveg	Precipitation flux over the fraction with vegetation coverage fveg
3	F_{PP}*(1-fveg)	Precipitaiton flux over the fraction without vegetation coverage
4	$F_{i,PP}$*fveg	Snowfall flux over the fraction with vegetation coverage fveg
5	$F_{l,PP}$*fveg	Rainfall flux over the fraction with vegetation coverage fveg
6	F_{sub}	sumlimation flux
7	F_{frost}	frost flux
8	F_{evap}	evaporation flux
9	F_{dew}	dew flux
10	$F_{i,drip}$	drip rate of canopy ice
11	$F_{l,drip}$	drip rate of canoyp liquid water
12	$F_{i,w\&T}$	exgra drip rate of canopy ice due to wind and temperature
13	$F_{i,through}$	through-fall rate of snowfall
14	$F_{l,through}$	through-fall rate of rainfall
15	$F_{i,net}$	net snowfall rate due to dripthrough and throughfall
16	$F_{l,net}$	net rainfall rate due to dripthrough and throughfall
17	$F_{l,snow,n}$	downward liquid flow from snow layer n
18	$F_{l,insur}$	input liquidwater flux to soil surface
19	$F_{l,srf}$	surface runoff rate
20	$F_{l,n(n+1)}$	liquid water fluxes between soil layer n and layer n+1
21	$F_{l,sub}$	subsurface runoff rate
22	$F_{trans,n}$	transpiration flux from soil layer n
23	$W_{i,canopy}$	canopy storage of ice
24	$W_{l,canopy}$	canopy storage of liquid water
25	$W_{i,snow,n}$	ice storage in snow layer n
26	$W_{l,snow,n}$	liquid water storage in snow layer n
27	$W_{i,soil,n}$	ice storage in soil layer n
28	$W_{l,soil,n}$	liquid water storage in soil layer n

Table 4-2. Option set for physical processes used in Noah-MP

	Physical processes	Options
1	dynamic vegetation	4 (use table LAI; use maixmum vegetation fraction)
2	canopy stomatal resistance	1 (Ball-Berry)
3	soil moisture factor for stomatal resistance	1 (Noah)
4	runoff and groundwater	3 (free drainage)
5	surface layer drag coefficient	1 (Monin-Obukhov)
6	supercooled liquid water	1 (no iteration)
7	frozen soil permeability	1 (linear effects)
8	radiation transfer	3 (two-stream applied to vegetated fraction)
9	ground snow surface albedo	2 (CLASS)
10	partitioning precipitation into rainfall and	1 (Jordan)
11	lower boundary condition of soil temperature	2 (original Noah)
12	snow/soil temperature time scheme	1 (semi-implicit)
13	surface resistance to evaporation/sublimation	1 (Sakaguchi and Zeng, 2009)

4.2.2 Water tracer implementation in Noah-MP

The water tracer module is a new set of equations that describe the dynamics of the partial storages and fluxes of the water tracers. The water tracers "tag" event precipitation and leave the system through evapotranspiration and runoff. Figure 4-1 shows how the tracers are conceptualized in each component of Noah-MP.

Tracer initiation: We initiate the water molecules from precipitation within a designated time window as water tracers. Before this time window, the tracer module is not activated and the simulation is the same as the original Noah-MP. During the designated period, the precipitation is "tagged" and provides the input of tracers using Equation (4-1). Therefore, the total tracer input equals the event precipitation designated by the time window. After this event, no further precipitation is being "tagged" but the existing tracers continue to be tracked until the end of simulation.

$$F_{PP}{}' = F_{PP} \times wt_{ratio},\ wt_{ratio} = \begin{cases} 1, & \text{if timestep is within tagging period;} \\ 0, & \text{if timestep is before/after tagging period.} \end{cases} \quad (4\text{-}1)$$

where F_{PP}' is the tracer input from precipitation, F_{PP} is the total precipitation into the land surface, and wt_{ratio} is a ratio used to control tracer input.

Tracers in single-layer canopy model: The canopy model characterizes the fraction covered by vegetation f_{veg} in each model grid. The canopy can store water if intercepted by vegetation leafs and stems (Fig. 4-1, top), and the model allows canopy storages in both liquid water and ice phases. Forest canopies are capable of intercepting large quantities of precipitation, which account for 10-50% of seasonal-long or annual precipitation (Carlyle-Moses and Gash 2011).

The intercepted water from prior rain events is found to have important mixing effects with the current rainfall in generating throughfall (Allen et al. 2013). To account for the mixing between pre-event canopy storage and the water tracers, we assume a "well-mixed" canopy model as in other isotope-enabled LSMs (e.g. Fischer 2006; Yoshimura et al. 2006; Aleinov and Schmidt 2006) (Fig. 4-1). Over the grid area covered by vegetation (f_{veg}), the water tracers are immediately mixed with pre-event canopy storage with a mixing ratio of $R_{l,canopy}$ or $R_{i,canopy}$:

$$R_{l,canopy} = \frac{F_{l,PP}'\ f_{veg}\ \delta t + W_{l,canopy}^{0}\ R_{l,canopy}^{0}}{W_{l.canopy}}\ ;\ R_{i,canopy} = \frac{F_{i,PP}'\ f_{veg}\ \delta t + W_{i,canopy}^{0}\ R_{i,canopy}^{0}}{W_{i,canopy}} \quad (4\text{-}2)$$

where $F_{l,PP}'$ and $F_{i,PP}'$ are tracer fluxes in the form of rain and snow respectively, δt is the interval of model timestep, $W_{l,canopy}^{0}$ and $W_{i,canopy}^{0}$ are total liquid water and ice storages from the previous timestep, $R_{l,canopy}^{0}$ and $R_{i,canopy}^{0}$ are tracer mixing ratios for the liquid water and ice storages from the previous timestep. Then, the tracer fluxes, such as evaporation, sublimation, drip-through and phase changes are all partitioned in proportion to $R_{l,canopy}$ or $R_{i,canopy}$:

$$\begin{cases} F_l' = F_l \times R_{l,canopy}, \text{ if the flux is extracting water from the liquid water storage;} \\ F_i' = F_i \times R_{i,canopy}, \text{ if the flux is extracing water from the ice water storage.} \end{cases} \quad (4\text{-}3)$$

where F_l' and F_l are the tracer and total fluxes from the liquid water storage ($W_{l,canopy}$) through different processes while F_i' and F_i are the tracer and total fluxes from the ice water storage ($W_{i,canopy}$). Note that we do not account for dew/frost, which is from the ambient water vapor, as a source for the water tracers to ensure that the only source for tracers is the "tagged" precipitation event.

Tracers in the snow model: Noah-MP uses a physically based snow model to simulate snowpack dynamics. The model has up to three layers (three individual stores) depending on the snowpack depth (Fig. 4-1, middle). The "well-mixed" assumption is assumed in each snow layer (e.g. Fischer 2006; Yoshimura et al. 2006; Aleinov and Schmidt 2006). The tracer input as rainfall/snow increases the storage of the topmost snow layer, following the original Noah-MP. The fluxes contributing to sublimation, phase change and snow layer dividing/combining are derived using similar equations to (4-2) and (4-3). In particular, when the downward percolation occurs ($F_{l,snow,n}$) due to rain-on-snow or snowmelt, the tracer flux ($F_{l,snow,n}'$) is calculated using (4-4):

$$R_{l,snow,n} = \frac{F_{l,snow,n-1}\ R_{l,snow,n-1}\ \delta t + W^0_{l,snow,n}\ R^0_{l,snow,n}}{F_{l,snow,n-1}\ \delta t + W^0_{l,snow,n}};$$
$$F_{l,snow,n}{}' = F_{l,snow,n} \times R_{l,snow,n} \qquad (4\text{-}4)$$

where $F_{l,snow,n-1}$ and $R_{l,snow,n-1}$ are the total liquid flow and tracer mixing ratio from the layer above, $W^0_{l,snow,n}$ and $R^0_{l,snow,n}$ are the total liquid storage and tracer mixing ratio of layer n at the prior timestep and $R_{l,snow,n}$ is the mixing ratio of tracers in liquid storage of layer n. Therefore, we assume that the meltwater flux is spatially uniform and homogeneously mixed as it percolates through the snowpack (Judy et al. 1970; Stichler 1987; Raben and Theakstone 1998). However, we are not

accounting for meltwater percolation down preferential pathways or discrete "fingers" (e.g. Gerdel:1954kd; Marsh and Woo 2010), accounting for this process requires a more sophisticated snow model to represent the heterogeneity of the melting process (e.g. Feng et al. 2002; Lee et al. 2010).

Tracers in the ground hydrologic model: In this study, we use a simple combination of infiltration-excess-based surface runoff scheme and a gravitational free-drainage subsurface runoff scheme as used in the original Noah (Schaake et al. 1996). Note that Noah-MP provides more sophisticated runoff and groundwater schemes to account for soil-ground water interactions; the tracers could be extended to these schemes in the future. At the soil surface, the total water input ($F_{l,insur}$) can generate infiltration-excess surface runoff ($F_{l,srf}$), which is partitioned into the tracer contribution ($F_{l,srf}'$) using (4-5):

$$R_{l,insur} = \frac{F_{l,insur}'}{F_{l,insur}}; \qquad F_{l,srf}' = F_{l,srf} \times R_{l,insur} \tag{4-5}$$

where $R_{l,insur}$ is the mixing ratio of tracer input at the soil surface to total input, and $F_{l,insur}'$ and $F_{l,insur}$ are the tracer and total water input at the soil surface. The rest is infiltrated into the soil column. The critical issue is the partitioning of subsurface fluxes into tracer fluxes within the soil column.

In Noah-MP, the liquid water in each soil layer is updated using Richards Equation:

$$\frac{\partial \theta}{\partial t} = \frac{\partial}{\partial z}\left[D(\theta)\frac{\partial \theta}{\partial z}\right] + \frac{\partial K(\theta)}{\partial z} \tag{4-6}$$

where θ is the soil water content which can be converted to water storage $W_{l,soil,n}$ multiplied by the soil thickness δz, $K(\theta)$ is the hydraulic conductivity and $D(\theta)$ is the soil water diffusivity.

$K(\theta)$ ($D(\theta)$) is parameterized as a function of θ and saturated hydraulic conductivity K_{sat} (saturated diffusivity D_{sat}). In Noah-MP, K_{sat} and D_{sat} are assigned according to soil type neglecting the vertical variations. In our simulations, we use observed profiles of these parameters from field experiments for the small watershed in the Northwestern U.S. (Section 4.4.1) to account for the compaction with soil depth. However, we use the assigned parameters without vertical variation for the regional-scale simulation (Section 4.4.2) as in the default Noah-MP due to the lack of observations. For all soil layers, the equations in the form of Equation (4-6) are solved together through a tridiagonal matrix using a time-implicit scheme (Niu et al. 2011).

Tracing water through the soil column is perhaps the most problematic aspect of the tracer model. The difficulty in implementing tracers using Richard's equation is that Equation (4-6) is not valid for tracer soil water (we can't replace θ with θ'). The reason is that the tracer water moves in proportion to the gradient in total moisture content, not the gradient in tracer moisture content. For this reason, we first calculate the total flux (the final form of which was not explicitly calculated in the original Noah-MP due to the time-implicit scheme), then partition the flux by multiplying by the mixing ratio tracer soil water to total soil water. In the discussion that follows we are assuming a "well-mixed" reservoir within each layer (in Section 4.2.3 we describe how to account for incomplete mixing). The water budget equations for total and tracer soil moisture are described in Eq. (4-7) and (4-8):

$$\begin{cases} \dfrac{\theta_1-\theta_1^0}{\delta t}=\dfrac{\left(F_{l,insur}-F_{l,srf}\right)-F_{l,12}-F_{evap}-F_{trans,1}}{\delta z_1}, & \text{for soil layer 1;} \\ \dfrac{\theta_n-\theta_n^0}{\delta t}=\dfrac{F_{l,(n-1)n}-F_{l,n(n+1)}-F_{trans,n}}{\delta z_n}, & \text{for soil layer 1<n<N;} \\ \dfrac{\theta_N-\theta_N^0}{\delta t}=\dfrac{F_{l,(N-1)N}-F_{l,sub}-F_{trans,N}}{\delta z_N}, & \text{for soil laye N.} \end{cases} \quad (4\text{-}7)$$

$$
\begin{cases}
\dfrac{R_1\theta_1 - R_1^0\theta_1^0}{\delta t} = \dfrac{\left(F_{l,insur}{}' - F_{l,srf}{}'\right) - R_1 \max\left(F_{l,12},0\right) - R_2 \min\left(F_{l,12},0\right)}{\delta z_1} \\
\qquad\qquad + \dfrac{-R_1 F_{evap} - R_1 F_{trans,1}}{\delta z_1}, \qquad \text{for soil layer 1;} \\
\dfrac{R_n\theta_n - R_n^0\theta_n^0}{\delta t} = \dfrac{R_{n-1} \max\left(F_{l,(n-1)n},0\right) + R_n \min\left(F_{l,(n-1)n},0\right) - R_n \max\left(F_{l,n(n+1)},0\right)}{\delta z_n} \\
\qquad\qquad + \dfrac{-R_n \min\left(F_{l,n(n+1)},0\right) - R_n F_{trans,n}}{\delta z_n}, \text{ for soil layer 1<n<N;} \\
\dfrac{R_N\theta_N - R_N^0\theta_N^0}{\delta t} = \dfrac{R_{N-1} \max\left(F_{l,(N-1)N},0\right) + R_N \min\left(F_{l,(N-1)N},0\right)}{\delta z_N} \\
\qquad\qquad + \dfrac{-R_N F_{l,sub} - R_N F_{trans,N}}{\delta z_N}, \qquad \text{for the bottom soil layer N.}
\end{cases}
\tag{4-8}
$$

where θ_n and θ_n^0 are the total soil water contents of layer n at the current time step and the prior time step, $F_{l,(n-1)n}$ is the total flux between layer (n-1) and n (taking downward direction as positive), R_n and R_n^0 are the mixing ratios of tracer soil water to total soil water in layer n at the current and the prior time steps respectively. To solve for R_1 - R_N, we first calculate the interlayer fluxes $F_{l,(n-1)n}$ using (4-7), and subsequently calculate the only unknowns R_1 - R_N in (4-8). Finally, the tracer fluxes and storages of each layer can be obtained assuming proportional extractions using R_1 - R_N.

4.2.3 Partial mixing in soil

The assumption of complete mixing of tracers with existing soil water is likely inadequate (Godsey et al. 2009; Rouxel et al. 2010; Hrachowitz et al. 2016). The tracer response can be very different from the bulk-flux response (e.g. derived from the Richards Equation or streamflow from an outlet) that largely manifests the effect of hydraulic gradients (i.e. the difference between

velocity and celerity) (see more details in McDonnell and Beven 2014; Hrachowitz et al. 2016). Water can bypass the soil matrix through macropores and reach specific depths faster than water moving through soil micropores (Ranken 1974; McDonnell 1990; Leaney et al. 1993; Kendall and McDonnell 1998; Buttle and McDonald 2002). To account for the dual response timescales, studies have conceptualized the flow through preferential pathways and soil matrix by separating the total storage into "active/mobile" and "passive/immobile" storage compartments in modeling (e.g. Fenicia et al. 2010; Hrachowitz et al. 2013). Under relatively dry conditions, a high portion of incoming precipitation (water tracers in our case) can be transiently stored in the porous flow media and interact with resident water of varying age; as the system wets up, more water is likely to bypass the matrix through preferential flowpaths due to higher hydrologic connectivity (Hrachowitz et al. 2013; 2016). This separation of active and passive storages is broadly consistent with the ecohydrological separation found by isotopic studies suggesting different storages that supply plant transpiration (passive/immobile) and groundwater recharge and streamflow (active/mobile) (Brooks et al. 2009; Evaristo et al. 2015).

However, the parameterization of such a dynamical partial mixing usually introduces extra parameters that require calibration (e.g. McGuire et al. 2007; Hrachowitz et al. 2013; Evaristo et al. 2015). To represent the effect of partial mixing, yet keep the simplicity of model application, we simplify the above process by (1) separating the total storage in each soil layer into half "mobile" and half "immobile" components (See the different stores of water in Fig. 4-1); (2) assuming the input tracer flux only passes the "mobile" storage (Fig. 4-1, bottom); (3) updating the two storages – "mobile" and "immobile" – with the total storage of each layer (half "mobile" and half "immobile") while neglecting tracer exchange between the two half storages (i.e. updating of the "immobile" half storage is achieved through non-tracer water exchanges). Therefore, we are

assuming that the incoming tracer flux only mixes with half of the storage that is "active/mobile", while the other half can be conceptualized as the water retained in soil matrix and is assumed to be "passive/immobile". These simplifications are more applicable for wet conditions, which are characterized by a faster transfer of younger water bypassing the soil matrix. While simplistic, this allows us to investigate the tracer responses to different "mixing" assumptions without introducing additional parameters. In future applications, the fraction of the storage that is "mobile" or "immobile" can be changed according to the research question and specific conditions of the region.

In addition to partitioning into "mobile" and "immobile", we also increased the number of soil sublayers in the tracer parameterization. The original soil layer thickness (up to 1 m in the default Noah-MP and up to 0.4 m in our case) may be too thick to resolve the vertical profile of tracers, especially for relatively short model time steps (30 min - 1 hour in this study). Such a homogeneous mixing will likely result in an earlier arrival of the tracer to a certain depth but with more dispersed transit time distribution than in observations (see results in Section 4.3). To account for vertical heterogeneity of tracer movement, we increase the number of layers in the soil when dealing with the tracers (not the bulk flow). We assume mixing within ½ and ¼ depth of each original soil layer (from Fig. 4-2b to Figs. 4-2c and 4-2d). To obtain the tracer flux and storage in each sublayer, we use the same equations as (8) to solve for the mixing ratios in each sublayer. Using sublayers, the transpiration flux $F_{trans,n}$ becomes ½ or ¼ of $F_{trans,n}$ in each sublayer and the interlayer fluxes become those between sublayers (red arrows in Fig. 4-2c). These sublayer fluxes are obtained from linear interpolation of the bounded whole-layer fluxes (e.g. $F_{I,12}$ and $F_{I,23}$ in Fig. 4-2a). In this way, we are able to preserve the flux gradient ($\partial Flux / \partial z$) of the thicker original layer throughout the sublayers and maintain the vertical profile of soil moisture invariant.

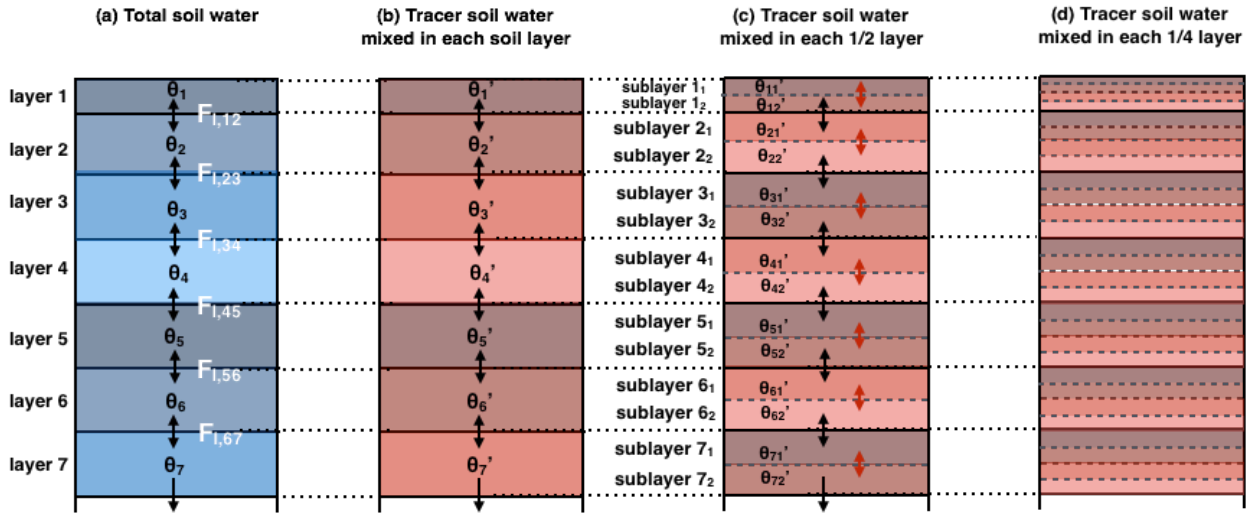

Figure 4-2. Schematics of (a) the soil layer configuration in Noah-MP, (b) the mixing of tracers in each soil layer as Noah-MP, (c) the mixing of tracers in each 1/2 layer, and (d) the mixing of tracers in each 1/4 layer.

In summary, we account for the horizontal and vertical heterogeneity of tracer transport in the subsurface by allowing partial mixing in each soil layer by (1) accounting for "mobile" and "immobile" storage, where the tracers only interact with the "mobile" storage; and by (2) subdividing the original model layers into additional sublayers when quantifying tracer movement. We test these different assumptions and their impact on the tracer flow and transport over a 10 ha watershed in Western Oregon U.S. (WS10). Like the "virtual experiment" approach introduced by Weiler and McDonnell (2004), over WS10 we collectively combine the numerical experiments using WT-Noah-MP using different mixing assumptions and the field experiments for the purposes of exploring first-order controls on transit time distribution of a controlled watershed. In addition, we demonstrate the use of WT-Noah-MP over a large region in U.S. Pacific Northwest (Western Washington) as an exploratory tool to quantify short and long-term impacts of an extreme precipitation event, with these partial-mixing assumptions incorporated as a measure of uncertainty.

4.3 Study Sites and Model Configuration

4.3.1 WS10 Watershed

WS10 (10.2 ha) is located in the H. J. Andrews Experiment Forest, as part of a larger research effort of the Long-Term Ecological Research (LTER) program in the west-central Cascade Mountains of Oregon, USA (44.2°N, 122.25°W) (McGuire et al. 2007). WS10 (Fig. 4-3a) is equipped with a comprehensive network of instrumentation and has been intensively studied for forest ecological and hydrological research (e.g. Jones 2000; McGuire and McDonnell 2010; Klaus et al. 2015).

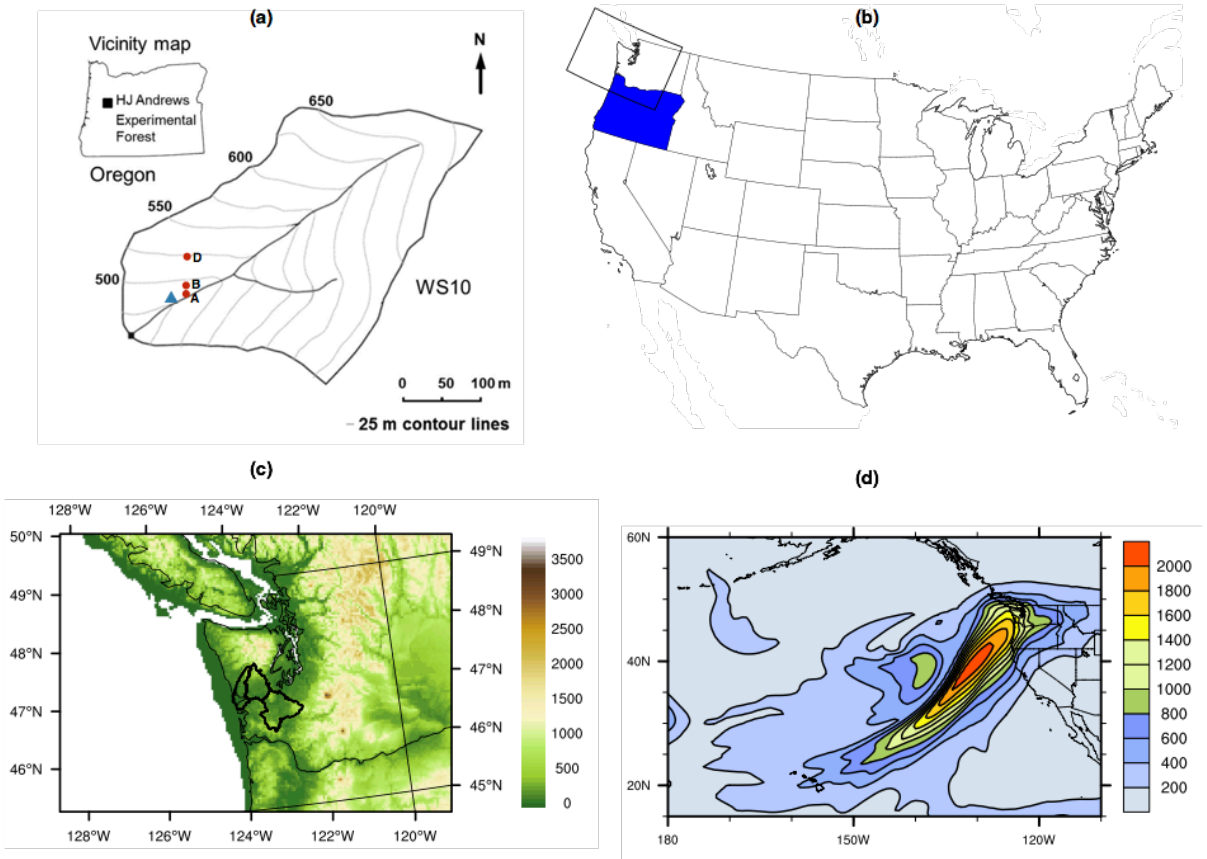

Figure 4-3. (a) Map of WS10 of the H.J. Andrews Experimental Forest and the location within Oregon, USA (from Klaus et al. 2015). The blue triangle suggests the location with soil moisture probes. The red dots suggest the locations of lysimeters that collects isotope measurements. (b) Map of the United States with the Oregon state highlighted with blue within which WS10 is located and the domain for Western Washington highlighted with the black box. (c) Topographic feature (unit: m) of the domain of Western Washington with the Chehalis River basin delineated in black. (d) Well-defined AR signature at 12Z Dec 3, 2007 shown by the narrow structure of vertically integrated vapor transport (unit: kg/m/s), which has significantly impacted the Chehalis River basin.

The vegetation type is a naturally regenerated second growth Douglas fir forest after a 1975 clear-cut harvest. The catchment is steep with slopes ranging from 30 to over 45° and elevations from 473 m to 680 m. It contains residual and colluvial clay loam soils with an average soil depth of 1.3 m. Surface soils are well aggregated, but lower depths (70 – 100 cm) have more massive blocky structure with less aggregation. Beneath is partially weathered bedrock with poor permeability in thickness from 1 to 7 m (~3.7 m on average). Annual precipitation is 2200 m (1979-2008), about 80% of which falls between October and April. Consequently, the catchment gradually wets-up from October to December and maintains the wet conditions until late spring. Runoff generation in the catchment shows clear thresholds, hysteresis, and event transit times varying with antecedent conditions. More details about WS10 can be found in McGuire et al. (2007), McGuire and McDonnell (2010), Klaus et al. (2015) and Hale and McDonnell (2016).

In a field experiment carried out in the 2002–2003 winter rainy season, oxygen-18 (^{18}O) samples were collected weekly for bulk precipitation and at time intervals between daily and weekly for soil water from the lysimeters (Fig. 4-3a). McGuire and McDonnell (2010), hereafter MM2010, used the data collected and a lumped parameter convolution model (Stewart and McDonnell 1991; McGuire et al. 2002; 2005) to examine the transit time of soil water along depth (red dots in Fig. 4-3a). To compare isotope observations to the numerical tracer model, we use a measure of "transit time" derived from the numerical tracers.

4.3.2 Western Washington State

Located to the north of WS10, the regional simulation we conduct covers the western part of Washington state (Figs. 4-3b and c). This mountainous domain covers Cascade Mountains on the east and Olympic Mountains close to the coastline. Surrounded by these mountains, the Chehalis River basin (delineated by black in Fig. 4-3c) is flood-prone for storms over the mountains. Similar

to WS10 in Oregon, western Washington is also frequently affected by winter storms. In particular, most of its winter precipitation (>60%) can be attributed to atmospheric river (AR) events (Rutz et al. 2014). ARs are structures of intense water vapor transport in the atmosphere, most of which is converted into precipitation over the U.S. West Coast (see more details in Zhu and Newell 1998; Neiman et al. 2008a; Ralph and Dettinger 2012). During 1-3 December 2007, an exceptionally intense AR event with well-defined filamentary structure of vapor transport (Fig. 4-3d) severely impacted the Chehalis basin (see more details in Hayes 2008).

4.3.3 Noah-MP configurations and forcing data

Watershed-scale Simulation, WS10: Noah-MP is configured with 7 soil layers (0.1, 0.3, 0.3, 0.3, 0.3, 0.3, 0.4 m in thickness for each layer from top to bottom) with a total soil depth of 2.0 m. The soil type is prescribed as clay loam, and the vegetation type as evergreen needleleaf forest. Noah-MP is run offline and uses the North American Land Data Assimilation System (NLDAS) (Mitchell 2004) data (1/8° grid and hourly resolution) as forcing data, which includes precipitation, downward shortwave and longwave radiation, near-surface air temperature, wind and humidity, and surface pressure. We run the single-column simulation using data from the grid point in NLDAS that is closest to the location of WS10 (44.25°N, 122.25°W), with initial soil conditions provided by Noah LSM simulations from NLDAS. The simulation period is from Jan 1st, 1999 to Dec 31st, 2004 with a model time step of 30 minutes, thus it encompasses the time period of the field tracer experiment in MM2010. We use the parameterizations shown in Table 4-2.

In contrast with the default version of Noah-MP, we also incorporate the vertical variations in soil properties according to observed profiles from field observation. McGuire et al. (2007) fitted exponential functions to observations to represent vertical profiles for saturated hydraulic conductivity (K_{sat}) and drainable porosity (n_d) in the form of:

$$K_{sat}(z) = k_0 \exp(-z/f) \tag{4-9}$$

$$n_d = n_0 \exp(-z/d) \tag{4-10}$$

where k_0=8.7 (unit: m/h), f=0.56 and n_0=0.26, d=1.12. We use these two functions to replace the two components for computing hydraulic conductivity $K(z)$ in Noah-MP as (4-11) by (4-12):

$$K(z) = K_{sat}\left(\frac{\theta(z)}{\theta_{\max}}\right)^{2b+3} \tag{4-11}$$

$$K(z) = K_{sat}(z)\left(\frac{\theta(z)-\theta_r(z)}{\theta_{\max}-\theta_r(z)}\right)^{2b+3} \tag{4-12}$$

where $\theta_{\max}$ is the soil porosity and $\theta_r(z)$ is assumed to be soil moisture retained after draining with 100 cm of tension ($\theta_r(z) = \theta_{\max} - n_d(z)$). By doing this, we improve the representation of both K_{sat} and effective saturation $\left(\frac{\theta(z)-\theta_r(z)}{\theta_{\max}-\theta_r(z)}\right)$. The same replacement for effective saturation is also used to compute hydraulic diffusivity $D(z)$. The sensitivity of the b parameter in (4-12) is tested around its mean within a standard deviation (8.52±3.44; data from Clapp and Hornberger 1978).

Regional-scale Simulation, Western Washington: We perform the simulation over the spatial domain shown in Figure 4-3c. It has 3 km grid-spacing with prescribed soil, vegetation, and topographic parameters derived from 30-arcsecond resolution geographical dataset (http://www2.mmm.ucar.edu/wrf/users/download/get_sources_wps_geog.html). We use the same soil layer configuration as in WS10. The simulation is forced by the Global Land Data Assimilation

System (GLDAS; 1/4° spatial resolution and hourly temporal resolution) (Rodell et al. 2004) and initialized by state variables from the Noah LSM simulation in GLDAS. Note that NLDAS is not used because artificial contrasts of precipitation forcing are found at the US-Canada border, which is probably due to deficiencies in the data assimilation algorithm (not shown). The same set of parameterizations shown in Table 4-2 is used. We run the simulation for the period from July 1st, 2007 to June 30th, 2008, with a model timestep interval of 1 hour. Note that no observation-based vertical profiles of soil properties are incorporated in this regional-scale simulation.

4.3.4 Experiments using WT-Noah-MP

Mixing experiments: To test the different assumptions of subsurface mixing, we implement 4 types of numerical experiments using WT-Noah-MP:

(1)CM: complete mixing scenario in each soil layer;

(2)PM: partial mixing scenario with half "active/mobile" storage;

(3)CM-1/2 and CM-1/4: complete mixing scenario with mixing in every ½ and ¼ thickness of soil layer;

(4)PM-1/2 and PM-1/4: partially mixed scenario in every ½ and ¼ thickness of soil layer.

For WS10, we use the WT-Noah-MP tool to "tag" 11 individual precipitation events (storms 5 to 15 in MM2010). These events are chosen because they occurred after the wet-up phase, thus we could focus on wet conditions. The time windows used to "tag" each storm are shown in Table 4-3 with a 3-day duration of each event. In total, we run 11 simulations with the same configuration but with different storm events "tagged" using Equation (4-1).

For the spatial simulation of Western Washington, we "tag" this extreme AR event in December 2007. We specify the precipitation falling from 00Z December 1, 2007 to 00Z December 10, 2007 as tagged water.

Table 4-3. The tagged time periods for 11 precipitation events.

	Start of tagging	End of tagging
1	2002-11-16:0000	2002-11-19:0000
2	2002-12-09:0000	2002-12-12:0000
3	2002-12-12:0000	2002-12-15:0000
4	2002-12-20:0000	2002-12-23:0000
5	2002-12-29:0000	2003-01-01:0000
6	2003-01-02:0000	2003-01-05:0000
7	2003-01-11:0000	2003-01-14:0000
8	2003-01-21:0000	2003-01-24:0000
9	2003-01-24:0000	2003-01-27:0000
10	2003-01-29:0000	2003-02-01:0000
11	2003-02-15:0000	2003-02-18:0000

4.4 Results and Discussion

4.4.1 Watershed-scale simulation of WS10 (Oregon)

In this section, we apply the WT-Noah-MP model to WS10 to explore the dominant process controls on water transit time. Specifically, we conduct a series of "virtual experiments", characterized by different hypotheses of subsurface mixing. We compare our numerical results to the results from observational field tracer experiments with the goal of evaluating the WT-Noah-MP tool. Figure 4-4a shows the measured soil moisture at a location 15 m from the slope base (blue triangle in Fig. 4-3a) and Figure 4-5a shows the best-fit transit time distributions using observed $\delta^{18}O$.

Soil moisture simulation: Before evaluating the tracer dynamics, we evaluate the simulation of the total soil moisture from Noah-MP. Figures 4-4b and c show the soil moisture at three different levels (~30 cm, 70 cm and 100 cm) from Sep 1st, 2002 to April 1st, 2003 (with b=5.08 in Equation 12). Consistent with observations from MM2010 (Fig. 4-4a), simulated soil moisture

(Figs. 4-4b) shows a wetting-up period on ~Nov 10th, 2002, marking the beginning of the winter rainy season. In addition, the observed delay in wetting with depth is also represented in Noah-MP. After the wetting-up period (after Dec 10th, 2002), the transient fluctuations in soil moisture as responses to precipitation events in Noah-MP are very similar to those from observations and the simulated soil moisture captures the increasing trend with depth as observed. However, the Noah-MP simulations underestimates the vertical gradients in soil moisture with means increasing from 24.6% at 30cm to 33.2% at 70cm to 43.5% at 100cm (averaged over the period shown in Fig. 4-4a), while the simulated means are 35.1% at 25cm, 37.3% at 70cm and 38.3% at 100cm (Fig. 4-

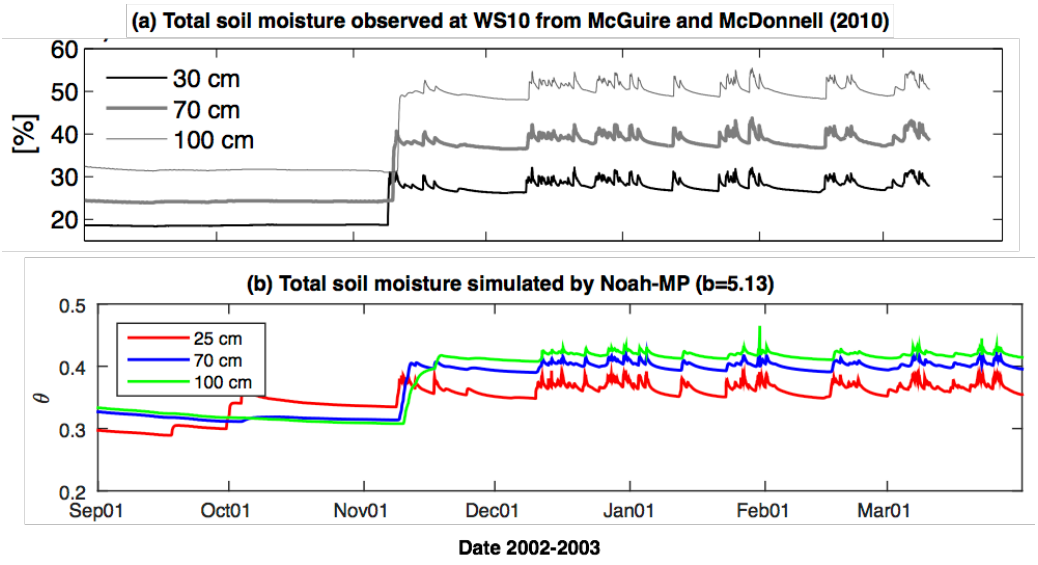

Figure 4-4. Time series of the volumetric water content (θ) (a) at location suggested by the blue triangle in Fig. 4-3a (adapted from McGuire and McDonnell 2010) and (b) from the single-column simulation from Noah-MP with b=5.08.

4b).

The simulation of vertical gradients in soil moisture improves with decreasing b parameter in Equation (4-12). Figure 4-4b shows the simulation with b=5.08 with a better representation than b=8.52 (not shown) because a smaller b requires larger soil moisture gradients to maintain the quasi-equilibrium soil moisture in wet conditions. This suggests that the model over-represents the

nonlinearity between soil moisture and $K(z)$ with large b values. In addition, the model also underestimates the 100 cm soil moisture in the wet period (after mid-December) when the observed soil moisture was near saturated. This can be attributed to the simplified model physics in Noah-MP that allows free drainage from the soil bottom (with the current configuration) with no lateral flow represented, while the near-saturated soil moisture in Figure 4-4a is measured at a location close to slope base (Fig. 4-3a) as a result of low permeability of the bedrock and especially of upstream lateral flow. Differences also exit in precipitation forcing from gauge measurements and NLDAS representing a 1/8° grid. Note that tracer transit is a function of flux, storage and mixing, we believe that Noah-MP reasonably captures the dynamics of soil moisture that allows us to estimate subsurface transit features.

CM scenario: We now test the hypotheses of tracer mixing in WT-Noah-MP using transit time distribution. We do this first for the CM scenario with complete mixing in each of the original 7 soil layers. For each "tagged" event, we obtain the transit time distribution using Equation (4-9) (Zuber 1986; McGuire et al. 2007):

$$TTD(t) = \frac{C_I(t)}{\int_0^\infty C_I(t)dt} = C_I(t)Q(t)/M \tag{4-13}$$

where $TTD(t)$ is the transit time distribution from the model, $C_I(t)$ is the tracer output concentration, $Q(t)$ is the output flux and M is sum of tracer mass applied to the system, which is the water mass of the "tagged" precipitation event in our case. Using this equation, we obtain the transit time distribution at 25, 70 and 100 cm depths of each event. Figure 4-5b (red dashed curve) shows the result from WT-Noah-MP. (Note that all the simulations are run with b=5.08.) The model results show more lagged and dispersed tracer responses as the tracers infiltrate down the soil column (from the soil surface to deeper soils). Comparing with observations from

MM2010 with particular focus on site D (black curves in Fig. 4-5a), which is the most upstream site (see

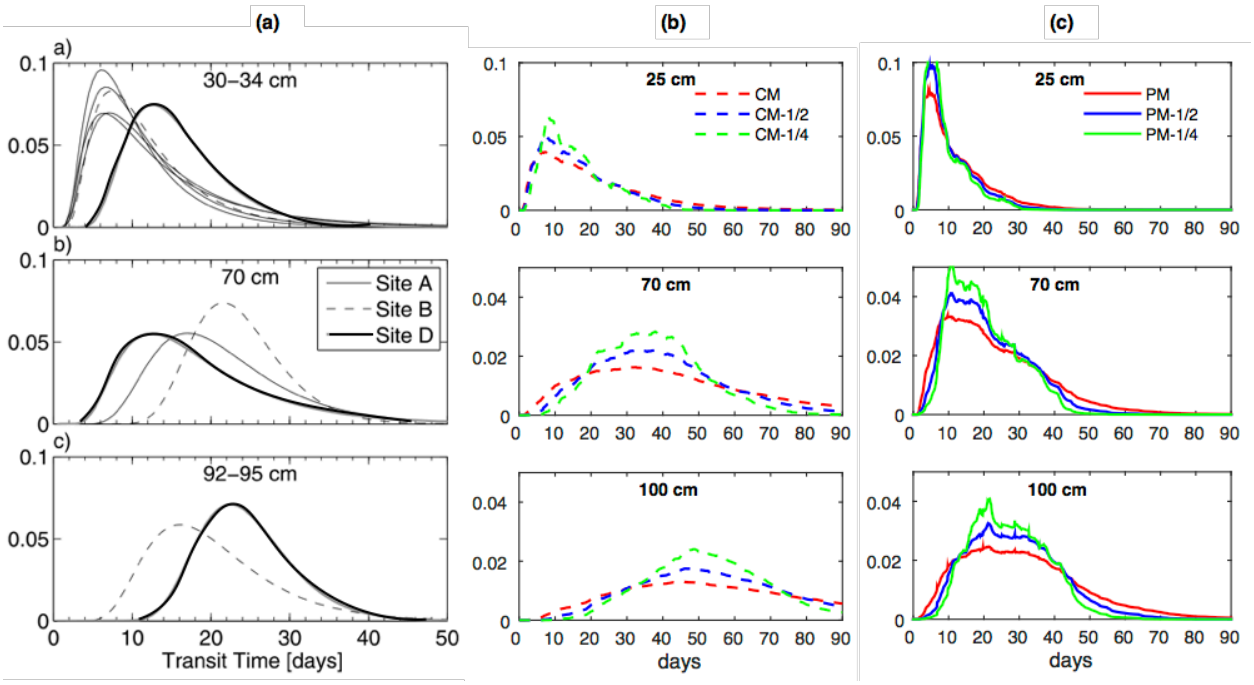

Figure 4-5. Soil water transit time distributions for sites A, B and D (red dots in Fig. 4-3a) (a; adapted from McGuire and McDonnell 2010) and estimated from WT-Noah-MP with CM, CM-1/2 and CM-1/4 scenarios (b) and with PM, PM-1/2 and PM-1/4 scenarios (c).

location in Fig. 4-3a) and less likely subject to lateral flow, the modeled mean transit times at 70 cm (38 days) and 100 cm (55 days) are much longer than the observed ones (~22 days). And the modeled transit time distributions at all levels are more dispersed than observations. Moreover, the time lag of ~10 days before the rising limb seen at 92-95 cm level is not reproduced in the model. Therefore, the modeled transit times with CM show more dispersed distribution, longer mean transit time at deeper layers with no time lag of wet-front penetration. These could be an artifact of the complete mixing assumption, which results in too much tracer being retained in the unsaturated soil (McGuire et al. 2007).

PM scenario: Now, we accelerate the water transit through preferential flow paths by assuming half of the soil water storage to be "active/mobile" while the other half retained in the

soil matrix (see Fig. 4-1). Figure 4-5c (red solid curve) shows the modeled transit time distributions of soil water at 25, 70 and 100 cm. Compared with Figure 4-5b, the distributions from the PM scenario are more highly peaked with less dispersion. The mean transit times estimated from Figure 4-5c (red solid curves) are 10, 22 and 28 days for the three levels, which are very close to the ones estimated from isotope observations (Fig. 4-5a). The faster transit of tracers can also be seen in Figure 4-6, that shows a faster downward propagation of the tracer flow (comparing the red dashed and solid profiles). The better results from the PM-active scenario suggest that the preferential flow pathways are critical for event water transit at WS10, especially for these events after the soil wet-up. However, the observed time lag in the rising limb of the hydrograph of tracer response at ~100 cm is still not captured.

CM-1/2 and CM-1/4 scenarios: To better represent the vertical profiles of tracers we assume mixing in every ½ and ¼ of the original soil thickness for each layer. Figure 4-5b show the modeled transit time distributions from this assumption (dashed blue and green curves). By allowing mixing in a thinner layer, we see more narrow-peaked distributions. Unlike that in PM scenario, the mean transit times are not significantly changed but there is a clear lag of the rising limb in tracer response at 100 cm. This lag is explained by a less dispersed downward penetration shown in Figure 4-6 (compare the dashed red, blue and green profiles). Thus, tracers simulated with CM-1/2 and CM-1/4 penetrate in a more concentrated way into deeper layers, mimicking piston flow. This enables these scenarios to capture the lag of tracer response in deeper layers, which is not captured by the CM or PM simulations.

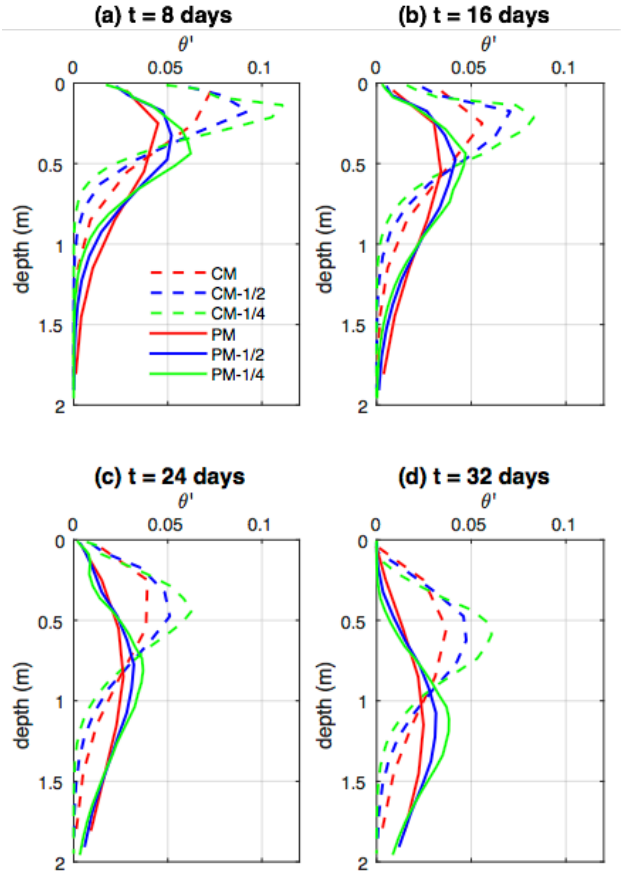

Figure 4-6. Averaged tracer soil moisture profiles (unit: m^3/m^3) derived from WT-Noah-MP with different scenarios at 8 days (a), 16 days (b), 24 days (c) and 32 days (d) after the tagging initiation of each event.

PM-1/2 and PM-1/4 scenarios: Due to the importance of preferential flow through macropores and piston replacement in the soil matrix, we incorporate both partial mixing assumptions of "active/mobile" storage and vertically constrained mixing into the model. As a result, the simulated transit times in Figure 4-5c show less spread-out distributions and lagged rising limbs at deeper levels, both of which are more consistent with those derived from isotopes.

In addition, the PW-1/4 modifies the 100 cm recession limb having a similar time as the rising limb, resulting in a better agreement with the isotope-derived ones.

To conclude, we test different hypotheses of mixing in estimating transit times in subsurface water using WT-Noah-MP. At WS10, the assumption of complete mixing in unsaturated soil results in broader distributions with longer transit times in deeper soil in stark contrast to the isotope-derived transit times from MM2010. For this case in which wet conditions dominate, we find it critical to represent the tracer transit through both preferential flowpaths and piston displacement. To do this in the model framework we incorporate a "mobile" and "immobile" soil moisture storage, and include additional sublayers in the simulation of the tracer transport.

4.4.2 Regional-scale simulation of an extreme precipitation event

In this section, we apply the WT-Noah-MP tool to better understand an extreme event that affected western Washington, USA. Our goal is to demonstrate that in addition to watershed applications, WT-Noah-MP can be used as a tool to investigate the water budget and subsurface time scales of a precipitation event with regional-scale impacts. Using the tracers, we "tag" the precipitation from an extreme precipitation event and track its contribution to different storages and fluxes throughout the terrestrial system.

Partition of AR precipitation into different stores: WT-Noah-MP can help us better quantify the contribution of this AR to different storages over land. Precipitation that falls on the

soil surface can contribute to soil moisture and flooding that causes inundation and direct economic losses, while the precipitation that falls on snowpack might contribute to snow accumulation that is critical for local water resources or rain-on-snow that may trigger snowmelt (Bonne et al. 2015; Guan et al. 2016).

For the date with maximum daily precipitation (00Z December 3, 2007 to 00Z December 4, 2007), up to 75 mm of precipitation fell over the Cascade Mountains (red circle in Fig. 4-7a), while

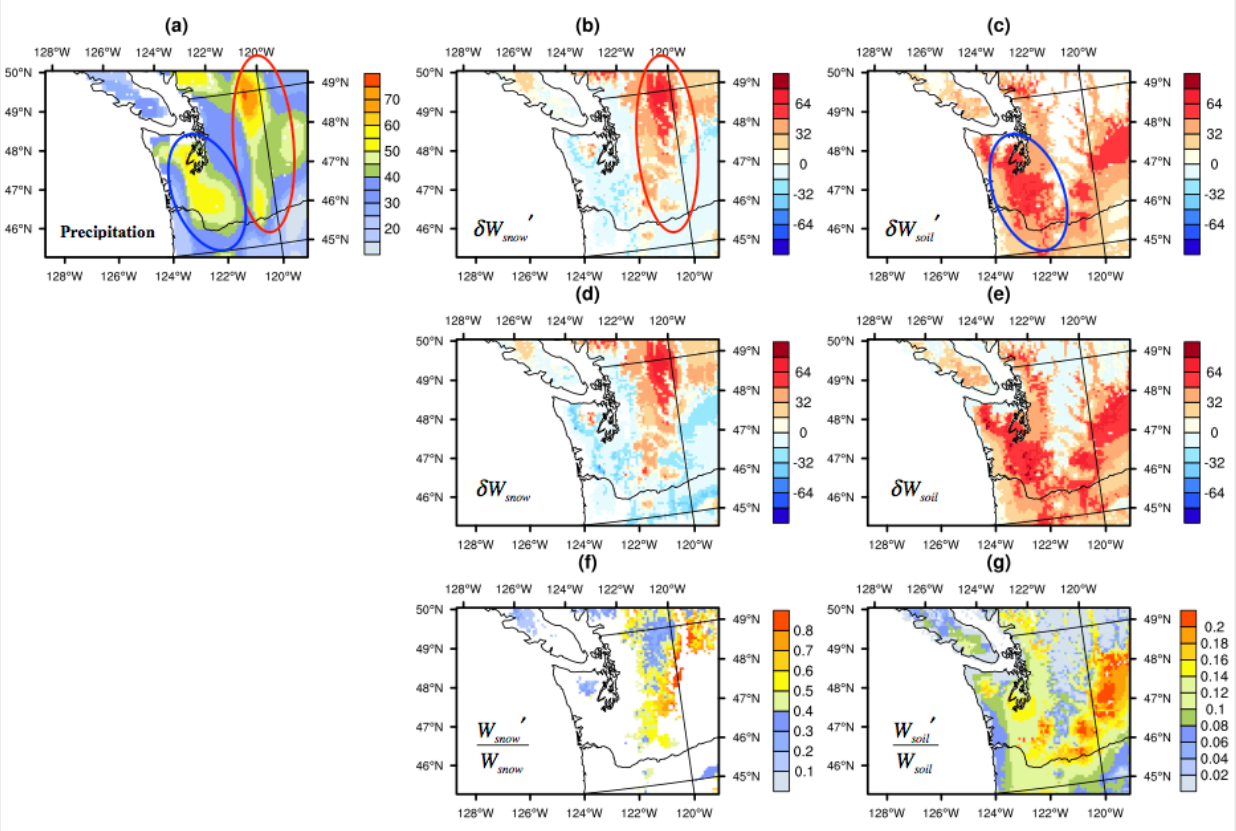

Figure 4-7. (a) The precipitation amount (kg m^{-2}) between 00Z Dec 3, 2007 and 00Z Dec 4, 2007. (b) The differences of snow water equivalent (unit: kg m^{2}) derived from tracers between 00Z Dec 4, 2007 and 00Z Dec 3, 2007; (c) The differences of soil moisture (unit: kg m^{2}) derived from tracers between 00Z Dec 4, 2007 and 00Z Dec 3, 2007; (d) The differences of total snow water equivalent (unit: kg m^{2}) derived from original Noah-MP between 00Z Dec 4, 2007 and 00Z Dec 3, 2007; (e) The differences of total soil moisture (unit: kg m^{2}) derived from original Noah-MP between 00Z Dec 4, 2007 and 00Z Dec 3, 2007; (f) The ratios of snow water equivalent that is >50 kg m^{-2} due to tracers at 00Z Dec 10, 2007; (g) The ratios of soil moisture due to tracers at 00Z Dec 10, 2007. All the results are from WT-Noah-MP with the CM scenario.

up to 60 mm fell on the lower coastal lands (blue circle in Fig. 4-7a). The results derived from WT-Noah-MP clearly reveal that the precipitation over the Cascade Mountains is accumulated as

snow water (Fig. 4-7b), while that over the western low lands and to the southeast of the Cascades was mostly stored as soil moisture (Fig. 4-7c). However, the water tracers are revealing a more nuanced picture. If we only look at the changes in total snow accumulation, we see that there were significant loses (blue regions) in the low-elevation regions (Fig. 4-7d). However, the tracers don't show such significant losses (Fig. 4-7b). This indicates that there was significant melting of the snow that had accumulated before the AR impacted the region. The melted snow then contributed to total soil moisture (Fig. 4-7e), but clearly, changes in soil moisture to the southeast of the Cascades were mostly due to "pre-event" water, rather than tagged water (compare Fig. 4-7e to 4-7c).

Figure 4-8b shows that the total surface runoff is mostly comprised of precipitation from this AR event (85.5%) while the rest 14.5% is contributed by the snowmelt from antecedent snow. A similar estimation is also obtained by Guan et al. (2016) from the rain-on-snow ARs affecting the southwest coast, with ~20% of total runoff from snowmelt. It is a key feature usually associated with extreme ARs, which can exaggerate the quick runoff response of basins because they are usually associated with higher temperatures. Therefore, the WT-Noah-MP tool helps differentiate the role of this AR in causing the extreme flooding into the precipitation from this event (direct) and the indirect thermal effect that triggered snowmelt across the region. By the end the tagged period (00Z Dec 10, 2007), water from the AR event accounts for >15% of soil moisture (Fig. 4-7g) over the low-elevation areas, while snowfall associated with this AR accounts for >50% of

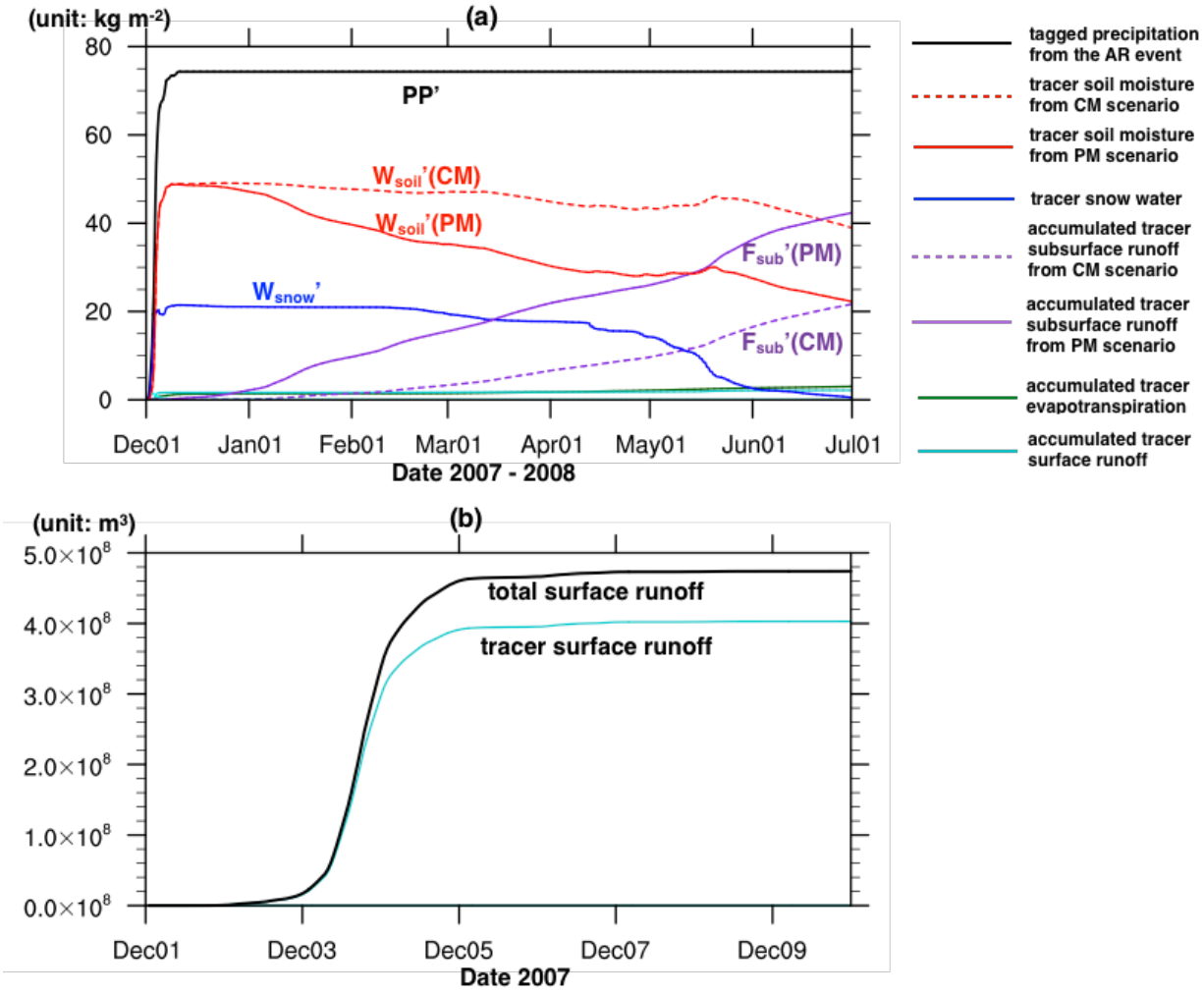

Figure 4-8. (a) Time series of domain-averaged tracer fluxes and storages (see labels and legends). (b) Time series of domain-aggregated surface runoff (solid black) and tracer surface runoff (dashed turquoise) accumulated from 00Z Dec 1, 2007 to 00Z Dec 10, 2007.

snow water over the Cascades (Fig. 4-7f). However, the value of the tracers is perhaps best exemplified when analyzing the tracer water for times after the event has passed.

Subsurface dynamics of AR extending to the seasonal scale: About 2/3 of this AR's precipitation was stored as soil moisture (Fig. 4-8a). Upon the arrival of ARs, they can replenish soil moisture and abruptly end the long-term water deficits between precipitation and evapotranspiration as drought busters (Dettinger 2013). Afterwards, these ARs can have hydroclimate impacts with much longer scales than the event timescale (days), by modifying land-

atmosphere interactions through evapotranspiration and by contributing to subsurface runoff that recharges groundwater and contributes to hydrographs.

From the simulation with CM, the tracers in the soil slowly leave the system as free drainage with a surge in mid-May due to the melting of tracers in snowpack (red dashed line in Fig. 4-8a). The main outflow is through subsurface runoff while the fluxes through evapotranspiration and surface runoff are comparable and small (Fig. 4-8a). By July 1st, 2007, all of the tracers in snow have melted while more than 50% of water from this AR's precipitation is still retained in the soil

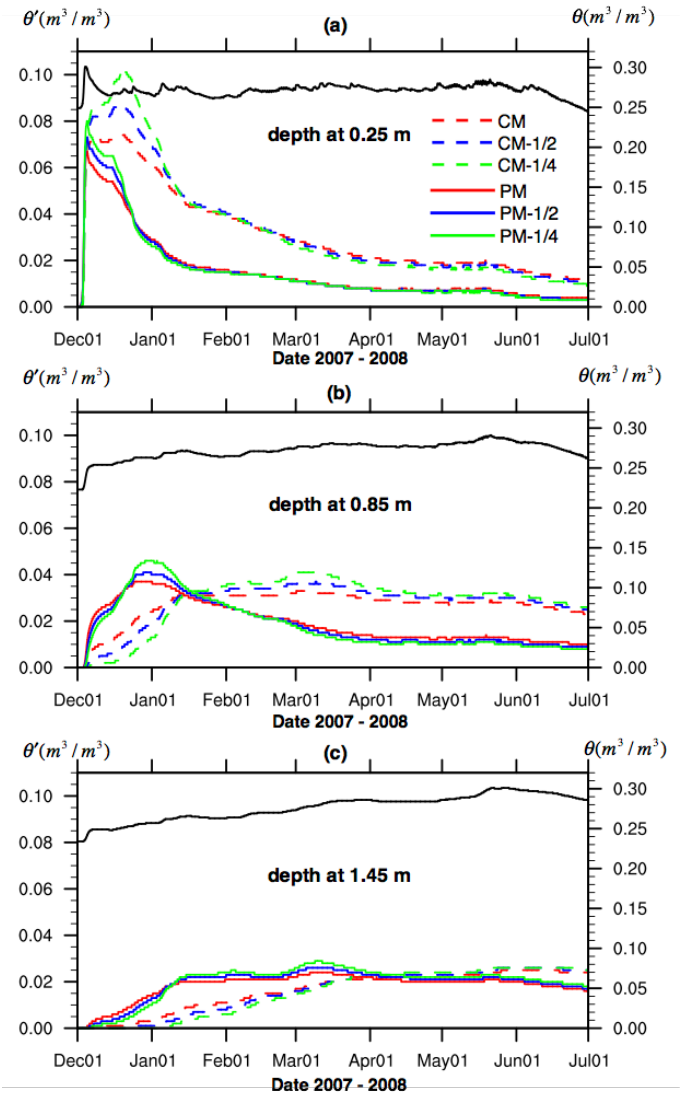

Figure 4-9. WT-Noah-MP simulated soil moisture at 0.25 m (a), 0.85 m (b) and 1.45 m depths (c). The colored curves show the tracer soil moisture (see legends in a) paired with the Y axis on the left, while the black curves show the total soil moisture paired with the Y axis on the right.

moisture storage, suggesting a longer-than-seasonal-timescale transit time of this AR assuming complete mixing.

Including additional sublayers in the soil does not result in large differences of event water stored as soil moisture (compare CM, CM-1/2 and CM-1/4 in Fig. 4-9). However, the simulation with partial mixing (PM) shows faster transit and thus fewer tracers retained in the soil (red solid line in Fig. 4-8a and Fig. 4-9). From Figure 4-9, the decrease of tracer water in the soil occurs preferentially close to the surface (0.25 and 0.85 m) after January, while those at 1.45 m depth have comparable tracer amount from all simulations. As a result, only ~22 kg/m^2 of water that is from this AR is retained in the soil by July 1, 2008 from the PM simulation. This accounts for ~30% of the total precipitation from this AR, suggesting that this event can contribute to local transpiration and especially groundwater recharge after 6 months.

In summary, we use WT-Noah-MP to track the water that originates as precipitation from an AR event. Of the total surface runoff that significantly contributed to local flooding, 85.5% came from the precipitation of this AR while the rest 14.5% came from the snowmelt from antecedent snowpack. However, the surface runoff only consists a small portion of this AR's precipitation. About 2/3 of AR precipitation was stored in the soil immediately after the event, and ~1/3 was stored as snow. During days and months following the event, these stores of water are depleted through runoff or evaporation. The rate at which the water leaves the surface-subsurface system depends on the different mixing assumptions. The CM simulation shows the largest amount of tracers retained in the soil and the slowest transit out, consistent with that in WS10 experiments. In the PM simulation, event water leaves the system at a faster rate through subsurface runoff (see purple line of Fig. 4-8a), thus depleting soil moisture. The soil moisture conditions before the December 3 event occurred were anomalously wet, as two previous storms had impacted the region

in the days leading up to the AR. For this reason, we hypothesize that the PM simulation more realistically captures the transit times in the system. However, without regional-scale observations, we cannot test our hypothesis. For this reason, the CM and PM simulations provide an "envelope of uncertainty" regarding the transit time distributions in the basin. Regardless of the assumptions used, approximately 30% of the AR's precipitation remains in the soil after 6 months. This result allows us to quantify the residence time of this extreme event in the terrestrial hydrologic system.

4.4.3 Comments

In the two examples above, we illustrate the use of WV-Noah-MP to track event-based water in (1) a detailed examination of subsurface transit at the watershed scale and (2) a regional-scale event water budget analysis. Unlike isotope-enabled LSMs, we trace the total event-based water and not the isotopes. For this reason, no isotopic data is required to drive the tracer module because we only need the total water amount from the "tagged" event as tracer input. This data can be derived from the forcing (precipitation) used to drive any regular LSM. Since we are tracing the actual water, no fractionation process need to be included, reducing the uncertainty and making the interpretation more straightforward. For these reasons, the new numerical water tracer tool makes it possible to investigate event-based physical processes in a wide range of spatial and temporal scales.

However, we still require isotope observations to validate our results. In our application to WS10, the isotope data collected from field experiments and its derived transit time distribution by MM2010 becomes a key benchmark to test the mixing assumptions that allow different subsurface flow regimes. Because the water tracer model does not provide isotope data, we convert the tracer results into transit times. On the other hand, the output from an isotope-enabled LSM would be directly comparable to isotope observations. It is clear that, while the goal of numerical

water tracers in LSMs and isotope-enabled LSMs is similar—to track the movement of water through the surface-subsurface modeling system—each tool has its own strengths and weaknesses (see Table 4-4). The two methods can be used as complementary tools to track water through the terrestrial system.

When compared with isotopic observations, WT-Noah-MP is a powerful tool that can provide a critical test for the physical processes represented in the model. As an example, isotope observations have shown that plants uptake water from different soil depths (e.g. Ehleringer and Dawson 1992), WT-Noah-MP can be used to evaluate if the model is appropriately representing plant water uptake depth. More generally, isotopic studies have identified an ecohydrological separation of soil water: the water transpired from plants is different from water that contributes to streamflow (Brooks et al. 2009; Evaristo et al. 2015). Water tracers can be used as a tool to improve LSMs so they better represent these compartments. Isotopic studies are critical for understanding the water cycle and the linked ecological processes (Good et al. 2015), but in general, LSMs have lagged far behind the isotopic observations. WT-Noah-MP and the existing isotope-enabled models can help bridge the gap between the observations and models.

Table 4-4. Comparison of the two tracer tools in LSMs

	Stable water isotope tracers	"Numerical" water tracers
Tracking objective	Compositions of $^{1}H^{2}H^{16}O$ and $^{1}H_{2}{}^{18}O$	Total amount of water sourced from a precipitation event (event water)
Similarities	Track the movement of water molecules in LSM and reveal the characteristics of different processes parameterized by the model (diagnostic tools for model's performance)	
Differences	• Provide a seamless interface with isotope observations • Help interpret isotopic signals in association with climate variation and climate changes in the past	• No isotope data is required to drive the tracer module • No de-convolution / inversion is required interpret the result • No fractioning parameterization

It is important to clarify that due to the simple runoff scheme of our simulations, water leaves the bottom soil layer as free drainage. Thus, we are not able to resolve the effect of bedrock permeability that is one of the main geological controls on catchment transit times (Hale and McDonnell 2016; Pfister et al. 2017). In addition, Noah-MP does not take the vertical variation of saturated hydraulic conductivity into account. Both of these processes contribute to the dry bias of soil moisture in deeper layers at WS10 and are likely to affect the estimation of transit times. Furthermore, the partitioning of half storage to be "active/mobile" is arbitrary and could be improved by parameterizing it as a function of soil moisture (e.g. Fenicia et al. 2010; Hrachowitz et al. 2013). These could be subjects to be improved in the future.

4.5 Conclusions

We have presented a new water tracer tool specifically designed to track individual hydrometeorological events—shifting the LSM approach from bulk estimation of storages and fluxes to an explicit representation of event water transit. We implement this numerical water tracer scheme in Noah-MP (WT-Noah-MP). The new numerical water tracers tag the total water from precipitation events of interest and track the subsequent partitioning and movement in the surface-subsurface continuum. In comparison to existing LSMs that incorporate isotopes, our water tracer tool does not require isotopic information as either initial conditions or boundary forcing, nor does it require the parameterization of isotopic fractionation processes. We believe WT-Noah-MP is complementary to existing isotope-enabled LSMs. The new water tracer tool allows for a long-term tracking of a specific precipitation events and a straightforward interpretation of hydrological processes. Noah-MP is the first LSM with this numerical water tracer capability.

In the tracer implementation, we make particular efforts to appropriately account for horizontal and vertical heterogeneity in mixing during subsurface transit. This is necessary because the "complete mixing" assumption (CM) usually causes an artificially long transit time. Therefore, to account for tracer transit through preferential flow pathways, which would usually result in a faster transit and is critical for wet soil conditions, we approximate the mixing and transfer of tracers only occurring in the part of storage that is "active/mobile". In this study, we test this approximation by specifying half of the total storage to be "active/mobile" (PM). In addition, to better preserve the tracer penetration as piston flow in the soil matrix, we discretize thinner soil layers for mixing so that tracers can percolate with less dispersion. We test this assumption by allowing mixing in ½ an ¼ of each original soil layer (PM-1/2 and PM-1/4).

The different mixing assumptions are tested in a well-studied watershed WS10 in Oregon over a period after soil wet-up. Comparing the transit times estimated from our water tracer tool and those from isotopic measurements (MM2010), the PM run significantly improves the transit time estimations in deeper soils (70 and 100 cm) when compared to the unrealistically longer transit times in the CM simulation. The PM-1/2 and PM-1/4 estimations further improve the transit time distributions, suggesting a more realistic tracer transit taking both preferential flow and piston flow into account, especially under wet soil conditions. We then use WT-Noah-MP to investigate the effect of an extreme AR event in December 2007 over Western Washington. While the CM simulation shows most of the tracers retained in the soil until July 2008, perhaps a more realistic estimation comes from the PM simulation with a faster transit of tracers and ~30% of this AR's total precipitation retained in the soil by July 2008. This event water retained in the soil can contribute to local evapotranspiration, groundwater recharge and base flow. Above the soil, we use WT-Noah-MP to differentiate and quantify the "direct" (runoff from this AR's

precipitation) and “indirect” (snowmelt trigged by the warm feature of this AR) effects to flooding which are difficult to derive from the original Noah-MP but simple to understand using the tracers. This additional information is valuable because it helps anticipate possible changes of ARs’ hydrologic consequence based on antecedent snow conditions and thermodynamic changes.

CHAPTER 5: SUMMARY

In the previous three chapters, we examined three different aspects of Atmospheric Rivers (ARs) characterized by different scales: Rossby wave behavior, tropical moisture export and land surface conditions. Each of them are linked with regional and local hydrological impacts in order to better understand the spatio-temporal variability of ARs over land and to better predict the risk of flooding and water availability related to ARs.

As the vapor transport component embedded in Rossby waves, ARs can be significantly modulated by the dynamics of their parent synoptic eddies. Indeed, we found that ARs in association with the two different Rossby wave breaking modes have different features in vapor transport strength and impinging angle towards the coast. ARs in association with anticyclonic wave breaking (AWB-ARs) are characterized by more zonal impinging angles. On the other hand, ARs associated with cyclonic wave breaking (CWB-ARs) have more meridional impingement offshore and have stronger vapor transport for ARs affecting the Southwest Coast. Through the interactions between these features and local mountains, AWB-ARs are responsible for most extreme flooding events for the coastal river basins in the Northwest Coast, while CWB-ARs account for the majority of flooding for the coastal basins in the Southwest Coast. This study is well aligned with recent studies aimed at understanding large-scale and upper-level dynamics in modulating moisture transport features including ARs (e.g. Ryoo et al. 2013; Payne and Magnusdottir 2014; Ryoo et al. 2015; Payne and Magnusdottir 2015; Liu and Barnes 2015), but with a unique emphasis on local impacts including streamflow. We believe that these connections with large-scale dynamics being established can be used to better understand the interactions between local water availability and atmospheric variabilities.

In addition to dynamic changes, thermodynamic factors can significantly induce AR changes (Lavers et al. 2013; Shields and Kiehl 2016; Payne and Magnusdottir 2015). In a similar way as parent extratropical cyclones can be intensified by latent heating, thermal and moisture conditions associated with ARs can modify AR strength and landfall characteristics. Using a water vapor tracer tool, we "tag" tropical moisture to understand its role in landfalling ARs. Significantly stronger pre-cold-frontal low-level jets (LLJs) are associated with ARs with greater contributions from tropical moisture due to the enhancement of positive potential vorticity induced by cold-frontal rainbands; larger export of tropical moisture along ARs also associated with warmer air advection, tends to enhance synoptic ascent and results in warmer air temperature. This is the first study to statistically establish the relationships between moisture sources and AR precipitation strength over land. In addition, this study proves the importance of direct export of tropical moisture to ARs' leading edges, contributing additional insight to the ongoing debate about moisture sources from remote tropical sources vs. local moisture convergence (Bao et al. 2006; Knippertz and Wernli 2010; Sodemann and Stohl 2013; Dacre et al. 2015; Eiras-Barca et al. 2017).

While the first two studies focus on atmospheric processes related to AR precipitation, in the third part of the dissertation we shift our focus onto terrestrial processes. These processes play a key role determining the local responses to landfalling ARs. To isolate the antecedent terrestrial conditions (snow and soil moisture) from AR precipitation, we developed a water tracer tool in the model framework of the Noah-Multiparameterization land surface model, and used this tracer tool to tag precipitation from individual AR events. By tagging an extreme AR event in December 2007, we found a 16% enhancement of runoff due to snowmelt in addition direct contribution from AR precipitation. Perhaps a more interesting finding from this study is the timescale of ARs' lifecycle over land. We test the tracer mixing assumptions in the estimation of residence times

averaged for 11 AR events using observations from WS10 watershed (Oregon). For the extreme December 2007 event, we found that the majority of the event water is retained in the local terrestrial system after 6 months. This provides a new perspective to understand the residence time of AR events, not only focusing on the preceding processes that are important in producing extreme precipitation and floods, but also noticing the long-term memory and hydroclimatological impacts left by these ARs on the terrestrial system.

Each of these features, highlighted by the previous three chapters, represent very distinct processes in scales and physics that ARs can be associated with. This in turn emphasizes the importance to view AR-related processes as an integrated system. In fact, all these aspects are interconnect. For instance, significant export of tropical moisture to ARs might require Rossby waves with certain equatorward displacement and meridional extension (Ralph et al. 2011; Hagos et al. 2015); subsequently, tropical moisture entrained within ARs can both lead to increases in precipitation and warm anomalies that may trigger snowmelt and enhance streamflow responses (Neiman et al. 2008b). Also, all these features are likely to change in a warmer climate: RWB patterns may shift poleward in association with the poleward migration of jet streams projected by climate models (Barnes and Hartmann 2012); moisture holding capacity would increase in line with the Clausius-Clapeyron relationship with global warming (Meehl), especially in the tropics; snow conditions may change and intensification of precipitation in extreme ARs are likely to occur. All of these may lead to very different local impacts than in the current climate. Here, we built individual connections between the three aspects and AR's local impacts that can hopefully be used to better interpret AR variations under the evolving Earth system and improving our ability to predict and prepare for these events.

REFERENCES

Aleinov, I., and G. A. Schmidt, 2006: Water isotopes in the GISS ModelE land surface scheme. *Global and Planetary Change*, **51**, 108–120, doi:10.1016/j.gloplacha.2005.12.010.

Allen, S. T., J. R. Brooks, R. F. Keim, B. J. Bond, and J. J. McDonnell, 2013: The role of pre-event canopy storage in throughfall and stemflow by using isotopic tracers. *Ecohydrol*, **7**, 858–868, doi:10.1002/eco.1408.

Anders, R., K. Davidek, and D. M. Stoeckel, 2011: *Water-Quality Data for the Russian River Basin, Mendocino and Sonoma Counties, California, 2005–2010*. 133 pp. http://pubs.usgs.gov/ds/610/pdf/ds610.pdf.

Bao, J. W., S. A. Michelson, and P. J. Neiman, 2006: Interpretation of enhanced integrated water vapor bands associated with extratropical cyclones: Their formation and connection to tropical moisture. *Mon. Wea. Rev*, **134**, 1063–1080, doi:10.1175/MWR3123.1.

Barlage, M., M. Tewari, F. Chen, G. Miguez-Macho, Z.-L. Yang, and G.-Y. Niu, 2015: The effect of groundwater interaction in North American regional climate simulations with WRF/Noah-MP. *Climatic Change*, **129**, 485–498, doi:10.1007/s10584-014-1308-8.

Barnes, E. A., and D. L. Hartmann, 2012: Detection of Rossby wave breaking and its response to shifts of the midlatitude jet with climate change. *J. Geophys. Res*, **117**, D09117–D09117, doi:10.1029/2012JD017469.

Birkel, C., C. Soulsby, D. Tetzlaff, S. Dunn, and L. Spezia, 2011: High-frequency storm event isotope sampling reveals time-variant transit time distributions and influence of diurnal cycles. *Hydrol. Process*, **26**, 308–316, doi:10.1002/hyp.8210.

Bonne, J.-L., H. C. Steen-Larsen, C. Risi, M. Werner, H. Sodemann, J.-L. Lacour, and X. Fettweis, 2015: The summer 2012 Greenland heat wave: In situ and remote sensing observations of water vapour isotopic composition during an atmospheric river event. **10**, 2970–2989, doi:10.1002/(ISSN)2169-8996.

Braud, I., T. Bariac, J. P. Gaudet, and M. Vauclin, 2005: SiSPAT-Isotope, a coupled heat, water and stable isotope (HDO and H218O) transport model for bare soil. Part I. Model description and first verifications. *JOURNAL OF HYDROLOGY*, **309**, 277–300, doi:10.1016/j.jhydrol.2004.12.013.

Brooks, J. R., H. R. Barnard, R. Coulombe, and J. J. McDonnell, 2009: Ecohydrologic separation of water between trees and streams in a Mediterranean climate. *Nature Geoscience*, **3**, 100–104, doi:10.1038/ngeo722.

Browning, K. A., 1985: Conceptual Models of Precipitation Systems. *Meteorological Magazine*, **114**, 293–319.

Browning, K. A., 1999: Mesoscale Aspects of Extratropical Cyclones: An Observational Perspective. *The Life Cycles of Extratropical Cyclones*, American Meteorological Society, Boston, MA, 265–283.

Buttle, J. M., 1994: Isotope hydrograph separations and rapid delivery of pre-event water from drainage basins. *Progress in Physical Geography*, **18**, 16–41, doi:10.1177/030913339401800102.

Buttle, J. M., and D. J. McDonald, 2002: Coupled vertical and lateral preferential flow on a forested slope. *Water Resour. Res*, **38**, 18–1–18–16, doi:10.1029/2001WR000773.

Cai, X., Z.-L. Yang, C. H. David, G.-Y. Niu, and M. Rodell, 2014: Hydrological evaluation of the Noah-MP land surface model for the Mississippi River Basin. *J. Geophys. Res. Atmos*, **119**, 23–38, doi:10.1002/2013JD020792.

Carlson, T. N., 1980: Airflow through midlatitude cyclones and the comma cloud pattern. *Mon. Wea. Rev*, **108**, 1498–1509, doi:10.1175/1520-0493(1980)108<1498:ATMCAT>2.0.CO;2.

Carlyle-Moses, D. E., and J. H. C. Gash, 2011: Rainfall Interception Loss by Forest Canopies. *Forest Hydrology and Biogeochemistry*, Vol. 216 of *Ecological Studies*, Springer Netherlands, Dordrecht, 407–423.

Cayan, D. R., and J. O. Roads, 1984: Local relationships between United States West Coast precipitation and monthly mean circulation parameters. *Mon. Wea. Rev*, **112**, 1276–1282, doi:10.1175/1520-0493(1984)112<1276:LRBUSW>2.0.CO;2.

Clapp, R. B., and G. M. Hornberger, 1978: Empirical equations for some soil hydraulic properties. *Water Resour. Res*, **14**, 601–604, doi:10.1029/WR014i004p00601.

Colle, B. A., 2004: Sensitivity of orographic precipitation to changing ambient conditions and terrain geometries: An idealized modeling perspective. *J. Atmos. Sci*, **61**, 588–606, doi:10.1175/1520-0469(2004)061<0588:SOOPTC>2.0.CO;2.

Dacre, H. F., P. A. Clark, O. Martinez-Alvarado, M. A. Stringer, and D. A. Lavers, 2015: How Do Atmospheric Rivers Form? *Bull. Amer. Meteor. Soc*, **96**, 1243–1255, doi:10.1175/BAMS-D-14-00031.1.

Dee, D. P., and Coauthors, 2011: The ERA-Interim reanalysis: configuration and performance of the data assimilation system. *Quart. J. Roy. Meteor. Soc*, **137**, 553–597, doi:10.1002/qj.828.

Dettinger, M., 2011: Climate Change, Atmospheric Rivers, and Floods in California - A Multimodel Analysis of Storm Frequency and Magnitude Changes1. *JAWRA Journal of the American Water Resources Association*, **47**, 514–523, doi:10.1111/j.1752-1688.2011.00546.x.

Dettinger, M. D., 2013: Atmospheric Rivers as Drought Busters on the US West Coast. *J. Hydrometeor*, **14**, 1721–1732, doi:10.1175/JHM-D-13-02.1.

Dettinger, M. D., F. M. Ralph, T. Das, P. J. Neiman, and D. R. Cayan, 2011: Atmospheric rivers, floods and the water resources of California. *Water*, **3**, 445–478, doi:10.3390/w3020445.

Dominguez, F., and Coauthors, 2018: Tracking an atmospheric river in a warmer climate: from water vapor to economic impacts. *Earth Syst. Dynam*, **9**, 249–266, doi:10.5194/esd-9-249-2018.

Dominguez, F., G. Miguez-Macho, and H. Hu, 2016: WRF with Water Vapor Tracers: A Study of Moisture Sources for the North American Monsoon. *J. Hydrometeor*, **17**, 1915–1927, doi:10.1175/JHM-D-15-0221.1.

Ehleringer, J. R., and T. E. Dawson, 1992: Water-Uptake by Plants - Perspectives From Stable Isotope Composition. *Plant Cell and Environment*, **15**, 1073–1082, doi:10.1111/j.1365-3040.1992.tb01657.x.

Eiras-Barca, J., F. Dominguez, H. Hu, A. D. Garaboa-Paz, and G. Miguez-Macho, 2017: Evaluation of the Moisture Sources in two Extreme Landfalling Atmospheric River Events using an Eulerian WRF-Tracers tool. *Earth Syst. Dynam. Discuss*, 1–21, doi:10.5194/esd-2017-63.

Ek, M. B., K. E. Mitchell, Y. Lin, E. Rogers, P. Grunmann, V. Koren, G. Gayno, and J. D. Tarpley, 2003: Implementation of Noah land surface model advances in the National Centers for Environmental Prediction operational mesoscale Eta model. *J. Geophys. Res. Atmos*, **108**, doi:10.1029/2002JD003296.

EMANUEL, K. A., M. FANTINI, and A. J. THORPE, 1987: Baroclinic Instability in an Environment of Small Stability to Slantwise Moist Convection .1. Two-Dimensional Models. *J. Atmos. Sci*, **44**, 1559–1573.

Evaristo, J., S. Jasechko, and J. J. McDonnell, 2015: Global separation of plant transpiration from groundwater and streamflow. *Nature*, **525**, 91–94, doi:10.1038/nature14983.

Feng, X., S. Taylor, C. E. Renshaw, and J. W. Kirchner, 2002: Isotopic evolution of snowmelt 1. A physically based one-dimensional model. *Water Resour. Res*, **38**, 35–1–35–8, doi:10.1029/2001WR000814.

Fenicia, F., S. Wrede, D. Kavetski, L. Pfister, L. Hoffmann, H. H. G. Savenije, and J. J. McDonnell, 2010: Assessing the impact of mixing assumptions on the estimation of streamwater mean residence time. *Hydrol. Process*, **24**, 1730–1741, doi:10.1002/hyp.7595.

Fischer, M. J., 2006: iCHASM, a flexible land-surface model that incorporates stable water isotopes. *Global and Planetary Change*, **51**, 121–130, doi:10.1016/j.gloplacha.2005.12.008.

Fischer, M. J., and K. Sturm, 2006: REMOiso forcing for the iPILPS Phase 1 experiments and the performance of REMOiso in three domains. *Global and Planetary Change*, **51**, 73–89, doi:10.1016/j.gloplacha.2005.12.006.

Gao, Y., J. Lu, L. R. Leung, Q. Yang, S. Hagos, and Y. Qian, 2015: Dynamical and

thermodynamical modulations on future changes of landfalling atmospheric rivers over western North America. *Geophys. Res. Lett*, **42**, 7179–7186, doi:10.1002/2015GL065435.

Gat, J. R., 1996: Oxygen and hydrogen isotopes in the hydrologic cycle. *Annual Review of Earth and Planetary Sciences*, **24**, 225–262, doi:10.1146/annurev.earth.24.1.225.

Genereux, D. P., and R. P. Hooper, 1998: Oxygen and Hydrogen Isotopes in Rainfall-Runoff Studies. *Isotope Tracers in Catchment Hydrology*, Elsevier, 319–346.

Gimeno, L., 2014: Atmospheric rivers: a mini-review. 1–6, doi:10.3389/feart.2014.00002/abstract.

Gochis, D. J., W. Yu, and D. N. Yates, 2013: *The WRF-Hydro model technical description and user's guide, version 1.0*. NCAR Tech. Doc.

Godsey, S. E., J. W. Kirchner, and D. W. Clow, 2009: Concentration-discharge relationships reflect chemostatic characteristics of US catchments. *Hydrol. Process*, **23**, 1844–1864, doi:10.1002/hyp.7315.

Good, S. P., D. Noone, and G. Bowen, 2015: Hydrologic connectivity constrains partitioning of global terrestrial water fluxes. *Science*, **349**, 175–177, doi:10.1126/science.aaa5931.

Guan, B., and D. E. Waliser, 2016: Detection of atmospheric rivers: Evaluation and application of an algorithm for global studies. *J. Geophys. Res. Atmos*, 1–22, doi:10.1002/(ISSN)2169-8996.

Guan, B., D. E. Waliser, F. M. Ralph, E. J. Fetzer, and P. J. Neiman, 2016: Hydrometeorological characteristics of rain-on-snow events associated with atmospheric rivers. *Geophys. Res. Lett*, **10**, 2964–2973, doi:10.1002/(ISSN)1944-8007.

Guan, B., N. P. Molotch, D. E. Waliser, E. J. Fetzer, and P. J. Neiman, 2010: Extreme snowfall events linked to atmospheric rivers and surface air temperature via satellite measurements. *Geophys. Res. Lett*, **37**, 1–6, doi:10.1029/2010GL044696.

Haese, B., M. Werner, and G. Lohmann, 2013: Stable water isotopes in the coupled atmosphere?land surface model ECHAM5-JSBACH. *Geosci. Model Dev*, **6**, 1463–1480, doi:10.5194/gmd-6-1463-2013.

Hagos, S., L. R. Leung, Q. Yang, C. Zhao, and J. Lu, 2015: Resolution and Dynamical Core Dependence of Atmospheric River Frequency in Global Model Simulations. *J. Climate*, **28**, 2764–2776, doi:10.1175/JCLI-D-14-00567.1.

Hale, V. C., and J. J. McDonnell, 2016: Effect of bedrock permeability on stream base flow mean transit time scaling relations: 1. A multiscale catchment intercomparison. *Water Resour. Res*, **52**, 1358–1374, doi:10.1002/2014WR016124.

Hayes, J. L., 2008: *Service Assessment*. 39 pp. http://www.nws.noaa.gov/om/assessments/pdfs/pac_nw08.pdf.

Henderson-Sellers, A., 2006: Improving land-surface parameterization schemes using stable water isotopes: Introducing the ?iPILPS? initiative. *Global and Planetary Change*, **51**, 3–24, doi:10.1016/j.gloplacha.2005.12.009.

Hong, S. Y., and J. Lim, 2006: The WRF single-moment 6-class microphysics scheme (WSM6). *J. Korean Meteor. Soc*, **42**, 129–151.

Hong, S.-Y., and H.-L. Pan, 1996: Nonlocal Boundary Layer Vertical Diffusion in a Medium-Range Forecast Model. *Mon. Wea. Rev*, **124**, 2322–2339, doi:10.1175/1520-0493(1996)124<2322:NBLVDI>2.0.CO;2.

Hoskins, B. J., A. J. Simmons, and D. G. Andrews, 1977: Energy Dispersion in a Barotropic Atmosphere. *Quart. J. Roy. Meteor. Soc*, **103**, 553–567, doi:10.1002/qj.49710343802.

Houze, R. A., Jr., 2012: Orographic effects on precipitating clouds. *Rev. Geophys*, **50**, RG1001, doi:10.1029/2011RG000365.

Hrachowitz, M., C. Soulsby, D. Tetzlaff, J. J. C. Dawson, S. M. Dunn, and I. A. Malcolm, 2009: Using long-term data sets to understand transit times in contrasting headwater catchments. *JOURNAL OF HYDROLOGY*, **367**, 237–248, doi:10.1016/j.jhydrol.2009.01.001.

Hrachowitz, M., H. Savenije, T. A. Bogaard, D. Tetzlaff, and C. Soulsby, 2013: What can flux tracking teach us about water age distribution patterns and their temporal dynamics? *Hydrol. Earth Syst. Sci*, **17**, 533–564, doi:10.5194/hess-17-533-2013.

Hrachowitz, M., P. Benettin, B. M. van Breukelen, O. Fovet, N. J. K. Howden, L. Ruiz, Y. van der Velde, and A. J. Wade, 2016: Transit times-the link between hydrology and water quality at the catchment scale. *WIREs Water*, **3**, 629–657, doi:10.1002/wat2.1155.

Hu, H., and F. Dominguez, 2018: The Role of Tropical Moisture Export to Atmospheric Rivers' vapor transport and landfall. 1–1.

Hu, H., F. Dominguez, P. Kumar, J. J. McDonnell, and D. Gochis, 2018: *A Numerical Water Tracer Model for Understanding Event Scale Hydrometeorological Phenomena*. 47 pp.

Hu, H., F. Dominguez, Z. Wang, D. A. Lavers, G. Zhang, and F. M. Ralph, 2017: Linking Atmospheric River Hydrological Impacts on the U.S. West Coast to Rossby Wave Breaking. *J. Climate*, **30**, 3381–3399, doi:10.1175/JCLI-D-16-0386.1.

Insua-Costa, D., and G. Miguez-Macho, 2018: A new moisture tagging capability in the Weather Research and Forecasting model: formulation, validation and application to the 2014 Great Lake-effect snowstorm. *Earth Syst. Dynam*, **9**, 167–185, doi:10.5194/esd-9-167-2018.

Jones, J. A., 2000: Hydrologic processes and peak discharge response to forest removal, regrowth, and roads in 10 small experimental basins, western Cascades, Oregon. *Water Resour. Res*, **36**, 2621–2642, doi:10.1029/2000WR900105.

Judy, C., J. R. Meiman, and I. Friedman, 1970: Deuterium variations in an annual snowpack.

Water Resour. Res, **6**, 125–129, doi:10.1029/WR006i001p00125.

Kain, J. S., 2004: The Kain–Fritsch convective parameterization: an update. *J. Appl. Meteo*, **43**, 170–181.

Kendall, C., and J. J. McDonnell, 1998: *Isotope tracers in catchment hydrology*.

Kendall, C., and T. B. Coplen, 2001: Distribution of oxygen-18 and deuterium in river waters across the United States. *Hydrol. Process*, **15**, 1363–1393, doi:10.1002/hyp.217.

Klaus, J., and J. J. McDonnell, 2013: Hydrograph separation using stable isotopes: Review and evaluation. *JOURNAL OF HYDROLOGY*, **505**, 47–64, doi:10.1016/j.jhydrol.2013.09.006.

Klaus, J., K. P. Chun, K. J. McGuire, and J. J. McDonnell, 2015: Temporal dynamics of catchment transit times from stable isotope data. *Water Resour. Res*, **51**, 4208–4223, doi:10.1002/2014WR016247.

Knippertz, P., and H. Wernli, 2010: A Lagrangian Climatology of Tropical Moisture Exports to the Northern Hemispheric Extratropics. *J. Climate*, **23**, 987–1003, doi:10.1175/2009JCLI3333.1.

L'Heureux, M. L., and D. Thompson, 2006: Observed relationships between the El Niño-Southern Oscillation and the extratropical zonal-mean circulation. *J. Climate*, **19**, 276–287.

Lackmann, G. M., 2002: Cold-frontal potential vorticity maxima, the low-level jet, and moisture transport in extratropical cyclones. *Mon. Wea. Rev*, **130**, 59–74, doi:10.1175/1520-0493(2002)130<0059:CFPVMT>2.0.CO;2.

Lavers, D. A., and G. Villarini, 2013: The nexus between atmospheric rivers and extreme precipitation across Europe. *Geophys. Res. Lett*, **40**, 3259–3264, doi:10.1002/grl.50636.

Lavers, D. A., G. Villarini, R. P. Allan, E. F. Wood, and A. J. Wade, 2012: The detection of atmospheric rivers in atmospheric reanalyses and their links to British winter floods and the large-scale climatic circulation. *J. Geophys. Res*, **117**, D20106, doi:10.1029/2012JD018027.

Lavers, D. A., R. P. Allan, G. Villarini, B. Lloyd-Hughes, D. J. Brayshaw, and A. J. Wade, 2013: Future changes in atmospheric rivers and their implications for winter flooding in Britain. *Environ. Res. Lett*, **8**, 034010, doi:10.1088/1748-9326/8/3/034010.

Leaney, F. W., K. Smettem, and D. J. Chittleborough, 1993: Estimating the contribution of preferential flow to subsurface runoff from a hillslope using deuterium and chloride. *JOURNAL OF HYDROLOGY*, **147**, 83–103, doi:10.1016/0022-1694(93)90076-L.

Lee, J., X. Feng, A. Faiia, E. Posmentier, R. Osterhuber, and J. Kirchner, 2010: Isotopic evolution of snowmelt: A new model incorporating mobile and immobile water. *Water Resour. Res*, **46**, 387–12, doi:10.1029/2009WR008306.

Leung, L. R., and Y. Qian, 2009: Atmospheric rivers induced heavy precipitation and flooding in

the western U.S. simulated by the WRF regional climate model. *Geophys. Res. Lett*, **36**, L03820–L03826, doi:10.1029/2008GL036445.

Leung, L. R., Y. Qian, X. Bian, W. M. Washington, J. Han, and J. O. Roads, 2004: Mid-Century Ensemble Regional Climate Change Scenarios for the Western United States. *Climatic Change*, **62**, 75–113, doi:10.1023/B:CLIM.0000013692.50640.55.

Liu, C., and E. A. Barnes, 2015: Extreme moisture transport into the Arctic linked to Rossby wave breaking. *J. Geophys. Res. Atmos*, **120**, 3774–3788, doi:10.1002/2014JD022796.

Livneh, B., E. A. Rosenberg, C. Lin, and B. Nijssen, 2013: A Long-Term Hydrologically Based Dataset of Land Surface Fluxes and States for the Conterminous United States: Update and Extensions. *J. Climate*, **26**, 9384–9392, doi:10.1175/JCLI-D-12-00508.s1.

Lundquist, J. D., P. J. Neiman, B. Martner, A. B. White, D. J. Gottas, and F. M. Ralph, 2008: Rain versus Snow in the Sierra Nevada, California: Comparing Doppler Profiling Radar and Surface Observations of Melting Level. *J. Hydrometeor*, **9**, 194–211, doi:10.1175/2007JHM853.1.

Marsh, P., and M. K. Woo, 2010: Wetting front advance and freezing of meltwater within a snow cover: 2. A simulation model. *Water Resour. Res*, **20**, 1865–1874, doi:10.1029/WR020i012p01865.

Martinez, J. A., and F. Dominguez, 2016: Impacts of a Groundwater Scheme on Hydroclimatological Conditions over Southern South America. *J. Hydrometeor*, doi:10.1175/JHM-D-16-0052.s1.

Mass, C., A. Skalenakis, and M. Warner, 2011: Extreme Precipitation over the West Coast of North America: Is There a Trend? *J. Hydrometeor*, **12**, 310–318, doi:10.1175/2010JHM1341.1.

McDonnell, J. J., 1990: A Rationale for Old Water Discharge Through Macropores in a Steep, Humid Catchment. *Water Resour. Res*, **26**, 2821–2832, doi:10.1029/WR026i011p02821.

McDonnell, J. J., 2017: Beyond the water balance. *Nature Geoscience*, **10**, 396–396, doi:10.1038/ngeo2964.

McDonnell, J. J., and K. Beven, 2014: Debates-The future of hydrological sciences: A (common) path forward? A call to action aimed at understanding velocities, celerities and residence time distributions of the headwater hydrograph. *Water Resour. Res*, **50**, 5342–5350, doi:10.1002/2013WR015141.

McGuire, K. J., and J. J. McDonnell, 2006: A review and evaluation of catchment transit time modeling. *JOURNAL OF HYDROLOGY*, **330**, 543–563, doi:10.1016/j.jhydrol.2006.04.020.

McGuire, K. J., and J. J. McDonnell, 2010: Hydrological connectivity of hillslopes and streams: Characteristic time scales and nonlinearities. *Water Resour. Res*, **46**, n/a–n/a, doi:10.1029/2010WR009341.

McGuire, K. J., D. R. DeWalle, and W. J. Gburek, 2002: Evaluation of mean residence time in subsurface waters using oxygen-18 fluctuations during drought conditions in the mid-Appalachians. *JOURNAL OF HYDROLOGY*, **261**, 132–149, doi:10.1016/S0022-1694(02)00006-9.

McGuire, K. J., J. J. McDonnell, M. Weiler, C. Kendall, B. L. McGlynn, J. M. Welker, and J. Seibert, 2005: The role of topography on catchment-scale water residence time. *Water Resour. Res*, **41**, n/a–n/a, doi:10.1029/2004WR003657.

McGuire, K. J., M. Weiler, and J. J. McDonnell, 2007: Integrating tracer experiments with modeling to assess runoff processes and water transit times. *Advances in Water Resources*, **30**, 824–837, doi:10.1016/j.advwatres.2006.07.004.

McIntyre, M. E., and T. N. Palmer, 1985: A note on the general concept of wave breaking for Rossby and gravity waves. *PAGEOPH*, **123**, 964–975, doi:10.1007/BF00876984.

Meehl, G. A., *Global climate projections. Climate Change 2007: The Physical Science Basis*. S.S.E. Al, Ed. 99 pp.

Messori, G., and R. Caballero, 2015: On double Rossby wave breaking in the North Atlantic. 1–22, doi:10.1002/(ISSN)2169-8996.

Miguez-Macho, G., G. L. Stenchikov, and A. Robock, 2004: Spectral nudging to eliminate the effects of domain position and geometry in regional climate model simulations. *J. Geophys. Res*, **109**, n/a–n/a, doi:10.1029/2003JD004495.

Mitchell, K. E., 2004: The multi-institution North American Land Data Assimilation System (NLDAS): Utilizing multiple GCIP products and partners in a continental distributed hydrological modeling system. *J. Geophys. Res*, **109**, 7449–32, doi:10.1029/2003JD003823.

Moore, B. J., P. J. Neiman, and F. M. Ralph, 2012: Physical Processes Associated with Heavy Flooding Rainfall in Nashville, Tennessee, and Vicinity during 1-2 May 2010: The Role of an Atmospheric River and …. *Mon. Wea. Rev*, doi:10.1175/MWR-D.

Mundhenk, B. D., E. A. Barnes, and E. D. Maloney, 2016a: All-Season Climatology and Variability of Atmospheric River Frequencies over the North Pacific. *J. Climate*, JCLI–D–15–0655.1–51, doi:10.1175/JCLI-D-15-0655.1.

Mundhenk, B. D., E. A. Barnes, E. D. Maloney, and K. M. Nardi, 2016b: Modulation of atmospheric rivers near Alaska and the U.S. West Coast by northeast Pacific height anomalies. *J. Geophys. Res. Atmos*, **121**, 12, 751–12, 765, doi:10.1002/2016JD025350.

Nakamura, M., and R. A. Plumb, 1994: The Effects of Flow Asymmetry on the Direction of Rossby-Wave Breaking. *J. Atmos. Sci*, **51**, 2031–2045, doi:10.1175/1520-0469(1994)051<2031:TEOFAO>2.0.CO;2.

Neiman, P. J., F. M. Ralph, G. A. Wick, J. D. Lundquist, and M. D. Dettinger, 2008a: Meteorological Characteristics and Overland Precipitation Impacts of Atmospheric Rivers

Affecting the West Coast of North America Based on Eight Years of SSM/I Satellite Observations. *J. Hydrometeor*, **9**, 22–47, doi:10.1175/2007JHM855.1.

Neiman, P. J., F. M. Ralph, G. A. Wick, Y.-H. Kuo, T.-K. Wee, Z. Ma, G. H. Taylor, and M. D. Dettinger, 2008b: Diagnosis of an Intense Atmospheric River Impacting the Pacific Northwest: Storm Summary and Offshore Vertical Structure Observed with COSMIC Satellite Retrievals. *Mon. Wea. Rev*, **136**, 4398–4420, doi:10.1175/2008MWR2550.1.

Neiman, P. J., G. A. Wick, B. J. Moore, F. M. Ralph, J. R. Spackman, and B. Ward, 2014: An Airborne Study of an Atmospheric River over the Subtropical Pacific during WISPAR: Dropsonde Budget-Box Diagnostics and Precipitation Impacts in Hawaii. *Mon. Wea. Rev*, **142**, 3199–3223, doi:10.1175/MWR-D-13-00383.1.

Neiman, P. J., L. J. Schick, and F. M. Ralph, 2011: Flooding in western washington: The connection to atmospheric rivers. *J. Hydrometeor*, **12**, 1337–1358, doi:10.1175/2011JHM1358.s1.

Newman, M., G. N. Kiladis, K. M. Weickmann, F. M. Ralph, and P. D. Sardeshmukh, 2012: Relative Contributions of Synoptic and Low-Frequency Eddies to Time-Mean Atmospheric Moisture Transport, Including the Role of Atmospheric Rivers. *J. Climate*, **25**, 7341–7361, doi:10.1175/JCLI-D-11-00665.1.

Niu, G.-Y., and Coauthors, 2011: The community Noah land surface model with multiparameterization options (Noah-MP): 1. Model description and evaluation with local-scale measurements. *J. Geophys. Res*, **116**, D12109–D12119, doi:10.1029/2010JD015139.

Orlanski, I., 2005: A new look at the pacific storm track variability: Sensitivity to tropical SSTs and to upstream seeding. *J. Atmos. Sci*, **62**, 1367–1390, doi:10.1175/JAS3428.1.

Payne, A. E., and G. Magnusdottir, 2014: Dynamics of Landfalling Atmospheric Rivers over the North Pacific in 30 Years of MERRA Reanalysis. *J. Climate*, **27**, 7133–7150, doi:10.1175/JCLI-D-14-00034.1.

Payne, A. E., and G. Magnusdottir, 2015: An evaluation of atmospheric rivers over the North Pacific in CMIP5 and their response to warming under RCP 8.5. 1–18, doi:10.1002/(ISSN)2169-8996.

Peters, D., and D. W. Waugh, 1996: Influence of barotropic shear on the poleward advection of upper-tropospheric air. *J. Atmos. Sci*, **53**, 3013–3031, doi:10.1175/1520-0469(1996)053<3013:IOBSOT>2.0.CO;2.

Pfister, L., N. Martínez-Carreras, C. Hissler, J. Klaus, G. E. Carrer, M. K. Stewart, and J. J. McDonnell, 2017: Bedrock geology controls on catchment storage, mixing, and release: A comparative analysis of 16 nested catchments. *Hydrol. Process*, **31**, 1828–1845, doi:10.1002/hyp.11134.

Pilotto, I. L., D. A. Rodríguez, J. Tomasella, G. Sampaio, and S. C. Chou, 2015: Comparisons of the Noah-MP land surface model simulations with measurements of forest and crop sites in

Amazonia. *Meteorol Atmos Phys*, **127**, 711–723, doi:10.1007/s00703-015-0399-8.

Raben, P., and W. H. Theakstone, 1998: Changes of Ionic and Oxygen Isotopic Composition of the Snowpack at the Glacier Austre Okstindbreen, Norway, 1995. *Hydrology Research*, **29**, 1–20.

Ralph, F. M., and M. D. Dettinger, 2011: Storms, floods, and the science of atmospheric rivers. *Eos, Transactions American Geophysical Union*, **92**, 265–266, doi:10.1029/2011EO320001.

Ralph, F. M., and M. D. Dettinger, 2012: Historical and National Perspectives on Extreme West Coast Precipitation Associated with Atmospheric Rivers during December 2010. *Bull. Amer. Meteor. Soc*, **93**, 783–790, doi:10.1175/BAMS-D-11-00188.1.

Ralph, F. M., P. J. Neiman, and G. A. Wick, 2004: Satellite and CALJET aircraft observations of atmospheric rivers over the eastern north pacific ocean during the winter of 1997/98. *Mon. Wea. Rev*, **132**, 1721–1745, doi:10.1175/1520-0493(1998)126<0725:APAFMF>2.0.CO;2.

Ralph, F. M., P. J. Neiman, D. E. Kingsmill, P. O. G. Persson, E. T. Strem, E. D. Andrews, and R. C. Antweiler, 2003: The impact of a prominent rain shadow on flooding in California's Santa Cruz Mountains: A CALJET case study and sensitivity to the ENSO cycle. *J. Hydrometeor*, **4**, 1243–1264, doi:10.1175/1525-7541(2003)004<1243:TIOAPR>2.0.CO;2.

Ralph, F. M., P. J. Neiman, G. A. Wick, S. I. Gutman, M. D. Dettinger, D. R. Cayan, and A. B. White, 2006a: Flooding on California's Russian River: Role of atmospheric rivers. *Geophys. Res. Lett*, **33**, L13801–L13805, doi:10.1029/2006GL026689.

Ralph, F. M., P. J. Neiman, G. A. Wick, S. I. Gutman, M. D. Dettinger, D. R. Cayan, and A. B. White, 2006b: Flooding on California's Russian River: Role of atmospheric rivers. *Geophys. Res. Lett*, **33**, L13801–L13805, doi:10.1029/2006GL026689.

Ralph, F. M., P. J. Neiman, G. N. Kiladis, K. Weickmann, and D. W. Reynolds, 2011: A Multiscale Observational Case Study of a Pacific Atmospheric River Exhibiting Tropical-Extratropical Connections and a Mesoscale Frontal Wave. *Mon. Wea. Rev*, **139**, 1169–1189, doi:10.1175/2010MWR3596.1.

Ralph, F. M., T. Coleman, P. J. Neiman, R. J. Zamora, and M. D. Dettinger, 2013: Observed Impacts of Duration and Seasonality of Atmospheric-River Landfalls on Soil Moisture and Runoff in Coastal Northern California. *J. Hydrometeor*, **14**, 443–459, doi:10.1175/JHM-D-12-076.1.

Ranken, D. W., 1974: Hydrologic Properties of Soil and Subsoil on a Steep, Forested Slope. 1 pp.

Rienecker, M. M., and Coauthors, 2011: MERRA: NASA's Modern-Era Retrospective Analysis for Research and Applications. *J. Climate*, **24**, 3624–3648, doi:10.1175/JCLI-D-11-00015.1.

Riley, W. J., C. J. Still, M. S. Torn, and J. A. Berry, 2002: A mechanistic model of H 218O and C 18OO fluxes between ecosystems and the atmosphere: Model description and sensitivity

analyses. *Global Biogeochem. Cycles*, **16**, 42–1–42–14, doi:10.1029/2002GB001878.

Rios-Entenza, A., and G. Miguez-Macho, 2013: Moisture recycling and the maximum of precipitation in spring in the Iberian Peninsula. *Clim Dyn*, 1–25, doi:10.1007/s00382-013-1971-x.

Risi, C., and Coauthors, 2016: The Water Isotopic Version of the Land-Surface Model ORCHIDEE: Implementation, Evaluation, Sensitivity to Hydrological Parameters. *Hydrol Current Res*, **07**, 1–24, doi:10.4172/2157-7587.1000258.

Rodell, M., and Coauthors, 2004: The Global Land Data Assimilation System. *Bull. Amer. Meteor. Soc*, **85**, 381–394, doi:10.1175/BAMS-85-3-381.

Rouxel, M., J. Molénat, L. Ruiz, C. Legout, M. Faucheux, and C. Gascuel-Odoux, 2010: Seasonal and spatial variation in groundwater quality along the hillslope of an agricultural research catchment (Western France). *Hydrol. Process*, **25**, 831–841, doi:10.1002/hyp.7862.

Ruckelshaus Center, 2012: *Chehalis Basin Flood Hazard Mitigation Alternatives Report*. 532 pp. http://ruckelshauscenter.wsu.edu/wp-content/uploads/2013/06/chehalis-report-12-19-12.pdf.

Rutz, J. J., W. J. Steenburgh, and F. M. Ralph, 2014: Climatological Characteristics of Atmospheric Rivers and Their Inland Penetration over the Western United States. *Mon. Wea. Rev*, **142**, 905–921, doi:10.1175/MWR-D-13-00168.1.

Ryoo, J.-M., D. E. Waliser, D. W. Waugh, S. Wong, E. J. Fetzer, and I. Fung, 2015: Classification of atmospheric river events on the U.S. West Coast using a trajectory model. 1–22, doi:10.1002/(ISSN)2169-8996.

Ryoo, J.-M., Y. Kaspi, D. W. Waugh, G. N. Kiladis, D. E. Waliser, E. J. Fetzer, and J. Kim, 2013: Impact of Rossby Wave Breaking on U.S. West Coast Winter Precipitation during ENSO Events. *J. Climate*, **26**, 6360–6382, doi:10.1175/JCLI-D-12-00297.1.

Salathé, E. P., Jr., 2006: Influences of a shift in North Pacific storm tracks on western North American precipitation under global warming. *Geophys. Res. Lett*, **33**, L19820–L19824, doi:10.1029/2006GL026882.

Schaake, J. C., V. I. Koren, Q. Y. Duan, K. Mitchell, and F. Chen, 1996: Simple water balance model for estimating runoff at different spatial and temporal scales. *J. Geophys. Res. Atmos*, **101**, 7461–7475, doi:10.1029/95JD02892.

Seager, R., N. Harnik, Y. Kushnir, and W. Robinson, 2003: Mechanisms of hemispherically symmetric climate variability*. *J. Climate*, **16**, 2960–2978, doi:10.1175/1520-0442(2003)016<2960:MOHSCV>2.0.CO;2.

Senatore, A., G. Mendicino, D. J. Gochis, W. Yu, D. N. Yates, and H. Kunstmann, 2015: Fully coupled atmosphere-hydrology simulations for the central Mediterranean: Impact of enhanced hydrological parameterization for short and long time scales. *J. Adv. Model. Earth Syst*, **7**, 1693–1715, doi:10.1002/2015MS000510.

Shields, C. A., and J. T. Kiehl, 2016: Atmospheric river landfall-latitude changes in future climate simulations. *Geophys. Res. Lett*, 8775–8782, doi:10.1002/(ISSN)1944-8007.

Sklash, M. G., R. N. Farvolden, and P. Fritz, 1976: A conceptual model of watershed response to rainfall, developed through the use of oxygen-18 as a natural tracer. *CAN. J. EARTH SCI*.

Sodemann, H., and A. Stohl, 2013: Moisture Origin and Meridional Transport in Atmospheric Rivers and Their Association with Multiple Cyclones. *Mon. Wea. Rev*, **141**, 2850–2868, doi:10.1175/MWR-D-12-00256.s1.

Stewart, M. K., and J. J. McDonnell, 1991: Modeling base flow soil water residence times from deuterium concentrations. *Water Resour. Res*.

Stichler, W., 1987: Snowcover and Snowmelt Processes Studied by Means of Environmental Isotopes. *Seasonal Snowcovers: Physics, Chemistry, Hydrology*, Springer, Dordrecht, Dordrecht, 673–726.

Strong, C., and G. Magnusdottir, 2008: How Rossby wave breaking over the Pacific forces the North Atlantic Oscillation. *Geophys. Res. Lett*, **35**, L10706–5, doi:10.1029/2008GL033578.

Sturm, C., Q. Zhang, and D. Noone, 2010: An introduction to stable water isotopes in climate models: benefits of forward proxy modelling for paleoclimatology. *Climate of the Past*, **6**, 115–129.

Thorncroft, C. D., B. J. Hoskins, and M. E. McIntyre, 1993: Two paradigms of baroclinic-wave life-cycle behaviour. *Q. J. R. Meteorol. Soc*, **119**, 17–55.

Trenberth, K. E., 1999: Atmospheric moisture recycling: Role of advection and local evaporation. *J. Climate*, **12**, 1368–1381.

Trenberth, K. E., 1998: Atmospheric Moisture Residence Times and Cycling: Implications for Rainfall Rates and Climate Change. *Climatic Change*, **39**, 667–694, doi:10.1023/A:1005319109110.

Twining, J., D. Stone, C. Tadros, A. Henderson-Sellers, and A. Williams, 2006: Moisture Isotopes in the Biosphere and Atmosphere (MIBA) in Australia: A priori estimates and preliminary observations of stable water isotopes in soil, plant and vapour for the Tumbarumba Field Campaign. *Global and Planetary Change*, **51**, 59–72, doi:10.1016/j.gloplacha.2005.12.005.

van der Velde, Y., P. J. J. F. Torfs, S. E. A. T. M. van der Zee, and R. Uijlenhoet, 2012: Quantifying catchment-scale mixing and its effect on time-varying travel time distributions. *Water Resour. Res*, **48**, 1537–13, doi:10.1029/2011WR011310.

Wang, Z., and C.-P. Chang, 2012: A Numerical Study of the Interaction between the Large-Scale Monsoon Circulation and Orographic Precipitation over South and Southeast Asia. *J. Climate*, **25**, 2440–2455, doi:10.1175/JCLI-D-11-00136.1.

Warner, M. D., C. F. Mass, and E. P. Salathé Jr., 2012: Wintertime Extreme Precipitation Events along the Pacific Northwest Coast: Climatology and Synoptic Evolution. *Mon. Wea. Rev*, **140**, 2021–2043, doi:10.1175/MWR-D-11-00197.1.

Weiler, M., and J. McDonnell, 2004: Virtual experiments: a new approach for improving process conceptualization in hillslope hydrology. *JOURNAL OF HYDROLOGY*, **285**, 3–18, doi:10.1016/S0022-1694(03)00271-3.

White, A. B., D. J. Gottas, and E. T. Strem, 2002: An automated brightband height detection algorithm for use with Doppler radar spectral moments. *J. Atmos. Oceanic Technol*, **19**, 687–697, doi:10.1175/1520-0426(2002)019<0687:AABHDA>2.0.CO;2.

Wick, G. A., P. J. Neiman, and F. M. Ralph, 2013: Description and Validation of an Automated Objective Technique for Identification and Characterization of the Integrated Water Vapor Signature of Atmospheric Rivers. *IEEE Trans. Geosci. Remote Sensing*, **51**, 2166–2176, doi:10.1109/TGRS.2012.2211024.

Yang, Z.-L., and Coauthors, 2011: The community Noah land surface model with multiparameterization options (Noah-MP): 2. Evaluation over global river basins. *J. Geophys. Res*, **116**, D12110–D12116, doi:10.1029/2010JD015140.

Yoshimura, K., S. Miyazaki, S. Kanae, and T. Oki, 2006: Iso-MATSIRO, a land surface model that incorporates stable water isotopes. *Global and Planetary Change*, **51**, 90–107, doi:10.1016/j.gloplacha.2005.12.007.

Zhang, X.-P., Z.-L. Yang, G.-Y. Niu, and X.-Y. Wang, 2009: Stable water isotope simulation in different reservoirs of Manaus, Brazil, by Community Land Model incorporating stable isotopic effect. *Int. J. Climatol*, **29**, 619–628, doi:10.1002/joc.1740.

Zhu, Y., and R. E. Newell, 1994: Atmospheric Rivers and Bombs. *Geophys. Res. Lett*, **21**, 1999–2002, doi:10.1029/94GL01710.

Zhu, Y., and R. E. Newell, 1998: A Proposed Algorithm for Moisture Fluxes from Atmospheric Rivers. *Mon. Wea. Rev*, **126**, 725–735, doi:10.1175/1520-0493(1998)126<0725:APAFMF>2.0.CO;2.

Zuber, A., 1986: On the interpretation of tracer data in variable flow systems. *JOURNAL OF HYDROLOGY*, **86**, 45–57, doi:10.1016/0022-1694(86)90005-3.